INTEGRATED, INTELLIGENT, SENSOR FABRICATION STRATEGIES FOR ENVIRONMENTAL MONITORING

Takeharu Suzuki

(B.E.)

Faculty of Engineering and Information technology

Griffith University

Brisbane, Queensland, Australia

Submitted in fulfillment of the requirement of the degree of

Doctor of Philosophy

January 2004

This work has not previously been submitted for a degree or diploma in any university. To the best of my knowledge and belief, the thesis contains material previously published or written by another person except where due reference is made in the thesis itself.

Takeharu Suzuki

ACKNOWLEDGEMENTS

This PhD project was supported by CRC for **micro**Technology.
I would like to thank my supervisors, Professor David V. Thiel and Dr. Philip Tanner for their support and guidance throughout the project and their constructive criticism of the manuscript. I would also like to express gratitude to Dr. Jisheng Han, Dr. Denis Sweatman and Mr. Ray Sweatman for their support and encouragement throughout the project, Dr. Barry Wood for XPS measurement at the University of Queensland, Dr. Jason Hayes for various assistance in hot embossing at Swinburn University, Mr. Ross Stevens for FTIR measurement, Mr. Neeli MadhusudanRao for developing the hot embossing machine, Mr. Mark Cornelius for generating the patterns of the multiple sensor, Mr. Leon Gourdeas for developing the environmental chamber, and Mr. Richard Adamec for contribution to win speed/direction sensor development.

CONTENTS

ABBREVIATIONS & ACRONYMS i
ABSTRACT I
Chapter 1. Introduction 1-1
1.1. Environmental sensor technologies 1-1
1.2. Multiple sensor techniques 1-3
1.3. Signal conditions of support electronic circuits 1-5
1.4. Review of encapsulation and interconnect strategies 1-6
1.5. Conclusions and thesis overview 1-18
References 1-20
Chapter 2. Review of humidity sensors 2-1
2.1. Introduction 2-1
2.2. Definition 2-3
2.3. Ceramic-based humidity sensors 2-6
2.3.1. Sensing mechanism of ceramic types 2-6
2.3.2. Example of ionic-type humidity sensor 2-10
2.3.3. Example of electronic-type humidity sensor 2-14
2.3.4. Example of capacitive-type humidity sensor 2-16
2.3.5. Example of solid-electrolyte-type humidity sensor 2-18
2.4. Polymer-based humidity sensors 2-20
2.4.1. Sensing mechanism of polymer types 2-20
2.4.2. Example of polyelectrolyte-type humidity sensor 2-23
2.4.3. Example of dielectric-type humidity sensor 2-24
2.4.4. Example of SAW and piezoresistive-type humidity sensors 2-30
2.5. Porous silicon type 2-32
2.6. Single chip integration solution 2-34
2.7. Conclusions 2-39
References 2-41
Chapter 3. Polyimide-based capacitive humidity sensors 3-1
3.1. Introduction 3-1
3.2. Electrodes 3-3
3.3. Process temperature effect on sensitivity and temperature dependence ... 3-8
3.4. Long-term stability 3-14
3.5. Sensor support electronic circuitry 3-14
3.6. Diffusion coefficient 3-17
3.7. Chemical modification of polyimide film by O_2 plasma etching 3-20
3.7.1. Experimental procedures of humidity sensors 3-21
3.7.2. Experimental results 3-21
3.7.3. Discussion 3-30
3.8. New structure for improved sensitivity 3-32
3.8.1. Structure and fabrication 3-32

3.8.2. Sensitivity, linearity and hysteresis 3-34
3.8.3. Temperature effect 3-39
3.8.4. Frequency response 3-42
3.8.5. Discussion on sensitivity 3-45
3.9. Conclusions 3-46
References 3-47
Chapter 4. Multiple sensor fabrication strategies 4-1
4.1. Introduction 4-1
4.2. Experimental study of thermal isolation 4-2
4.3. Key strategies for multiple sensor fabrication 4-12
4.4. Process details 4-16
4.5. Conclusions 4-23
References 4-24
Chapter 5. Hot embossing for packaging intelligent environmental sensors 5-1
5.1. Introduction 5-1
5.2. Polycarbonate encapsulation using hot embossing 5-2
5.3. Hot embossing machine 5-4
5.4. Process theory and requirements 5-5
5.4.1. Environmental protection 5-5
5.4.2. Interconnects 5-6
5.4.3. Electrical insulation 5-7
5.4.4. Mechanical constraints 5-11
5.5. Optimized process details 5-15
5.6. Results 5-17
5.7. Technical limitations and extension of technology 5-21
5.8. Conclusions 5-22
References 5-24
Chapter 6. Conclusions 6-1
Appendix A : O_2 plasma treated polyimide-based humidity sensors A-1
Appendix B : Hot embossing integrated circuit dies in polycarbonate for environmental sensors B-1

LIST OF FIGURES

Chapter 1.

Fig. 1. 1. Image of environmental sensor deployment in field 1-1
Fig. 1. 2. A block diagram of switched-capacitor circuit 1-6
Fig. 1. 3. Packaging trends [1.8] 1-8
Fig. 1. 4. Cross section of exact chip scale CSP [1.10] 1-9
Fig. 1. 5. Flip-chip package with solder boll interconnections 1-10
Fig. 1. 6. Example of anisotropic conductive adhesive [1.12] 1-10
Fig. 1. 7. Wire bonding for stacked ICs 1-12
Fig. 1. 8. Stacked TAB 1-12
Fig. 1. 9. Stacked package with glass-epoxy frames (redrawn referring to [1.17]) 1-13
Fig. 1. 10. 3-D packaging on flexible substrates 1-14
Fig. 1. 11. Vertical interconnections on polymer based passivation [1.13] 1-15
Fig. 1. 12. Cross section of through-hole interconnection for 3-dimensional stack ICs [1.27] 1-16
Fig. 1. 13. Interconnections created with 30 μm-wide tracks in 1mm × 1mm opening [1.24] 1-17
Fig. 1. 14. Interconnections created by plasma anisotropic etching (a) Schematic of the structure (b) SEM image of an etched and metal-plated hole (c) SEM image at the top corner [1.26] 1-17

Chapter 2.

Fig. 2. 1. Concept of proton conduction in solid-electrolyte-type humidity sensor [2.20][2.22] 2-10
Fig. 2. 2. Constructed $MgCr_2O_4$-TiO_2 based ceramic sensor for ovens [2.24] 2-11
Fig. 2. 3. Temperature dependence of $MgCr_2O_4$-TiO_2 based humidity sensor [2.24] 2-12
Fig. 2. 4. Resistance changes due to chemisorption of various gases [2.24] 2-12
Fig. 2. 5. Cross-sectional view of humidity sensor with polarity reversed interdigitated electrode [2.25] 2-13
Fig. 2. 6. Effect of LiCr concentration on the resistance vs. relative humidity [2.25] 2-13
Fig. 2. 7. Temperature dependence of the resistance vs. relative humidity [2.25] 2-13
Fig. 2. 8. Conductivity ratio-humidity characteristics at 400 C [2.26] 2-15
Fig. 2. 9. Dependence of electric conductivity of perovskite-type oxides on the water vapor content in air at 400 C [2.26] 2-15
Fig. 2. 10. MIS structure of capacitive type ceramic humidity sensor 2-17
Fig. 2. 11. Current response as a function of relative humidity at various input

voltages at 0.5 kHz [2.32] 2-18
Fig. 2. 12. Sensor response as a function of film thickness [2.35]..... 2-19
Fig. 2. 13. Dependence of impedance on water vapor pressure at various temperature [2.36] 2-19
Fig. 2. 14. Interdigitated transducers in determination of acoustic wavelength.. 2-22
Fig. 2. 15. Sensor response as a function of film thickness [2.40]..... 2-24
Fig. 2. 16. Schematic diagram of the high-speed capacitive humidity sensor [2.50] 2-25
Fig. 2. 17. Sensor output as a function of relative humidity at room temperature with polyimide column diameters, A=5 m, B=10 m, and C=15 m [2.50] 2-25
Fig. 2. 18. Durability of linear PMMA for acetone measured at 100 kHz, 30 C in increasing RH. (●) initial value before exposure to acetone, (○) first measurement, (Δ) second, and (□) third measurement after exposure[2.55] 2-26
Fig. 2. 19. Durability of cross-linked PMMA with ED for acetone measurement at 100 kHz, 30 C in increasing RH. The symbols are the same as in Fig. 2.18 [2.55] 2-26
Fig. 2. 20. Electrical response of a thick-film CAB dielectric humidity sensor [2.37] 2-28
Fig. 2. 21. Temperature dependence at 25, 30, and 35 ˚C [2.57]..... 2-29
Fig. 2. 22. Stability of the sensor. The sensors was continuously operated at humidity of 80% RH at 25 C [2.57] 2-29
Fig. 2. 23. Schematic of SAW structure with PVA film for humidity detection [2.4] 2-30
Fig. 2. 24. Hysteresis curve of SAW RH sensor using PVA film at room temperature [2.4] 2-30
Fig. 2. 25. Schematic of the piezoresistive humidity sensor: (a) layout, (b) passivation layer system, (c-d) cross sectional view of type A and type B sensors, respectively between cross sections A and B. [2.6][2.7]..... 2-32
Fig. 2. 26. Porous silicon humidity sensor [2.65]..... 2-33
Fig. 2. 27. Response of porous silicon humidity sensor at four different frequencies at room temperature [2.65]..... 2-34
Fig. 2. 28. FET humidity sensor with CAB [2.8]..... 2-36
Fig. 2. 29. Stability of drain current at V_O=2.5 volts (D.C.) for FET humidity sensor with a 'duplex-gate' electrode or 'single-gate' electrode [2.8]..... 2-36
Fig. 2. 30. Output characteristic of FET humidity sensor measured at 25 C [2.8] 2-36
Fig. 2. 31. Hysteresis curve [2.13] 2-37
Fig. 2. 32. Sensor interface circuit [2.12]..... 2-38
Fig. 2. 33. Photograph of chip after post-processing polyimide [2.12]..... 2-38
Fig. 2. 34. Typical hysteresis measurement with polyimide (PI2160) at V_{refA}=3 V [2.12] 2-38

Chapter 3.

Fig. 3. 1. The custom built environmental chamber. 3-2
Fig. 3. 2. Images of fabricated humidity sensor. (a) IDT, (b) Slit, (c) Grid electrodes 3-3
Fig. 3. 3. Sensor response with IDT electrode. Thickness of polyimide: 0.5 μm, 1.1 μm and 21 μm. 3-5
Fig. 3. 4. Sensor response with various top electrodes of parallel-plate humidity sensors; grid with nickel (GRID), slit with nickel (SLIT), porous with nickel (PR with Ni), porous with gold (PR with AU), and porous plus grid with nickel (PR+GRID). Humidity was varied at 1% RH/min. 3-6
Fig. 3. 5. Absorption and desorption curves of the humidity sensor with a parallel-plate grid electrode, indicating maximum and minimum hysteresis locations. 3-7
Fig. 3. 6. Comparison of change in sensor capacitance when humidity was increased. Each curve corresponds to the sensors with polyimide cured at 250, 300, 350 and 400 ^{o}C. 3-9
Fig. 3. 7. Temperature dependence of humidity sensor with polyimide cured at 250 ^{o}C 3-9
Fig. 3. 8. Temperature dependence of humidity sensor with polyimide cured at 300 ^{o}C 3-10
Fig. 3. 9. Temperature dependence of humidity sensor with polyimide cured at 350 ^{o}C 3-10
Fig. 3. 10. Temperature dependence of humidity sensor with polyimide cured at 400 ^{o}C 3-11
Fig. 3. 11. Short-term drift test of humidity sensors with four different polyimide curing temperatures: 250 ^{o}C, 300 ^{o}C, 350 ^{o}C and 400 ^{o}C (a) at 20% RH, (b) at 50% RH, (c) at 90% RH 3-13
Fig. 3. 12. Long-term stability test of a polyimide-based capacitive humidity sensor for 321 days 3-14
Fig. 3. 13. Block diagram of sensor output circuitry 3-15
Fig. 3. 14. Schematic of electronic circuitry for humidity sensor 3-15
Fig. 3. 15. Constructed circuit based on the circuit diagram in Fig. 3.14. 3-16
Fig. 3. 16. DC output voltage from sensor support electronic circuitry 3-16
Fig. 3. 17. Geometry of plane sheet 3-18
Fig. 3. 18. Response curve of humidity sensor with polyimide layer cured at maximum temperature of 250 ^{o}C when the sensor was exposed to 90% RH from dry condition created with silica gel. Dotted line = experimental data, Solid line = Numerical data 3-20
Fig. 3. 19. Measured outputs of non-plasma and plasma treated humidity sensors as a function of relative humidity. 3-22
Fig. 3. 20. Hysteresis of humidity sensor, (a) Non-plasma treated (b) Plasma

treated 3-23
Fig. 3. 21. Response speed of the non-plasma and plasma treated humidity sensors to a burst of steam. 3-24
Fig. 3. 22. XPS survey scan of PI2737; (a) Non-plasma treated, (b) Plasma treated 3-26
Fig. 3. 23. XPS spectra for non-plasma treated polyimide, (a) C1s (b) O1s (c) N1s. 3-27
Fig. 3. 24. XPS spectra for plasma treated polyimide, (a) C1s (b) O1s (c) N1s . 3-27
Fig. 3. 25. FTIR subtraction spectrum of PI2737..... 3-29
Fig. 3. 26. AFM images of topography of polyimide surfaces without top electrode, (a) Non-plasma treated (b) Plasma treated 3-30
Fig. 3. 27. Sensor structures (a) Partially perforated polyimide type (b) Cross-section of the partially perforated polyimide type between A and B (c) Non-perforated polyimide type 3-33
Fig. 3. 28. Humidity sensor mounted in DIL ceramic chip carrier 3-34
Fig. 3. 29. Normalized sensor responses in capacitance at 60% RH with 1% RH/min ramping for partially perforated type and non-perforated type (a) UR5440 (b) BG-2430 3-36
Fig. 3. 30. Hysteresis of the sensors with polyimide UR-5440 at 1% RH/min ramping (a) Partially perforated type (b) Non-perforated type 3-37
Fig. 3. 31. Hysteresis with the sensors polyimide BG-2430 at 1% RH/min ramping (a) Partially perforated type (b) Non-perforated type 3-38
Fig. 3. 32. Temperature effect of the sensors with polyimide UR-5440 at 1% RH/min ramping (a) Partially perforated type (b) Non-perforated type 3-40
Fig. 3. 33. Temperature effect of the sensors with polyimide BG-2430 at 1% RH/min ramping (a) Partially perforated type (b) Non-perforated type 3-41
Fig. 3. 34. Frequency response of the sensors with polyimide UR-5440 at 1% RH/min ramping (a) Partially perforated type (b) Non-perforated type 3-43
Fig. 3. 35. Frequency response of the sensors with polyimide BG-2430 at 1% RH/min ramping (a) Partially perforated type (b) Non-perforated type 3-44
Fig. 3. 36. Illustration of water diffusion paths into a polyimide layer (a) Perforated polyimide layer case (b) Non-parforated polyimide layer case 3-45

Chapter 4.

Fig. 4. 1. Structures built to test thermal isolation, (a) Cross-section of bulk micromachined silicon with silicon nitride diaphragm (b) Top view of test structure built on silicon nitride diaphragm (c) Cross-section of polyimide plateau (d) Top view of test structure built on polyimide plateau..... 4-4
Fig. 4. 2. Fabricated thermopiles and a heater on a silicon nitride diaphragm..... 4-6
Fig. 4. 3. Temperature output of the nickel heater as a function of supplied power 4-6
Fig. 4. 4. Probe station setup for testing responses of thermopiles 4-7

Fig. 4. 5. Outputs of thermopiles as a function of nickel heater temperature 4-8
Fig. 4. 6. Fabricated 27 μm-thick polyimide plateau with nickel heater and Ni-NiCr thermopiles 4-8
Fig. 4. 7. Comparison of nickel heater temperature as a function of supplied power to the heaters on silicon nitride diaphragm and polyimide plateau 4-9
Fig. 4. 8. Comparison of thermopile outputs on the silicon nitride diaphragm and the polyimide plateau as a function of nickel heater temperature 4-10
Fig. 4. 9. Illustration of photolithography conditions with polyimide plateau.... 4-11
Fig. 4. 10. Illustration of unevenly spun photoresist 4-11
Fig. 4. 11. Illustration of multiple sensor: humidity, wind speed/direction and temperature sensors (a) Cross sectional view (b) top view 4-12
Fig. 4. 12. Crystal orientation of wafers used, (a) wafer cut for n-type {100} wafer (b) slope after anisotropic wet etching {100} wafer aligned parallel to {110} plane 4-14
Fig. 4. 13. Mask for front-to-back alignment through holes 4-17
Fig. 4. 14. Mask for creating etched pits under the sensors 4-17
Fig. 4. 15. Pattern for bottom electrode of humidity sensor..... 4-18
Fig. 4. 16. Humidity sensing 1st polyimide layer after patterning 4-19
Fig. 4. 17. Humidity sensing 2nd polyimide layer after patterning..... 4-19
Fig. 4. 18. Pattern for top electrode of humidity sensor 4-20
Fig. 4. 19. Pattern for wind/speed direction and temperature sensors..... 4-21
Fig. 4. 20. Photograph of completed multiple sensor with back lit to show silicon nitride diaphragm 4-22
Fig. 4. 21. Cross-sectional view of multiple sensor 4-22

Chapter 5.

Fig. 5. 1. Square wave oscillator using an LM324 single power supply operational amplifier 5-3
Fig. 5. 2. The custom built hot embossing machine at Griffith University..... 5-5
Fig. 5. 3. Images of head parts of bonding wires (a) Aluminium wires bonded with an ultrasonic bonder (b) Gold wires bonded with a thermocompression bonder 5-7
Fig. 5. 4. Block diagram of application of insulator and process sequence of hot embossing. 5-9
Fig. 5. 5. Elastic modulus of polycarbonate as a function of temperature. T_g = 145 C [5.6] 5-12
Fig. 5. 6. Schematic of a loading method conducted by Wilson et al. [5.7]. 5-13
Fig. 5. 7. Top view of the op amp on the dummy silicon substrate with aluminium coating prior to hot embossing 5-16
Fig. 5. 8. Complete sensor system on polycarbonate substrate with the embossed op amp, resistors and humidity sensor. 5-17
Fig. 5. 9. SEM image of a bonding wire after embossing the op amp into

polycarbonate 5-18
Fig. 5. 10. Surface profile of a bonding wire embossed into polycarbonate shown in Fig. 5. 9..... 5-19
Fig. 5. 11. Bonding wires along op amp after hot embossing (a) Photograph from the backside see-through polycarbonate sheet (b) Cross section 5-20
Fig. 5. 12. Measured frequency outputs of humidity sensor as a function of relative humidity..... 5-21

Chapter 6.

Fig. 6. 1. Schematic of hot embossed chip with CCLF..... 6-5

LIST OF TABLES

Chapter 1.

Table 1. 1. Examples of multiple sensors in application and process types..... 1-4
Table 1. 2. Electronic packaging requirements [1.8]..... 1-7

Chapter 2.

Table 2. 1. List of selected materials for polymer-based humidity sensors 2-20
Table 2. 2. Typical sensors characteristics 2-40

Chapter 3.

Table 3. 1. Outline of humidity sensor fabrication steps..... 3-4
Table 3. 2. Summary of minimum and maximum capacitance and sensitivity of five different parallel-plate electrodes..... 3-6
Table 3. 3. Summary of minimum and maximum hysteresis of various electrodes 3-7
Table 3. 4. Summary of sensitivity and capacitance change due to temperature dependence 3-11
Table 3. 5. Diffusion coefficients of polyimide cured at four different temperatures 3-19
Table 3. 6. A summary of atomic concentration of polyimide..... 3-28
Table 3. 7. Major specifications of fabricated humidity sensors..... 3-34
Table 3. 8. Summary of minimum and maximum of hysteresis in non-perforated and partially perforated type sensors 3-39

Chapter 4.

Table 4. 1. Materials used in thermopiles 4-5
Table 4. 2. Lists of solutions to the key issues for fabricating the multiple sensors 4-13
Table 4. 3. Some examples of nickel wet etchant [4.10]..... 4-15

Chapter 5.

Table 5. 1. List of drawbacks in growing SiO_2 thermally 5-8
Table 5. 2. List of merits and demerits of polymer based insulation materials... 5-10
Table 5. 3. Some mechanical and thermal properties of silicon and polycarbonate 5-12
Table 5. 4. Fracture stress of two crystal orientations [5.7] 5-13

ABBREVIATIONS & ACRONYMS

AFM	Atomic force microscopy
APM	Acoustic plate mode
CAB	Cellulose acetate butyrate
CCLF	Copper clad laminate film
CMOS	Complementary metal oxide semiconductor
CSP	Chip scale package
CTE	Coefficient of linear thermal expansion
CVD	Chemical vapor deposition
DIP	Dual-in-line package
DOF	Depth of focus
EGDM	Ethylene glycol dimethacrylate
FET	Field effect transistor
FPW	Flexural plate wave
FTIR	Fourier transform infrared
HEM	Hot embossing machine
HF	Hydrofluoric acid
HVAC	Heating, ventilation and air conditioning
IC	Integrated circuit
ICD	Integrated circuit die
IDT	Interdigital transducer
IGFET	Insulated gate field effect transistor
KOH	Potassium hydroxide
MCM	Multi chip module
MEMS	Microelectromechanical systems
MIS	Metal insulator semiconductor
PAN	Phosphoric acid, Acetic acid, Nitric acid
PC	Polycarbonate
PCB	Printed circuit board
PDMS	Polydimethylsiloxane
PECVD	Plasma enhanced chemical vapor deposition
PEFl	Polyethynylfluorenol
PET	Polyethylene Terephthalate
PMDA-ODA	Pyromellitic dianhydride-oxydianiline
PMMA	Polymethyl methacrylate
PSF	Polysulfone
PTFE	Tetrafluoroethylene
PVA	Polyvinyl-alcohol
PWM	Pulse width modulation
RIE	Reactive ion etching
SAW	Surface acoustic wave

SH-SAW	Shear horizontal surface acoustic wave
SICONEC	Signal conditioning electronics circuitry
SOI	Silicon on insulator
SSI	Small scale integration
TAB	Tape automated bonding
TCP	Tape carrier package
TMAH	Tetramethyl ammonium hydroxide
TO	Transistor outline
ULSI	Ultra large scale integration
XPS	X-ray photoelectron spectroscopy

ABSTRACT

The humidity, temperature, wind speed/direction micro sensors can be manufactured individually, resulting in three individual substrates. The integration of the three sensors into a single substrate is a vital challenge to achieve an integrated intelligent sensor so called a multiple sensor. This requires the integration of process flows and is a major challenge because adequate sensor performance must be maintained. Polyimide was selected as a humidity sensing material for its compatibility with conventional integrated circuit fabrication technology, negligible temperature dependence and good resistance against contamination. Nickel was selected for the temperature and wind speed/direction sensor because of its useful temperature coefficient and the advantage of its cost. Since the known wet etchant for nickel requires hard-baked photoresist, a method which does not attack the polyimide while removing the photoresist must be developed. The method developed for etching nickel employs hard-bake-free photoresist. Other challenge was ensuring good thermal isolation for the wind speed/direction sensor fabricated on a silicon nitride layer preformed on top of a silicon wafer. Since silicon acts as a good heat sink, the silicon under the sensor was etched entirely away until the silicon nitride layer was reached. This structure achieved good thermal isolation resulting in small power consumption. This low power feature is essential for sensors deployed in fields where power access or replacement of power sources is restricted. This structure was compared with the structure created by polyimide plateau on a silicon nitride layer coated on a silicon substrate as a function of power consumption. Based on the examination of thermal isolation, the multiple sensor utilizing a MEMS technique was fabricated with a single-sided mask aligner.

The characteristics of humidity sensors fabricated with polyimide were examined in detail with respect to variations of electrode structures, improvement of sensitivity, effect of process temperature, temperature and frequency dependence, and stability. The humidity sensor constructed with O_2 plasma treated polyimide resulted an improvement in sensitivity and hysteresis. The investigation using XPS, FTIR and AFM

concluded the chemical modification of polyimide played an important role in this improvement. The design, fabrication and results of a series of humidity sensors are quantified.

There is always no unique packaging solution for sensors because of the application-specific nature of the sensors. This intelligent environmental monitoring system was designed to accommodate both an environmental sensor and its signal conditioning electronics circuitry (SICONEC) into a single package. The environmental sensors need direct exposure to the environment while SICONEC needs a sealed encapsulation to avoid environmental damage. A new style of packaging addressing these requirements was demonstrated using a hot embossing machine. The hot embossing machine was used to embed an integrated circuit (IC) in a bare die condition into a polycarbonate (PC) sheet. In this case, the IC was flipped down against the PC, which protects the front side of the IC from the environmental damages. In a test phase, a die containing operational amplifiers was embossed into the PC. A humidity sensor and surface mount resisters were placed on the same surface of the PC to test the validity of this new technique. Interconnection between the embossed die and the humidity sensor was established using bonding wires. Copper tracks were also used to ensure all electrical connections for the die, the humidity sensor and the resistors. The results clarified the method developed. Details of process methods, issues and further potential improvement are reported.

.

Chapter 1. Introduction

1.1. Environmental sensor technologies

It is appropriate that humidity, temperature and light govern the primal environmental factors, which influence human comfort, industrial processes and agricultural activities. Among these three cases, agricultural activities may be the most basic level of production in which environmental monitoring sensors are used. Agriculture is still mostly run by the family unit whether the area of cultivation is small or large. In industrialized countries, many machines have been introduced in agriculture regardless of the size of cultivated areas and the work force. The machines are, however, mainly used to reduce physically oriented tasks. Crops, fruits and vegetables available to consumers at supermarkets have enjoyed an improvement in quality over the years. This may have been achieved as a result of good fertilizer, effective chemical formulas, improvements in seed quality, water control, temperature control and so on. These factors are mainly determined by the experience of farmers. Since microtechnology has become advanced in design and processes, environmental monitoring sensor technology may assist in growing crops, fruits and vegetables in the so called quantitative way. An image of environmental sensors deployed in the field can be seen in Fig. 1.1.

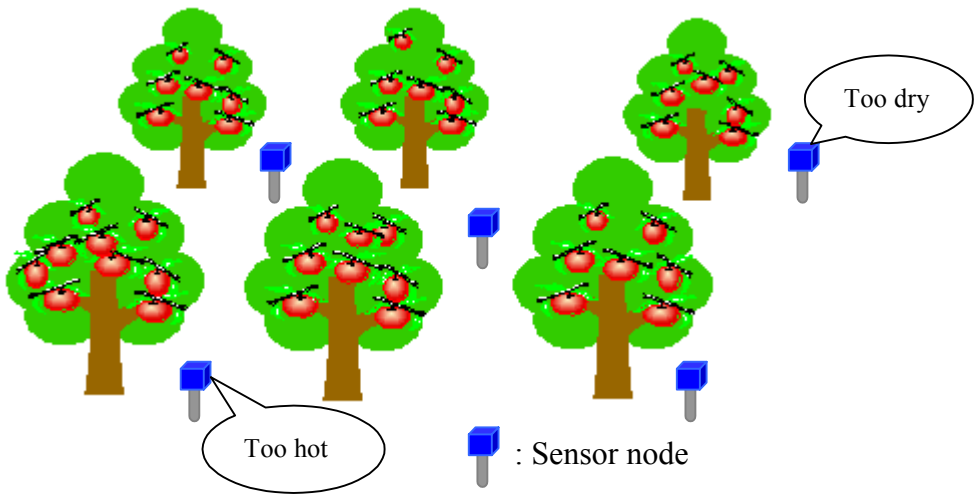

Fig. 1. 1. Image of environmental sensor deployment in field

The benefits that the sensors offer include:

(1) Remote monitoring of the environment
(2) Data logging and storing sensor data for reference and future modeling
(3) Automation of some workload
(4) As an aid for the quantitative determination of types of tasks

This may result in better quality control, a reduction of agricultural producers' workloads and a better understanding of the correlation of growing conditions and environmental influence. In order to achieve these benefits, some issues should be addressed, namely cost, sensor size, sensor installment and sensor disposal. The cost has a big impact because of the large number of sensors required to monitor the environment in a useful way. The sensor cost is determined by the sensor size, fabrication processes, and packaging method. The sensor installment at fields should also be done efficiently, otherwise this job may create an intolerably large workload. The sensor will come to the end of its useful life at some stage, so a method to dispose of the sensors must be developed. This has to be done to minimize the workload and damage to the land. In order to meet some of these requirements for improved environmental monitoring, some novel strategies were developed throughout this research. Humidity, temperature and wind speed/direction sensors were incorporated in the environmental sensor. The sensor was developed with a view to serve as a multiple functional sensor integrated into a single die.

In relation to packaging, ultimately it should accommodate a support electronic circuit and an environmental sensor together. This packaging is challenging because the two devices have different requirements. Namely, the sensor needs a sensing element to make direct contact to the environment. This means that the widely used conventional mold packaging is not suitable. On the other hand, the support electronics needs comprehensive protection against contamination from the local environment and

mechanical damage on the side where bonding pads are located. This can be achieved with the conventional mold packaging. However, the conventional packaging technology uses a large number of materials and results in a large sensor system. This may raise concerns for a disposable sensor system. Ideally when the sensor is finally disposed, the materials used to build the sensor system should be biodegradable and/or minimize damage to the soil, so that only a small sensor and integrated support electronic circuit built on silicon remain afterwards. Alternatively, a new method which leaves the minimum amount of material is necessary.

In essence, it is important to develop useful environmental sensor technologies, which provide tiny, low cost, intelligent and networked sensors. To achieve these technological benefits, this thesis reports the novel strategies developed.

1.2. Multiple sensor techniques

Multiple sensors described in this section relate to sensors with multi-functionality as well as being integrated into a single die. Combination of sensors is determined based on intended applications. Some of this type of sensors is listed in Table 1.1. Air flow in [1.1] and humidity sensors in [1.4] are omitted from the sensor types in Table 1.1 because they are not monolithically integrated according to the authors. The combinations of humidity and temperature sensors suit applications in monitoring comfort, food and pharmaceutical process conditions, and weather conditions. For example, the application raised in the article in [1.2] is useful for providing clients with the transportation history of goods. Accelerometer, pressure, temperature, and humidity sensors in this particular chip are able to monitor and record the degree of shock and stress, temperature and humidity variation during transportation. From the device fabrication point of view, MEMS especially bulk micromachining is incorporated as a part of the processes to achieve desired sensor operations. This technique is mainly used for the purpose of thermal isolation from a substrate and a detection of deformation of diaphragm with piezoresistors. The thermal isolation is effective for gas flow, infrared,

and chemical vapor sensors [1.3]. Pressure is sensed by a change in resistance of piezoresistors as a result of deformation of a diaphragm. The nature of detection method of the accelerometers in Table 1.1 also requires MEMS techniques. Examples of multiple sensors in Table 1.1 use silicon as a substrate and materials which are compatible with conventional CMOS or bipolar fabrication processes except for Pt, Cr, and ZnO in [1.3]. This implies that the sensors were designed to make use of the conventional fabrication technology but there was a need to use other materials for obtaining optimum functionality of the sensors.

Table 1. 1. Examples of multiple sensors in application and process types

Sensor types	Purpose	Process type	Chip size	Ref.
Temperature Humidity	Comfort for human environment	Silicon substrate MOS + MEMS	n.a.	[1.1]
Accelerometer Pressure Temperature Humidity sensor	Logistic system	SOI substrate Bipolar + MEMS	15×10 mm^2	[1.2]
Gas flow Infrared sensing Accelerometer Chemical vapor Tactile Charge-coupled device	Physical and chemical variables	Silicon substrate MOS + MEMS ZnO and Pt are used.	8×9 mm^2	[1.3]
Peak expiratory flow Temperature Pressure	Pulmonary function diagnostics	Silicon substrate MOS + MEMS	4 mm^2	[1.4]

Chip size is also an important parameter. If sensors cannot be integrated vertically, resulting in the side-by-side integration, the overall required substrate area increases, which reflects as a higher manufacturing cost. The larger chip size is also at a risk of reduction of production yield due to higher chance of defects on the chips. The examples in Table 1.1 show that as the number of sensor types per die increases, there will be a corresponding increase in the die size. Process integration is an important

strategy to keep the number of process steps to a minimum when the number of integrated sensor types increases per die.

1.3. Signal conditions of support electronic circuits

In this section, some key issues associated with support electronics for humidity sensors are briefly discussed.

Humidity sensors are classified in two types based on operating principles: resistive and capacitive types. When a resistive type sensor is used, it is important to note that the degree of an output change between dry and wet conditions, temperature dependence and impedance level. Resistive type humidity sensors tend to have a very large response and to respond exponentially. This is discussed in Chapter 2.It may be necessary to incorporate a logarithmic circuit in order to compress the overall response into a suitable signal level. If a temperature dependence is beyond an intended application range, temperature compensation circuitry is necessary. Typically, this type of sensor shows very large impedance at low humidity. This requires particular attention to design noise-proof circuits, providing a measure such as a guard ring where sensor output is read. In addition, if signal amplification is necessary, FET type operational amplifiers should be used. If sensor excitation by a dc signal is prohibited to apply due to degradation of the sensor, an ac signal is carefully applied at amplitude which does not damage the sensing material.

In capacitive type sensors, an ac signal is also applied at amplitude which does not damage the sensing material. The capacitive type sensors tend to have a small response. This relates to the signal-to-noise ratio. The capacitive type sensors can be used as a part of an oscillation circuit. The sensor can be used with known 555 timer IC in an astable mode, resulting in frequency output. This method has been presented [1.5]. With a 555 timer, pulse width modulation mode can also be used. The output signal can be fed directly to a microprocessor or converted to dc voltage with a low pass filter. Other detection methods can be used based on signal comparisons between a reference

and a sensor called a switched-capacitor readout circuit [1.6]. Pulse trains out of phase with each other are applied to the reference and the sensor in this method. If there is a phase difference between the two signals as a result of a sensor response, an integrator performs a charge and discharge operation. After the integration stage, output signals can be fed to an A/D circuit. A block diagram of this circuit is shown in Fig. 1.2.

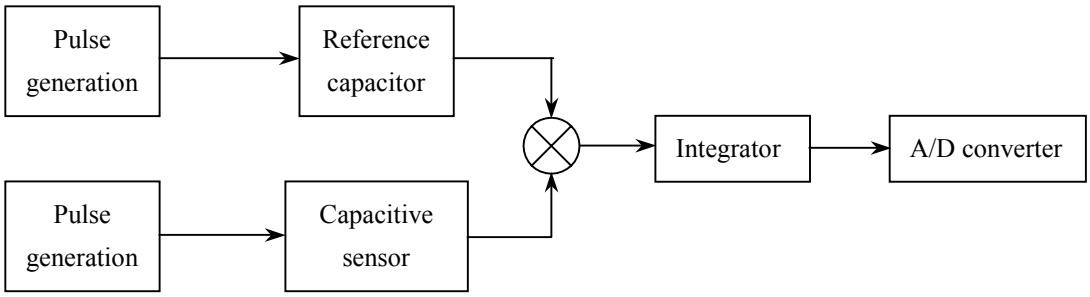

Fig. 1. 2. A block diagram of switched-capacitor circuit

1.4. Review of encapsulation and interconnect strategies

The packaging of the integrated circuit (IC) was viewed in the form called dual-in-line package (DIP) developed in the 1960s [1.7]. Increasing complexity of the ICs and higher input/output (I/O) led to the DIP package. This was a major change in package since transistor outline (TO) package was developed for early transistors before 1960s. The minimum purposes of the packaging are to provide the interconnections of power and signals, mechanical and environmental protections for ICs. Since IC technology progressed from small-scale integration (SSI) to ultralarge-scale integration (ULSI), the requirements of packaging have been growing. Some of the requirements are listed in Table 1.2. Requirements for environmental sensors have been added to this list.

Table 1. 2. Electronic packaging requirements [1.8]

Category	Requirement	Category	Requirement
Speed	• Large bandwidth • Short inter-chip propagation delay	Test and Reliability	• Easy to test • Easy to modify • Highly reliable • Low cost
Thermal and Mechanical	• High heat removal rate • A good match between the thermal coefficients of the dice and the chip carrier	Noise	• Low noise coupling among wires • Good-quality transmission line • Good power distribution
Pin count and Wireability	• Large I/O count per chip • Large I/O between the first and second level package	Environmental sensors	• Small parasitic inductance and capacitance • Protection against contamination
Size	• Compact size		

Because packaging is a broad area, a single-chip packaging, stacked-chip packaging, and interconnection for stacked packaging are covered in this review section. Fig. 1.3 [1.8] illustrates the variation of IC package types developed over decades. The evolution of package types is the motivation of solving the technology demands such as increasing the number of input/output (I/O) leads, and smaller footprint. The package types arranged diagonally in Fig. 1.3 shows this trend. Chip scale package or chip size package (CSP) at the lower right hand corner in Fig. 1.3 meets this trend. It features large I/O counts and small footprint which is equal to or 1.2 times larger than that of the bare die [1.7].

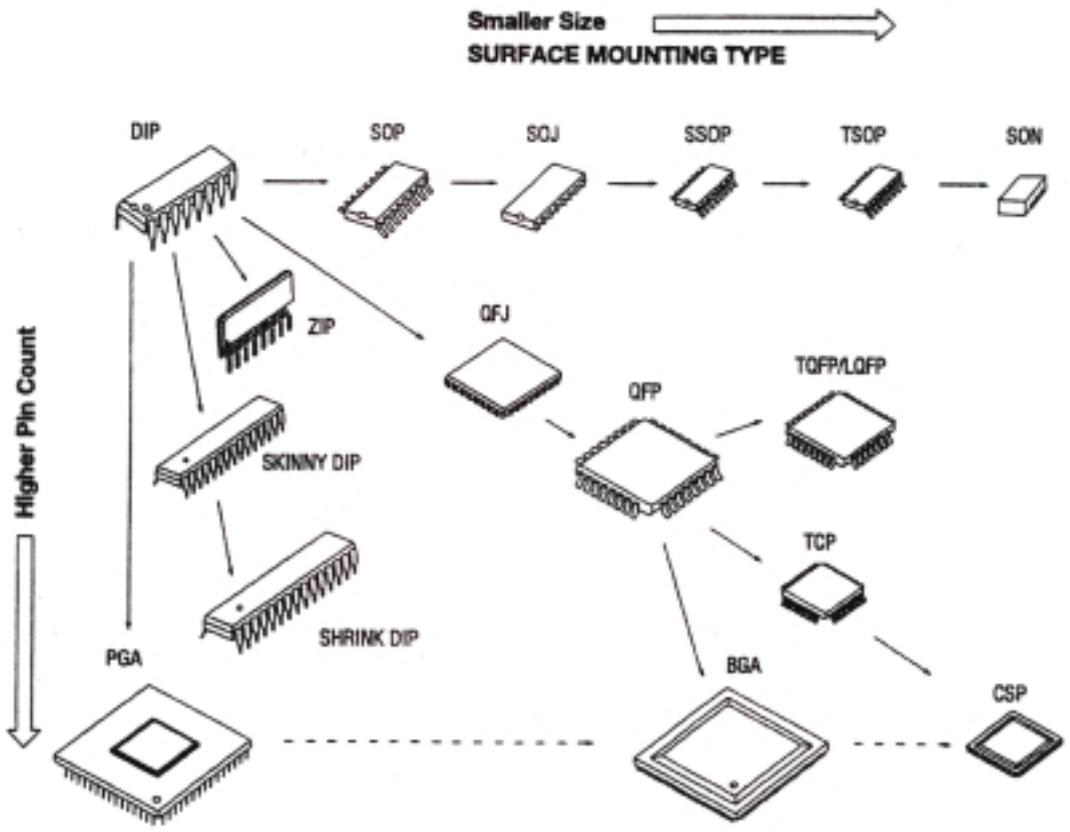

Fig. 1. 3. Packaging trends [1.8]

Interconnection between a die and a package has to be established in any packaging style. In general, this process is as follows. A die is attached on a metal leadframe with die attach adhesive. Wire bonding is performed between bonding pads on the die and the leadframe with either gold or aluminum wire. The encapsulation is made by the process called a transfer molding method using commonly thermosetting polymers. This process ensures mechanical protection and minimum environmental damage. In ceramic packages, a die is directly attached in the cavity of a chip carrier with die attach adhesive. Similarly, wire bonding is performed. Hermetical sealing between a ceramic chip carrier and a cap is carried out using low-temperature glass.

In CSP, there are fan-in and fan-out types, depending on the ratio of the number of pin counts and the die size [1.9]. With CSP technology, a die is usually mounted on an organic substrate. The interconnection between pads for electrical

contacts on the die and metal tracks on the organic substrate is established by bonding wires. The metal tracks are extended to external terminals on the reverse side of the substrate, which are usually made of solder balls. Using bonding wires results in slightly larger package size than die size. The method to make the exact chip size packaging has been reported [1.10]. The die is flipped face down in this method. Instead of bonding wires, metal posts created on Al pads on a die are used. The metal posts are attached to metal redistribution tracks formed on the encapsulant. Finally, as Fig. 1.4 shows, these tracks are connected to the solder balls on the reverse side of the encapsulant for a chip mounting.

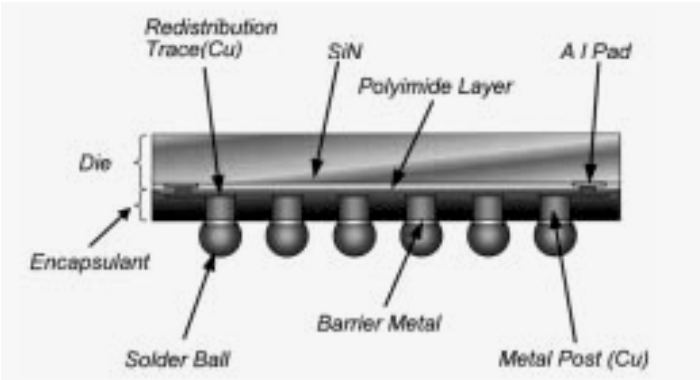

Fig. 1. 4. Cross section of exact chip scale CSP [1.10]

Flip-chip packaging in Fig. 1.5 is one of the surface mounting type packages, offering more than 1000 I/O [1.11], and very small parasitic inductance and capacitance because of a direct chip connection between a die and a substrate, meaning no wire-bonding is required. Similar to CSP, organic substrates such as FR4 and polyimide as well as ceramic are used in flip-chip packaging. Interconnections can be established by forming bumps such as solder balls, electroless nickel bumps or gold stud bumps on bonding pads on the IC. Solder balls on the IC are attached to electrodes created on a substrate using a reflow process. Because of the surface tension of solder, a small misalignment between the IC and the substrate can be compensated by self-aligning. Gold stud bumps are possibly pressed against electrodes on a substrate with application

of temperature simultaneously. An anisotropic conductive film is also used as an interconnection method. Metal particles such as gold, silver, or nickel are dispersed throughout this polymer based conductive film. This film is placed between a die and a substrate at the beginning. Then the electrodes on the die and the substrate are aligned. The electroless nickel bumps can be used for these electrodes. Application of pressure and temperature establishes electrical connections between the die and the substrate. With the right pressure, metal particles are trapped between the electrodes resulting in electrical conduction only in z direction while x and y directions are kept isolation as Fig. 1.6 shows. This film also becomes the underfill between the die and the substrate. In general, the underfill which may be epoxy based is necessary in flip chip packages to enhance mechanical rigidity of solder joints. If any anisotropic conductive film is not used, underfill is usually applied under a die after reflow of solder bumps.

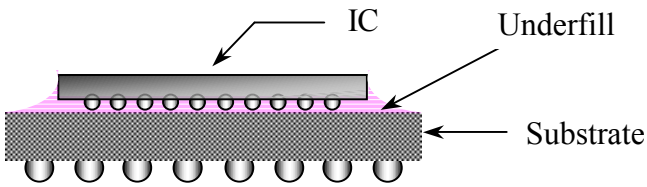

Fig. 1. 5. Flip-chip package with solder boll interconnections

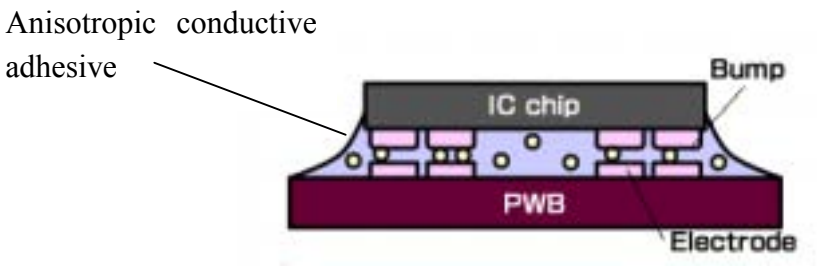

Fig. 1. 6. Example of anisotropic conductive adhesive [1.12]

The general packaging aspects for a single chip has been presented so far. The attention is turned to interconnections applicable for stacked chips in the rest of this review section. Al-sarawi et al. [1.13] reviewed three-dimensional packaging technologies including vertical interconnection techniques. This review, however, covers a broad range of examples. The examples in the review are used as a guide for packaging and interconnection for environmental sensors. Therefore, some variations to the review have been made here. The selection criteria are:

(1) There is a possibility to mount a sensor such a way that its sensing element is faced up even though dice are stacked.
(2) No lid or cover over the sensor is required.
(3) No multichip module (MCM) types because of a large footprint.

Wire bonding is a de facto method to interconnect a single chip. This method has been extended to form interconnections between stacked dice as Fig. 1.7 shows [1.14-1.16]. A die is wire-bonded across bonding pads and metal tracks on an organic substrate, and adhesive material is placed followed by placing the next die and bonding wires [1.14]. This method has been applied to stack up to three dice, which were thinned down to 150 μm for market demand of small height [1.15]. This type of packaging requires the top chip to be smaller size. Nakanishi et al. [1.16] demonstrated the TSOP packaging using wire bonding, which contains two dice mounted each on front and underside of a leadframe. This can be seen in Fig. 1.7 (b).

Similar to the wire bonding, the interconnections can be formed by tape automated bonding (TAB) as shown in Fig. 1.8 [1.13]. The vertical interconnects are created by through-holes and joined with solder Fig. 1.9 [1.17]. Each die is mounted on tape carrier package (TCP). Wire bonding is made between gold plated leads on TCP and pads on the die.

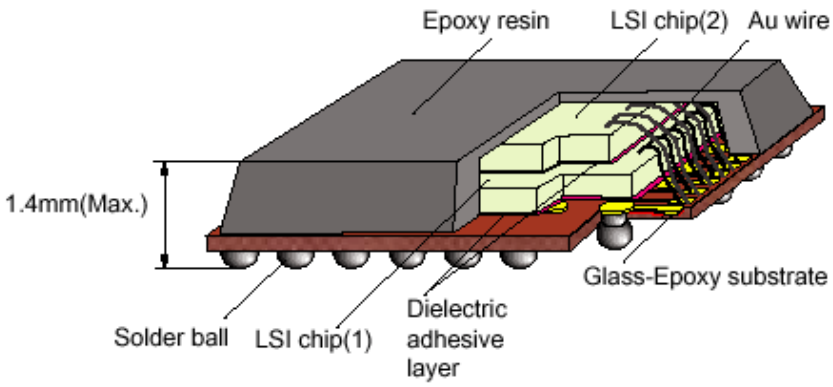

(a) Piggy back mount [1.14]

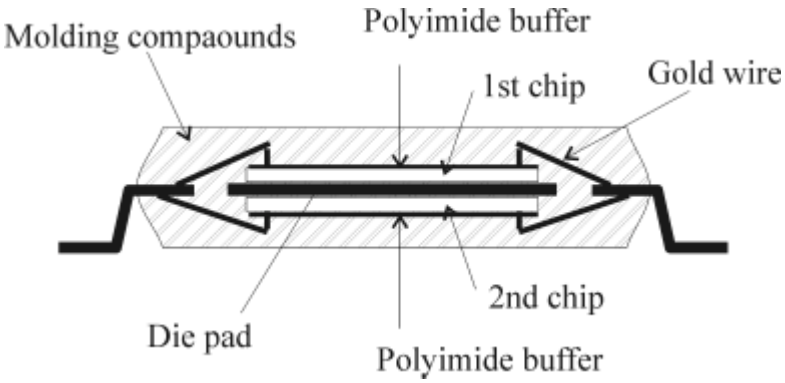

(b) Individual mount (redrawn referring to [1.16])

Fig. 1. 7. Wire bonding for stacked ICs

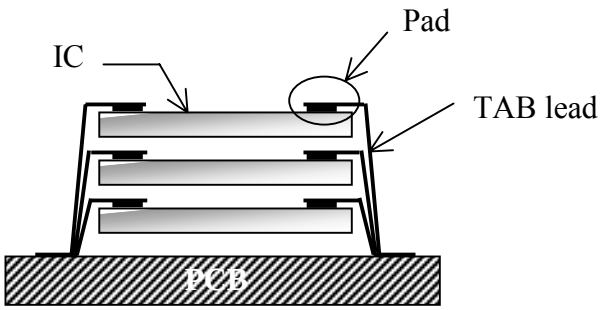

Fig. 1. 8. Stacked TAB

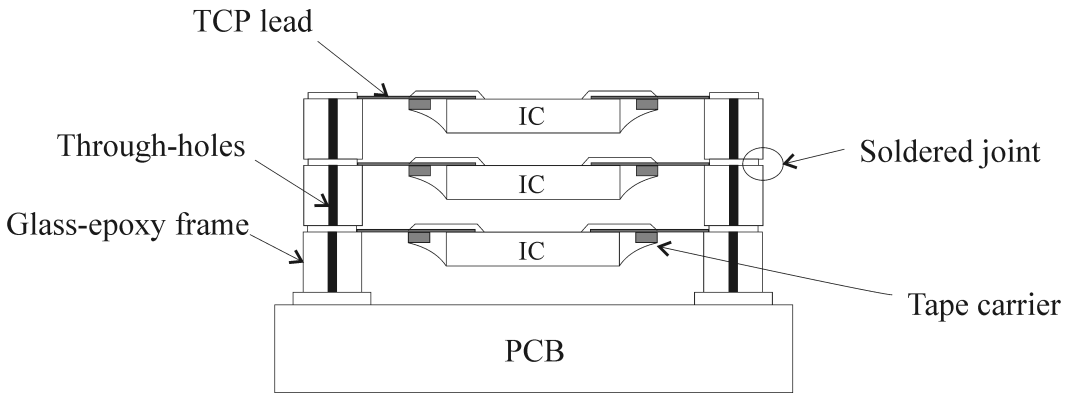

Fig. 1. 9. Stacked package with glass-epoxy frames (redrawn referring to [1.17])

Folded flexible tape has been demonstrated for packaging multiple chips in Fig. 1.10 [1.13][1.18][1.19]. Each die is mounted on a flexible substrate such as polyimide. After placing all components, a flexible substrate is folded to minimize the footprint. The interconnection between dice is established by metal tracks formed on the flexible substrate. The bonding pads on a die and electrodes on the flexible substrate are joined with gold stud bumps [1.18].

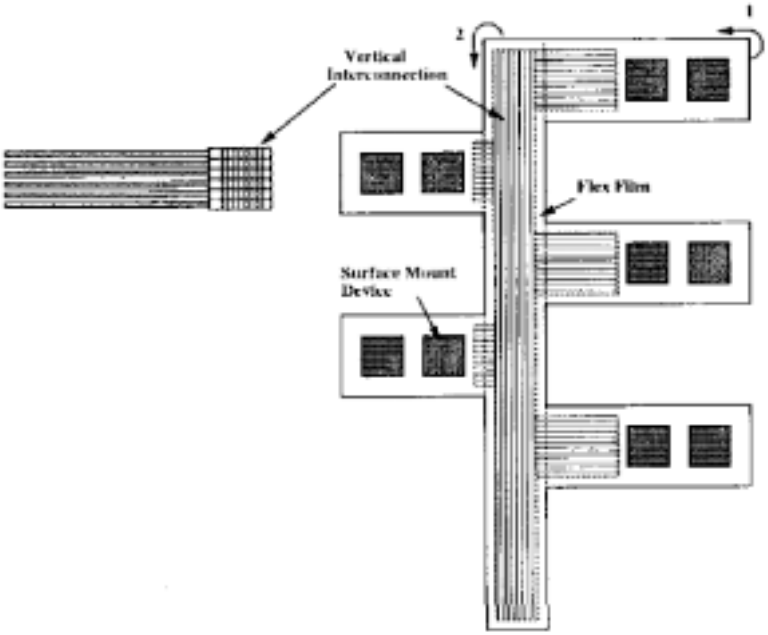

(a) 3-D packaging on flexible substrate [1.13]

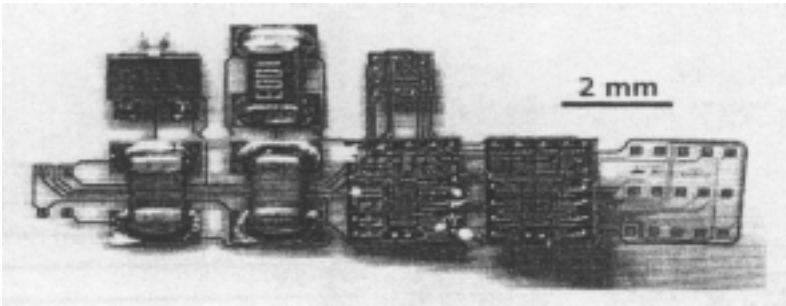

(b) 3-D packaging on polyimide substrate with ICs and discrete components before folding [1.18]

Fig. 1. 10. 3-D packaging on flexible substrates

Instead of using vertical frames such as depicted in Fig. 1.9, interconnections between stacked dice are formed over passivation on the sidewall of the stacked dice as in Fig. 1.11. This method called a bare die stacking technology has been demonstrated using polyimide [1.20][1.21], and combination of polyimide plus thermoplastic adhesives as passivation [1.22]. The polyimide is used to insulate each die and serve as a layer to distribute I/O lines on the side of a die [1.20]. In addition to the former case,

the combination of polyimide and thermoplastic adhesives is also used to insulate sidewalls of the dice [1.22].

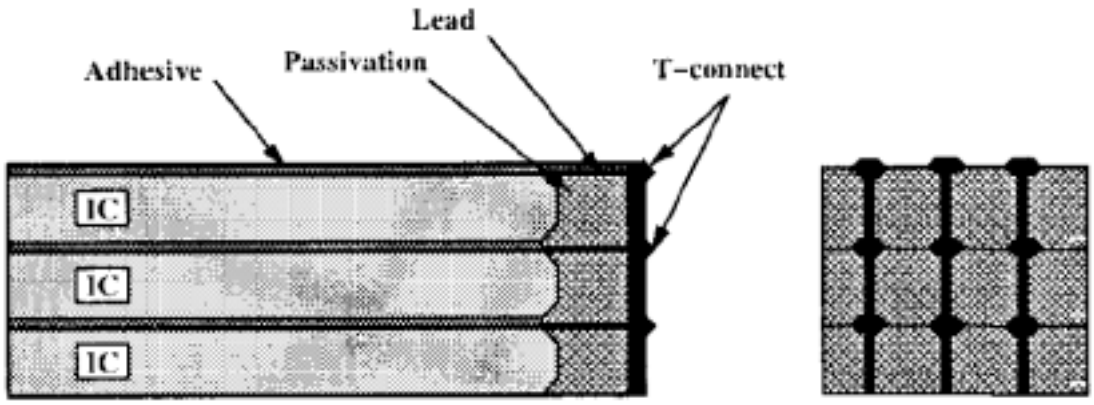

(Cross section) (Side view)

Fig. 1. 11. Vertical interconnections on polymer based passivation [1.13]

The examples so far are based on interconnections created around the periphery of ICs. In contrast, there is a technique creating through-holes directly in a silicon substrate [1.23-1.29]. This through-hole technique is able to create interconnections for three-dimensional packaging with the highest interconnection density [1.25]. The through-holes can be created by etching silicon either isotropically or anisotropically. Examples created anisotropically are shown in Figs. 1.12 and 1.13. The structure in Fig. 1.12 was created using a wet etching method followed by insulating the holes with PECVD SiO_2. Electrical paths were formed by electroplating with gold, achieving a 25 μm-thick layer [1.27]. The authors claimed that it was also possible to stack multiple dice with this technique using solder joints.

Instead of electroplating through-holes, metal tracks were formed along the slope of the through-holes from the front to the reverse side of the silicon substrate as in Fig. 1.13 [1.24]. The etch pit created by anisotropic wet etching of {100} silicon has sloped sides with angles of 54.7° as defined by the {111} crystal planes. The metal layers were deposited using an e-beam system on SiO_2 which was grown on the surface of the silicon substrate. Before patterning the metal, electrodeposition of photoresist was

performed. This photoresist deposition method created a highly uniform photoresist layer on the conductive surface of the substrate. After patterning the photoresist, the metal tracks were patterned with a wet etching method.

In order to achieve higher interconnection density, anisotropic etching methods using a plasma etching technique have been studied [1.25-1.29]. The size of the holes is considerably smaller compared to those created anisotropic wet etching which needs openings of greater than 100 μm in diameter with the wafer thickness beyond 400 μm [1.25]. For example, 30 μm × 30 μm holes were created in 525 μm-thick silicon wafer using a reactive ion etching (RIE) system with SF_6 and C_4F_8 gas mixture [1.26]. Once holes are created, electrical isolation must be considered using either application of reverse bias voltage or deposition of dielectric material(s). The example in Fig. 1.14 employed SiO_2 as a dielectric material for electrical isolation followed by polysilicon and copper deposition for signals to pass [1.26]. The holes were not completely filled with copper in this example.

There is no unique solution for sensor packages because they must be application specific. However, it is true that short length of interconnects, good mechanical and environmental protections and a small footprint are advantageous.

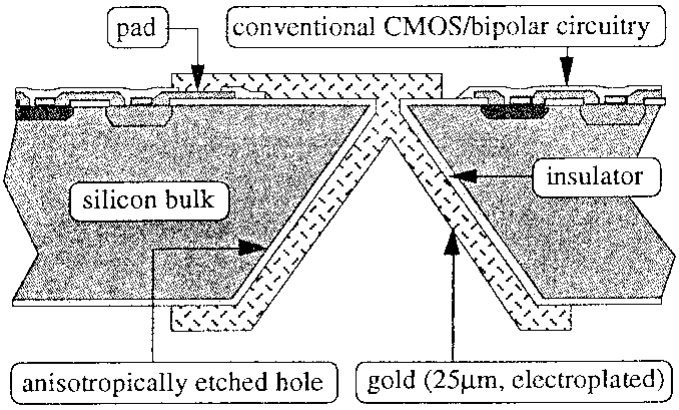

Fig. 1. 12. Cross section of through-hole interconnection for 3-dimensional stack ICs [1.27]

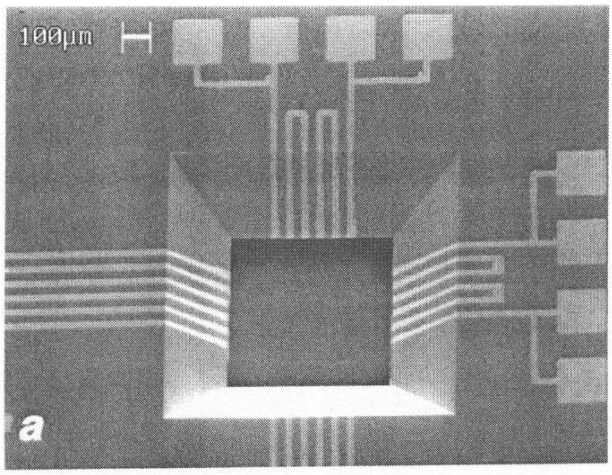

Fig. 1. 13. Interconnections created with 30 µm-wide tracks in 1mm × 1mm opening [1.24]

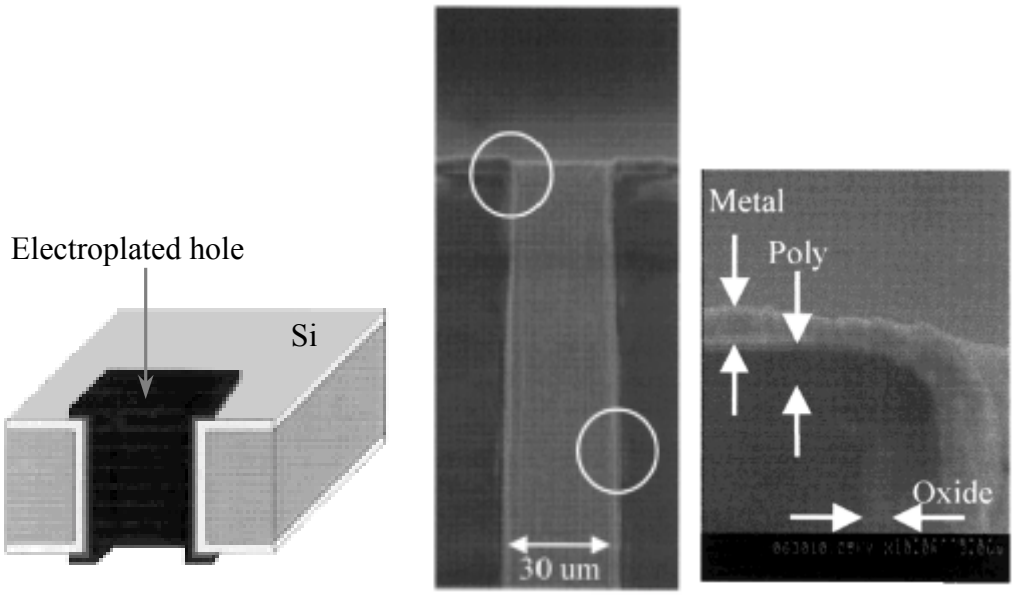

(a) (b) (c)

Fig. 1. 14. Interconnections created by plasma anisotropic etching (a) Schematic of the structure (b) SEM image of an etched and metal-plated hole (c) SEM image at the top corner [1.26]

1.5. Conclusions and thesis overview

In this chapter, the requirements of a multielement environmental sensor have been reviewed in the light of previous work in the area. The sensor itself must be small, low-powered and preferably integrated on to a single substrate using a minimum number of process steps. The sensor must be conveniently packaged with the sensor surface exposed but the support electronics and interconnects protected from the environment. This thesis reports on a unique approach to solving these problems for a multielement sensor destined for agricultural monitoring.

Chapter 2 reviews the humidity sensors fabricated with ceramics and polymers for humidity sensing materials in terms of their humidity detection mechanisms, structure, process outlines, and characteristics. This review reports a suitable humidity sensor included in the multiple sensor described in Chapter 4. Chapter 3 includes the studies of humidity sensors in order to optimize their characteristics using CMOS compatible fabrication processes. The characteristics examined are (a) the sensitivity measured with a series of different electrode structures, (b) the effects of curing temperature variations used for polyimide, temperature dependence, frequency response, hysteresis, and stability. An improvement in sensitivity achieved with O_2 plasma treated polyimide and partially perforated polyimide in humidity sensors is also discussed. Plasma etching applied to polyimide film after cure caused increase in sensitivity towards moisture and improvement of hysteresis. Surface chemistry of plasma treated polyimide was examined using XPS and FTIR. AFM was used for examination of polyimide surface morphology. The distinctive change before and after the treatment is discussed. Diffusion coefficients in absorbing moisture were extracted and compared using the polyimide cured at different temperatures. Chapter 4 features the process strategies of integrated multiple sensor; humidity, wind speed/direction and temperature sensors. The influence of thermal isolation is demonstrated using a back-etched silicon structure and a thick polyimide plateau on a silicon nitride layer formed on a silicon substrate. Based on the investigation of thermal isolation, the multiple sensor was

fabricated using a bulk micromachining technique with a single-sided mask aligner. Chapter 5 presents innovative packaging techniques, employing a hot embossing machine. This method was developed in search for simple and cheap ways of packaging support electronic circuitry as well as an environmental sensor. A novel part of this work is embedding an integrated circuit die into a plastic sheet in a face-down manner. The method is successfully applied to operational amplifier. The process flows, issues and the test result in conjunction with a humidity sensor are presented. Chapter 6 states general conclusions of the thesis. Some suggestions are included for the purpose of future improvement of the work made throughout this research.

The original contributions of this thesis include:

- A multiple sensor; namely humidity, temperature and wind speed/direction sensors, fabricated using a MEMS technique, achieving low power consumption.
- Demonstration of capability in complex multiple sensor process sequences with a single-sided mask aligner. To the best of our knowledge, the multiple sensor integrated in the form of overlying on top each other in addition to a thin diaphragm has not been demonstrated previously.
- A nickel wet etching with the aid of hard-bake-free photoresist has successfully been applied without damaging polyimide layers. This method only requires acetone to remove the photoresist.
- A hot embossing machine has been applied to embed an integrated circuit in bare die form into a polycarbonate sheet. The validity of the method has been demonstrated with a humidity sensor

References

[1.1] J. Kang and S. Park, "Development of comfort sensing system for human environment", *Mechatronics*, 8, pp. 459-466, 1998

[1.2] T. Fujita and K. Maenaka, "Integrated multi-environmental sensing-system for the intelligent data carrier", *Sens. Actuators A*, vol. 97-98, pp. 527-534, 2002

[1.3] D.L. Polla, R.S. Muller, and R.M. White, "Integrated multisensor chip", *IEEE Electron Device Lett.*, vol. EDL-7, no. 4, pp. 254-256, Apr. 1986

[1.4] A.F.P. van Putten, M.H.P.M. van Putten, R. Eichler, F. Dankwart, C. Pellet, C. Laville, B. Puers, D.D. Bruijker, C.M.B.A. Correia, M. Morgado, R. ten Wolde, J. Berends, P.F.A.M. van Putten, and M.J.A.M. van Putten, "Multiple-Sensor micro-system for pulmonary function diagnostics for COPD and asthma patients", *Proc. SeSens Workshop*, pp. 683-688, Dec. 2000

[1.5] J.M. Pérez, and C. Freyre, "A Poly(ethyleneterephthalate)-based humidity sensor", *Sens. Actuators B*, vol. 42, pp. 27-30, 1997

[1.6] U. Schoeneberg, B.J. Hosticka, G. Zimmer, and G.J. Maclay, "A novel readout technique for capacitive gas sensors", *Sens. Actuators:* B, vol. 1, pp. 58-61, 1990

[1.7] W.D. Brown, *Advanced electronic packaging: with emphasis on multichip modules*, IEEE Press, New York, 1999, p.13

[1.8] W, Chen, *The VLSI handbook*, CRC Press , New York, 2000, pp. 11.1-11.16

[1.9] I. Anjoh, A. Nishimura, and S. Eguchi, "Advanced IC packaging for the future applications", *IEEE Trans. Electron Devices*, vol. 45, no. 3, March 1998, pp. 743-752

[1.10] T. Kawahara, "Super CSP", *IEEE Trans. Adv. Pack.*, vol. 23, no. 2, pp. 215-219, May. 2000

[1.11] J.H. Lau, *Flip chip technologies*, McGraw Hill, Boston, MA, 1996, p. 225

[1.12] Hitachi Chemical Co., Ltd. www.hitachi-chem.co.jp Dec. 2000

[1.13] S.F. Al-sarawi, D. Abbott, and P.D. Franzon, "A review of 3-D packaging technology", *IEEE Trans. Comp., Packag., Manufact., Technol.*, Part B, vol. 21, no. 1, pp. 2-14, Feb. 1998

[1.14] Mitsubishi Electric Corp., IC package catalog, Sept. 1999

[1.15] Y. Fukui, Y. Yano, H. Jusi, Y. Matsune, K. Miyata, A. Narai, Y. Sota, Y. Takeda, K. Fujita, and M. Kada, "Triple-chip stacked CSP", *in Proc. 2000 50th Electron. Comp. Technol. Conf., IEEE*, Las. Vegas, NV, pp. 385-389, May 2000

[1.16] H. Nakanishi, T. Maruyama, K. Miyata, T. Ishio, Y. Sota, A. Narai, S. Fukunaga, K. Toyosawa, K. Fujita, and M. Kada, "Development of high density memory IC package by stacking IC chips", *in Proc. '95 45th Electron. Comp. Technol. Conf., IEEE*, Las. Vegas, NV, pp. 634-640, May 1995

[1.17] I. Miyano, K. Serizawa, S. Sakaguchi, T. Ishida, M. Yamada, and T. Kudaishi, "Fabrication and thermal analysis of 3 dimensionally located LSI packages", *Proc. 9th Euro. Hybrid Microelectron*. Conf., Nice, France, June 1993, pp. 184-191

[1.18] J. Meyer, T. Stieglitz, O. Scholz, W. Haberer, and H. Beutel, "High density

interconnects and flexible hybrid assemblies for active biomedical implants", *IEEE Trans. Adv. Pack.*, vol. 24, no. 3, pp. 366-374, Aug. 2001

[1.19] H. Goldstein, "Packages go vertical", *IEEE Spectrum*, pp.46-51, Aug. 2001

[1.20] M.D. Caterer, T.H. Daubenspeck, T.G. Ference, S.J. Holmes, and R.M. Quinn, "Processing thick multilevel polyimide films for 3-D stacked memory", *IEEE Trans. Adv. Pack.*, vol. 22, no. 2, pp. 189-199, May 1999

[1.21] J.A. Minahan, A. Pepe, R. Some and M. Suer, "The 3-D stack in short form", *in Proc. '92 42nd Electron. Comp. Technol. Conf., IEEE*, San Diego, CA, pp. 340-344, May 1992

[1.22] H.S. Ko, J.S. Kim, H.G, Yoon, S.Y. Jang, S.D. Cho, K.W. Paik, "Development of three-dimensional memory die stack packages using polymer insulated sidewall technique", *IEEE Trans. Adv. Pack.*, vol. 23, no. 2, pp.252-256, May 2000

[1.23] M.A.S. Jaafar, and D.D. Denton, "A plated through-hole interconnect technology in silicon", *J. Electrochem. Soc*. vol. 144, no. 7, pp. 2490-2495, July 1997

[1.24] C. Christensen, P. Kersten, S. Henke, and S. Bouwstra, "Wafer through-hole interconnections with high vertical wiring densities", *IEEE Trans. Comp., Packag., Manufact., Technol.*, Part A, vol. 19, no. 4, pp. 516-521, Dec. 1996

[1.25] E.M. Chow, V. Chandrasekaran, A. Partridge, T. Nishida. M. Sheplak. C.F. Quate and T.W. Kenny, "Process compatible polysilicon-based electrical through-wafer interconnects in silicon substrate", *J. Microelectromech. Syst*., vol. 11, no. 6, pp. 631-640, Dec. 2002

[1.26] H.T. Soh, C.P. Yue, A. McCarthy, C. Ryu, C. Ryu, T.H. Lee, S.S. Wong, and C.F. Quate, "Ultra-low resistance, through-wafer via (TWV) technology and its applications in three dimensional structures on silicon", *Jpn, J. Appl. Phys.*, Part 1, vol. 38, no. 4B, pp. 2393-2396, April 1999

[1.27] S. Linder, H. Baltes, F. Gnaedinger, and E. Doering, "Fabrication technology for wafer through-hole interconnections and three-dimensional stacks of chips and wafers", *Proc. 7th IEEE Int. Workshop Microelectromechanical Syst., MEMS 1994*, Japan, Jan 1994, pp.349-354

[1.28] E.M. Chow, A. Partridge, C.F. Quate, and T.W. Kenny, "Through-wafer electrical interconnects compatible with standard semiconductor processing", *Solid-State Sensor and Actuator Workshop*, Hilton Head Island, SC, June 4-8 2000, pp.343-346

[1.29] E.M. Chow, H.T.Soh, H.C. Lee, J.D. Adams, S.C. Minne, G. Yaralioglu, A. Atalar, C.F. Quate, and T.W. Kenny, "Integration of through-wafer interconnects with a two-dimensional cantilever array", *Sens. Actuators A*, vol. 83, pp. 118-123, 2000

Chapter 2. Review of humidity sensors

2.1. Introduction

The purpose of this review is the selection of a method to fabricate miniaturized humidity sensors using conventional IC processes with a view to implementing them in the multiple sensors as a single chip. This idea is presented in Chapter 4.

It is important to understand the desired requirements imposed on a good humidity sensor. These requirements are listed below.

(1) Good reproducibility

Reproducibility is a very important characteristic in regards to reliability. For a sensor to be useful, its output should be consistent with time.

(2) High sensitivity

The sensors with high sensitivity may relieve the design complications of support electronic circuits. If the sensitivity is too low, large signal amplification and a large number of parts are required to meet a satisfactory sensor output. In relation to output signal quality, the signal-to-noise ratio may also degrade.

(3) Small hysteresis

Hysteresis is the difference of sensor output between increasing and decreasing humidity. Sensors with small hysteresis are useful for precise readings.

(4) Good linearity

Linearity may not be a major issue because compensation is possible with a microprocessor. However good linearity reduces the demand for extra electronic circuits, parts and programming effort.

(5) High durability

Durability can be classified into mechanical and chemical aspects. Mechanical durability is determined by the type of substrate, sensor structure and packaging method. Chemical durability is determined by the type of sensing materials.

(6) Negligible temperature dependence

Negligible temperature dependence is useful to simplify the sensor design, support electronics and programming for compensation.

(7) Resistance against contamination

Contaminations such as smoke, oil, organic solvent, acidic/alkaline chemicals and so on degrade the performance of the sensor, resulting in misleading sensor outputs. Selection of humidity sensing material should reflect intended application area of humidity sensors. Recovery methods from contaminations may be employed in certain applications for more reliable sensors.

(8) Low cost

Although performance of the sensor may be excellent, if the production cost is very high, this may become a disincentive to entering markets. To avoid this problem, design and production should be reviewed carefully.

(9) Fast response speed

Response time may become important in the applications requiring fast response time such as industrial processes and medical facilities.

In this thesis, research and development efforts have an emphasis on answering various applications and improving the performance requirements described above. This chapter's review of past R & D reveals efforts made on the modification of humidity sensor structures, introduction and modification of sensing materials, process optimization, and development of new sensing principles. There are two main types of operating principles for humidity sensors: capacitive and resistive types. They are mainly determined by the nature of the sensing materials used. Once materials are selected, an electrode structure can be determined. The common structures are interdigitated and parallel-plate electrodes. With the interdigitated electrode, the sensing material is placed on top of the electrodes. With the parallel-plate electrode, the sensing material is placed between the top and bottom electrodes. Sensing materials commonly used are ceramic and polymer based materials. They are selected on the basis of their

intended use. Other detection techniques have been attempted. They include surface acoustic wave (SAW) [2.1-2.5], piezoresistive type [2.6][2.7], field effect transistor (FET) [2.8][2.9] and optical methods [2.10][2.11]. A trend which should not be missed is the integration of a humidity sensor and its signal conditioning circuit on a single chip [2.12-2.14]. This can be achieved utilizing conventional IC fabrication technology. Humidity sensing methods such as psychrometry, dew point, gravimetric measurement and optical methods are not covered in this chapter because of the difficulty of miniaturization [2.12]. This chapter covers the definition of terms used in measuring humidity, the sensing mechanism of ceramic and polymer based sensors with some examples, also techniques such as SAW, piezoresistive, and FET types. Some integrated humidity sensors with signal conditioning electronic circuitry on chips are also described.

2.2. Definition

There are a number of different terms and units to express moisture and humidity. The main reason for this variety is that the need to measure moisture and humidity is different for different applications [2.15]. This thesis uses the definitions by Quinn [2.15].

- Absolute humidity, d_w (Mass/Vapor concentration)

$$d_w = \frac{M_w}{V_w + V_g} = \frac{M_w}{V} \tag{2.2.1}$$

where M_w: mass of water vapor, V_w: volume of water vapor, V_g: volume of dry gas(air) V: total volume occupied by a mixture of water vapor and dry gas (air). Unit (grams/m^3)

- Mixing ratio (Humidity ratio)

$$W = \frac{M_w}{M_g} \tag{2.2.2}$$

Ratio of the mass of water vapor M_w to mass of dry gas (air) M_g. Unit (kg/kg, grams/kg)

- Relative humidity

$$RH(\%) = \frac{\rho_w}{\rho_s} \times 100 \tag{2.2.3}$$

The ratio of the partial vapor pressure ρ_w to saturation vapor pressure ρ_s

- Specific humidity

$$q = \frac{M_w}{M_w + M_g} = \frac{W}{1+W} \tag{2.2.4}$$

The ratio of the mass of water vapor M_w to total mass occupied by a mixture of water vapor and dry gas (air) ($M_w + M_g$).

- Mole ratio

$$y = \frac{N_w}{N_g} \tag{2.2.5}$$

The ratio of the number of moles of water vapor N_w to mole of dry gas (air) N_g.

- Mole fraction

$$x = \frac{N_w}{N_w + N_g} = \frac{y}{1+y} \tag{2.2.6}$$

The ratio of the number of moles of water vapor N_w to mole of wet gas (air) ($N_w + N_g$).

- PPM by volume

$$PPM_v = \frac{V_w}{V_w + V_g} \times 10^6 = \frac{V_w}{V} \times 10^6 \tag{2.2.7}$$

The ratio of partial volume of water vapor V_w to partial volume occupied by a mixture of water vapor and dry gas (air) ($V_w + V_g$) multiplied by one million.

(Once this value is determined, it does not change with pressure or temperature.)

- PPM by weight

$$PPM_w = \frac{M_w}{M_g} \times 10^6 = W \times 10^6 \tag{2.2.8}$$

$$PPM_w = PPM_v \frac{m_w}{m_g} \tag{2.2.9}$$

where m_w is mole weight of water, m_g is mole weight of carrier gas.

- Dew point temperature – the temperature at which moist air is saturated. If this air is cooled down at constant pressure and constant vapor content below dew point temperature, condensation of water vapor begins.
- Frost point temperature – the temperature at which moist air begins to condense in the form of ice.

Absolute humidity is used in applications where the quantity of water required for a particular process is important, such as chemical and food processing.

Mixing ratio, volume percent and specific humidity are useful indicators when the content of water vapor is required. If water vapor is either an impurity or a defined component of a process gas mixture, these indicators are used.

Relative humidity (RH) is commonly used in Heating, Ventilation and Air Conditioning (HVAC) applications. RH is an indicator to know human comfort and indoor air quality. Process control personnel is also aware of the importance of RH because low RH can cause brittleness of materials and electrostatic problems while high RH can cause swelling and clumping [2.16].

Dew point and frost point are used to quantify the dryness of the gas. This helps the industrial processes at low temperature avoid moisture condensation. The dew point is also used as a measure of water vapor in industrial processes at high temperature, such as industry drying.

2.3. Ceramic-based humidity sensors

Ceramic type humidity sensors are classified into ionic, electronic, capacitive and solid-electrolyte types based mechanisms. Ceramics, in particular metal oxides, have advantages in terms of their mechanical strength, their resistance to chemical attack and their thermal and physical stability [2.17]. The main problem of ceramic humidity sensors is the need for periodic regeneration of heat cleaning to recover the humidity sensitive properties. This is due to the formation of stable chemisorbed hydroxyl groups (OH^-) on the surface, causing a progressive drift in the resistance of the ceramic humidity sensor [2.17]. It is possible to remove the hydroxyl ions by heating to above 400 °C [2.17]. The other issue is the irreversible sensor response caused by contamination on the ceramic surface by dirt, dust, oil, smoke, alcohol, chemical substances and so on. Sometimes this contamination can also be removed by heating. In the following subsections, the sensing mechanism of ionic, electronic, capacitive, and solid-electrolyte type humidity sensors and some past work are presented.

2.3.1. Sensing mechanism of ceramic types

(1) Ionic type

This type of sensor utilizes the change of ionic conductivity resulting from water absorption and desorption. The humidity-sensitive characteristics depend on the intrinsic conductivity of the materials used and the microstructure of the specimens [2.18]. Ionic-type oxide is related to both the chemisorption and physisorption of water molecules on the oxide surface as well as capillary condensation in the micropores of ceramics. Chemisorption causes dissociation of water molecules to form surface OH^- groups [2.18]. The hydroxyl group formed on the oxide surface layer of the grains features high local charge density and a strong electrostatic field. Furthermore, a proton reacts with an adjacent surface O^{2-} group to form a second OH^- group [2.20]. At high surface hydroxyl content, an absorbed water molecule is bonded to two hydroxyl groups. At low content, only a single bond is formed. Single bonded water molecules are easier

to reorient than the double-bonded ones. This results in an increase in protonic conductivity [2.18]. The physisorbed water easily dissociates to form H_3O^+ because of the high electrostatic fields in the chemisorbed layer. The first layer of physisorbed water molecules is characterized by double hydrogen bonding of a single water molecule. Water molecules in the succeeding physisorbed layers are only singly bonded and form a liquid-like network [2.20]. The conduction mechanism depends on the surface coverage of absorbed water. When only hydroxyl ions are present on the oxide surface, the charge carriers are protons as a result of hydroxyl dissociation. The protons hop between adjacent hydroxyl groups [2.20]. If surface coverage of water is not complete, H_3O^+ diffusion on the hydroxyl group dominates. However, proton hopping between adjacent water molecules in clusters still takes place. The easy dissociation of physisorbed water produces H_3O^+ groups due to the high electric field in the chemisorbed layer. This charge transport occurs when H_3O^+ releases a proton to a nearby water molecule, ionizing it and forming another H_3O^+, resulting in the proton hopping from one water molecules to another [2.20]. This process is known as the Grotthuss chain reaction. The morphology of ceramics influences water vapor absorption and desorption. The condensation of water vapor occurs as a result of capillary effect. The behavior of this condensation is a function of ceramic pore sizes and its distribution. Kelvin's equation given below can be used to evaluate the pore radius when capillary condensation occurs at a particular temperature:

$$r_k = \frac{2\gamma M}{\rho RT\, ln(P_S / P)} \qquad (2.3.1.1)$$

where r_k is the Kelvin radius, P is the water vapor pressure, P_s is the water-vapor pressure at saturation, and γ, ρ and M are the surface tension, density and molecular weight of water, respectively. The condensation occurs in all pores with radii up to r_k and under a constant pressure P [2.18]. The smaller the r_k, or the lower the temperature, the more easily condensation occurs. Pore size determines the response speed. Pore size above 1000 Å in diameter exhibits a fast response but pore size smaller than 100 Å in

diameter responds very slowly [2.18].

(2) Electronic type

This type of sensors is based on electron donation from the water molecules to semiconductive metal oxides [2.19]. Semiconductor-type sensors using metal oxides have been studied for high temperature applications, which require the temperature of greater than 100 °C [2.17]. Since the operating temperature of the sensors based on semiconductors is much higher than that of water physisorption, the observed change in electrical conductivity is based on the chemisorption of water molecules [2.20]. When water molecules are chemisorbed on semiconducting oxides, their resistivity varies, either decreasing or increasing according to the type of semiconducting oxides (n- or p-type) [2.20]. This indicates the transportation of electrons from water molecules to the oxide. The surface of a semiconductor absorbs oxygen ions in air, and these ions affect the resistivity of the oxide surface [2.20]. An oxidation reaction takes place between the absorbed oxygen and the introduced reducing gases, injecting electrons, thereby resulting in a decrease in resistivity for n-type semiconductors [2.20]. There are some investigations of mechanisms of electron transfer. When two hydroxyl groups are formed during the chemisorption reaction, there is no electron transfer to oxide with H^+ bonded to an oxide ion and OH^- to a metal ion [2.20]. The other mechanism is the electron donation from water molecules to perovskite-type oxides (ABO_3). The humidity sensitivity of perovskite-type oxides was attributed to the presence of surface defects with trapped electrons such as ionized oxygen [2.20]. Trapped electrons are liberated by the absorption of water molecules [2.20]. The microstructure of ceramics, such as surface and average particle size does not significantly affect semiconducting characteristics than that of the ionic type sensors [2.19]. A major problem of this type of sensor is that the humidity sensitivity is affected by the inflammable gases because changes in resistivity with the gases are analogues to the changes with moisture. [2.20].

(3) Capacitive type

This type of sensor consists of parallel-plate structure, either top electrode – porous ceramic – SiO_2 – silicon – ohmic contact electrode or top electrode – porous ceramic – bottom electrode. The materials used for this type are porous aluminium oxide (Al_2O_3) [2.29-2.31], and perovskite-type such as strontium lanthanum titanate (Sr_{1-x} La_x TiO_3) [2.32], strontium titanate-niobate ($SrNb_x$ $Ti_{1-x}O_3$) [2.34] and barium titanate ($BaTiO_3$) [2.33]. These materials can be measured in resistance variation as a result of interaction with moisture but capacitance variation is measured in this type, using parallel-plate structure.

If Al_2O_3 is used, anodization is necessary to form a porous structure after depositing aluminium. Ceramics such as Sr_{1-x} La_x TiO_3 and $SrNb_x$ $Ti_{1-x}O_3$ are usually deposited and followed by annealing to create the desired porous structure. Control of the micropores in the ceramic is important to determine sensing performance. These micropores influence physisorption and chemisorption of water molecules are responsible for humidity sensitivity. Similar to the previous mechanisms, capillary condensation also plays an important role in this type of sensors. The dielectric constant of the ceramic is proportional to water content [2.21].

(4) Solid-electrolyte

Solid-electrolyte type has also been investigated for high temperature applications. This type of sensor utilizes mainly the protonic conductivity of materials [2.20]. Electromotive force (e.m.f.) is the measure of the proton conductor type of solid-electrolyte as a result of variation of water vapor pressure. An e.m.f. appears between the electrodes causing a variation of current as shown in Fig. 2.1. The proton transfer occurs from higher vapor pressure side, which is the negative pole relative to lower vapor pressure side. The reactions at each electrode are described as follow [2.22]:

- Electrode with higher vapor pressure
  H_2O (g) → $2H^+$ (electrolyte) + $1/2O_2$ (g) + $2e^-$
- Electrode with lower vapor pressure
  $2H^+$ (electrolyte) + $1/2O_2$ (g) + $2e^-$ → H_2O (g)

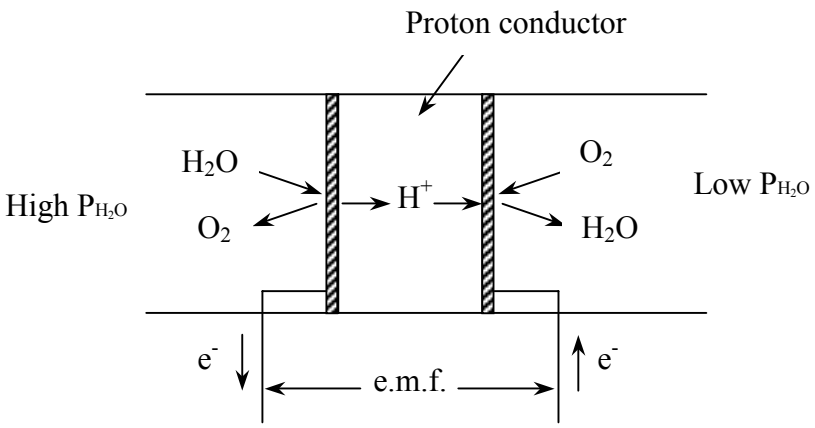

Fig. 2. 1. Concept of proton conduction in solid-electrolyte-type humidity sensor [2.20][2.22]

2.3.2. Example of ionic-type humidity sensor

Nitta et al. [2.23-2.25] developed a $MgCr_2O_4$-TiO_2 based porous ceramic humidity sensor for microwave ovens. This ceramic material reacts with water molecules through physisoption and chemisorption [2.24]. The porosity, average pore size, and average grain size of $MgCr_2O_4$-TiO_2 are 30 – 40 %, 3000 Å, and 1 – 2 μm, respectively. The structure of the sensor is shown in Fig. 2.2 and consists of the porous ceramic substrate with the electrodes of porous ruhenium oxide (RuO_2). The heater which surrounds the humidity sensor resets the sensitivity of the humidity sensor by heating it to about 450 °C each time the sensor is used. This heating is necessary after each use to eliminate the hydroxyl groups on the element surface which causes drift of the resistance of the ceramic [2.17]. In addition, the heater removes other contaminations such as an oil vapor and other organic vapors. Fig. 2.3 is the response curve of this sensor. The sensor is quite sensitive at low humidity range and shows an exponential decrease in the resistance as humidity increases. The temperature dependence is shown

in Fig. 2.3. A response speed of absorption was about 20s but the desorption took more than 100s [2.24]. The reaction test was also reported as shown in Fig. 2.4, which was tested up to the concentration of about 10^4 ppm with oxygen, hydrogen, ammonia and organic molecules containing function radicals such as hydroxyl, carbonyl, carboxyl, amino, and thiol. The conductivity decreased significantly with all gases listed except carbon monoxide, hydrogen and hydrocarbons. On the other hand, the conductivity increased with oxygen, which was the same direction as water vapor. The heater worked effectively to remove contaminations such as oil and other organic vapor.

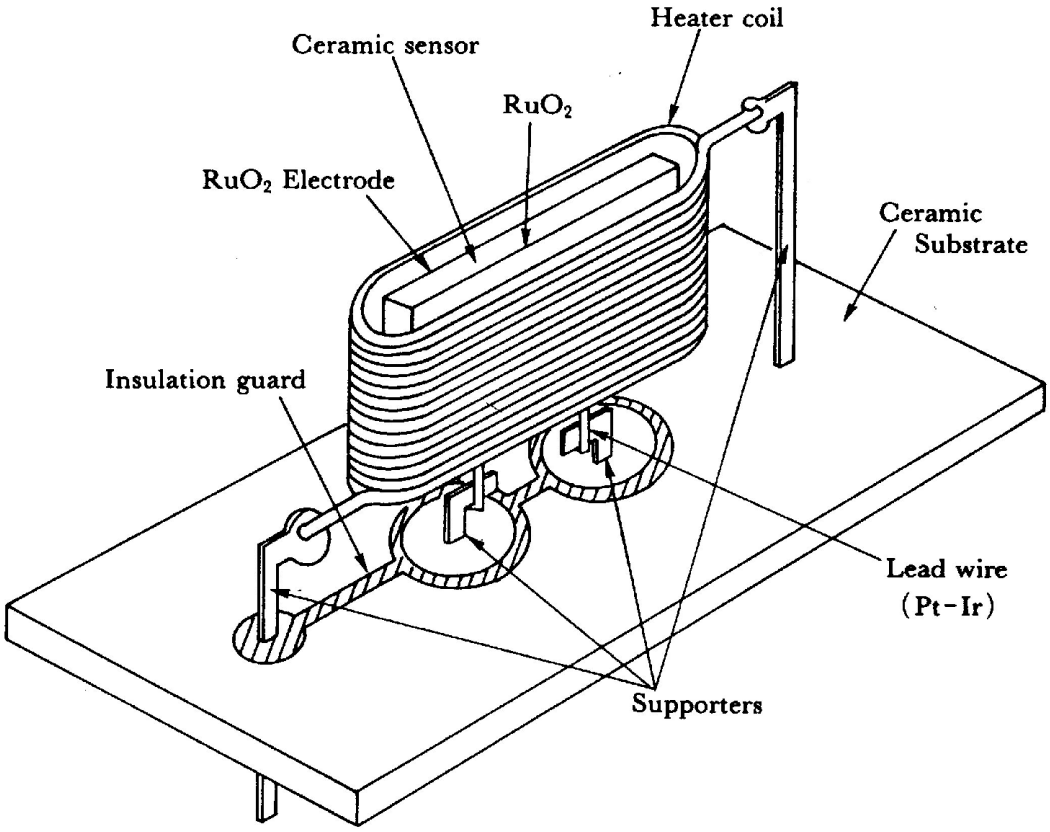

Fig. 2. 2. Constructed $MgCr_2O_4$-TiO_2 based ceramic sensor for ovens [2.24]

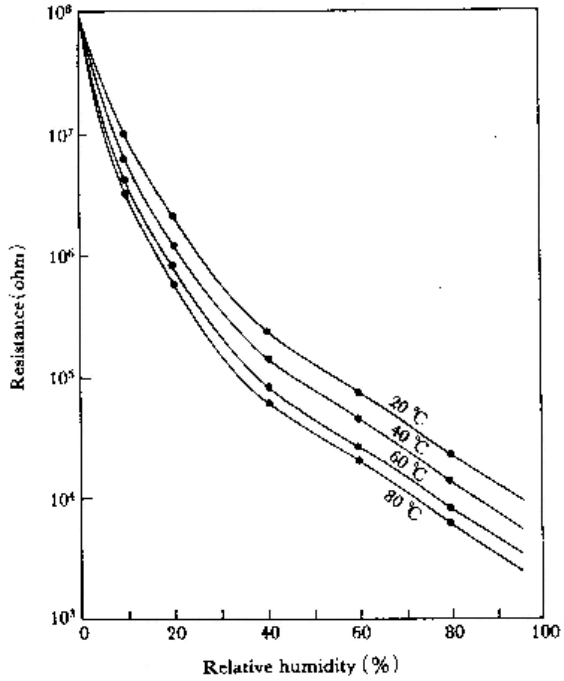

Fig. 2. 3. Temperature dependence of $MgCr_2O_4$-TiO_2 based humidity sensor [2.24]

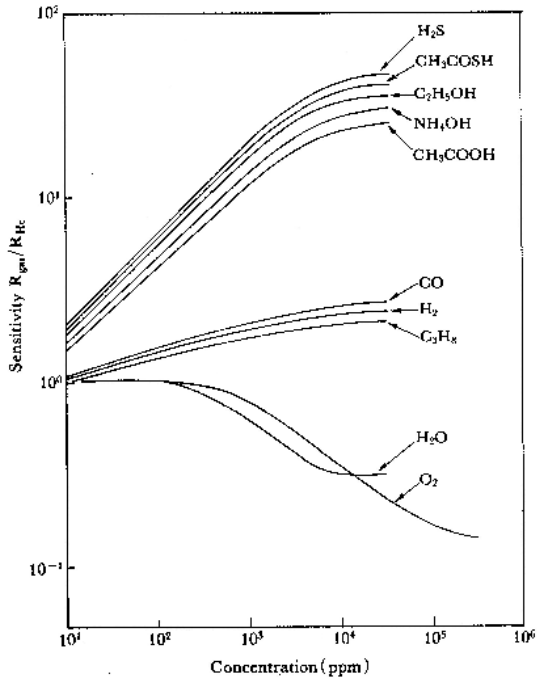

Fig. 2. 4. Resistance changes due to chemisorption of various gases [2.24]

Qu et al. [2.25] studied a $MnWO_4$ based porous ceramic sensor with a polarity reversed interdigitated electrode as shown in Fig. 2.5. The conventional thick-film technique was used to apply $MnWO_4$ on an alumina substrate resulting in an inexpensive process. LiCl was used as an adhesion promoter while sintering $MnWO_4$ instead of traditional glass frits. The LiCl allows the sintering at low temperature, 850 °C compared with the case using pure $MnWO_4$ paste 1300 °C. Interestingly, the amount of LiCl affected the shape of the response curve as Fig. 2.6 shows. The response curve with 5.0% LiCl is very different from the others. The authors pointed out that the higher the amount of LiCl, the more Li^+ ions the sensor has, resulting in smaller resistance at low humidity. The large amount of LiCl increases the ceramic density according to SEM investigation, which causes higher resistance at high humidity due to less moisture absorption. A temperature dependence was observed between 15 and

35 °C and is shown in Fig. 2.7. The reported response speed in absorption is 10s. This measurement was carried out when the sensor was quickly exposed from <15% RH to > 98% RH environment. Similarly, the contamination can be removed by heating at 400 °C to minimize the resistance drift.

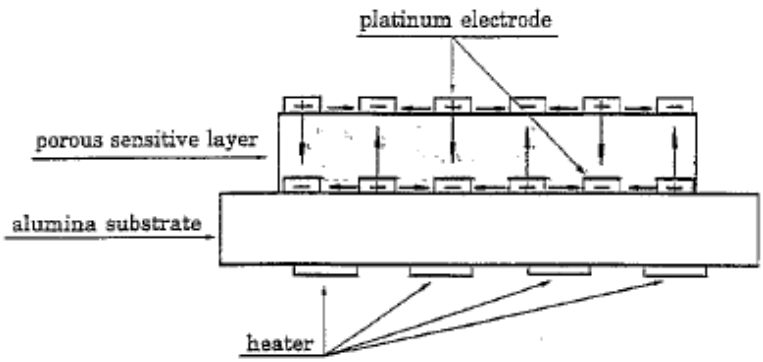

Fig. 2. 5. Cross-sectional view of humidity sensor with polarity reversed interdigitated electrode [2.25]

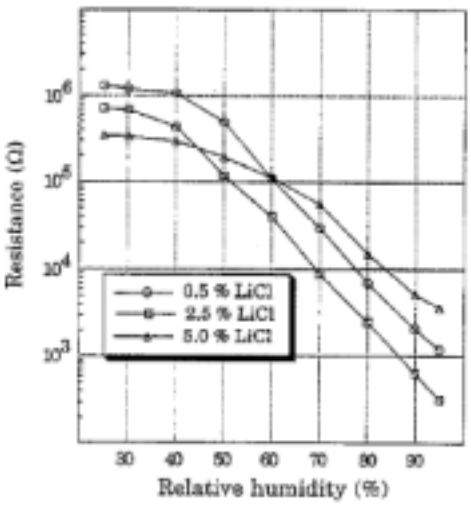

Fig. 2. 6. Effect of LiCr concentration on the resistance vs. relative humidity [2.25]

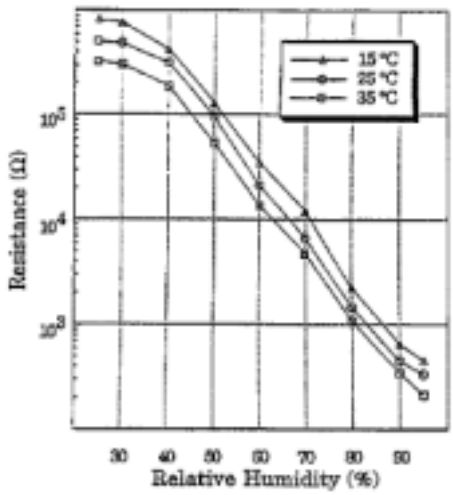

Fig. 2. 7. Temperature dependence of the resistance vs. relative humidity [2.25]

2.3.3. Example of electronic-type humidity sensor

Arai et al. [2.26] reported humidity sensitive characteristics in the perovskite-type oxides. The series of oxides, $CaTiO_3$, $CaSnO_3$, $SrTiO_3$ and $SrSnO_3$ were found to be moisture sensitive at 300 °C. $SrTiO_3$ showed the change from n-type to p-type semiconduction between 256 °C and 507 °C. The other materials behaved as n-type semiconductors. As humidity increased, the conductivity of n-type increased while p-type decreased. The absorption of electron-donating molecules results in a conductivity change, which is larger for n-type semiconductive oxides than that for p-type oxides [2.26]. This implies that n-type oxides are more suitable for humidity sensors. The conductivity ratio – humidity curve is shown in Fig. 2.8. Since the unsubstituted oxides given in the figure did not have the necessary sensitivity, partial substitution of lanthanum for calcium or strontium was made to improve the sensitivity. This improvement can be seen in Fig. 2.9. The partial substitution of the ions contributes the increase in concentration of electrons, hence the increase in conductivity [2.27]. The sensitivity to reducing gases at 1000 ppm was reported. The sensitivity of $Sr_{0.9}La_{0.1}SnO_3$ toward reducing gas; H_2, C_3H_8 and C_2H_5OH was higher than that toward water vapor.

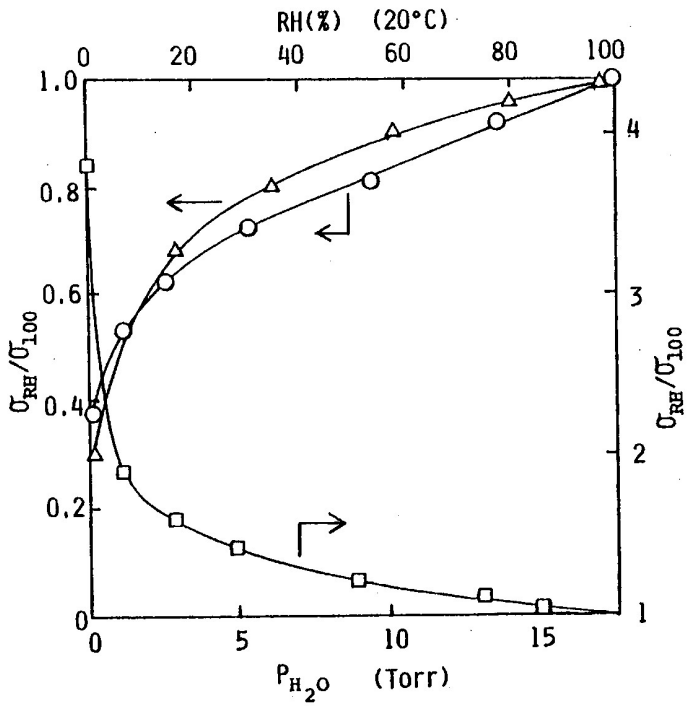

Fig. 2. 8. Conductivity ratio-humidity characteristics at 400 °C [2.26]

○ $SrSnO_3$, △ $Sr_{0.9}La_{0.1}TiO_3$, □ $SrTiO_3$

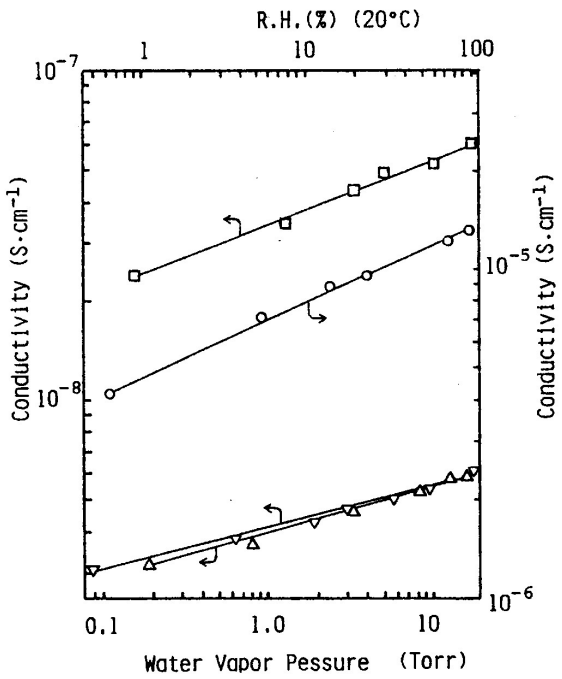

Fig. 2. 9. Dependence of electric conductivity of perovskite-type oxides on the water vapor content in air at 400 °C [2.26]

○ $Sr_{0.9}La_{0.1}SnO_3$, □ $Ca_{0.9}La_{0.1}TiO_3$
△ $Sr_{0.9}La_{0.1}TiO_3$, ▽ $Ca_{0.9}La_{0.1}TiO_3$

Nitta et al. [2.28] investigated ZrO_2 – MgO (n-type semiconductor) ceramic. This sensor operated even at 700 °C but the maximum vapor sensitivity was found between 450 °C and 550 °C. This sensor exhibited sensitivity towards alcohol and reducing gases such as hydrogen, ammonia, and carbon monoxide. Sensitivity to reducing gases remarkably reduced in air at temperatures greater than 500 °C [2.28]. Alcohol had an influence on sensitivity at any temperature but it did not affect detecting water vapor if an ambient atmosphere contained larger amounts of water vapor than alcohol. The response time taken in desorption was five times longer than that of the adsorption of water vapor. The slow response time of electronic-type sensors is due to the slow rate of chemisorption and the subsequent electron-transfer process on the oxide surface [2.17].

2.3.4. Example of capacitive-type humidity sensor

Some ceramics such as aluminum oxide (Al_2O_3), barium titanate ($BaTiO_3$), strontium lanthanum titanate (Sr_{1-x} La_x TiO_3), and strontium titanate-niobate ($SrNb_x$ $Ti_{1-x}O_3$) were used as capacitive type humidity sensors [2.29-2.34]. A common structure is either metal – insulator – metal or metal – insulator – semiconductor (MIS) as shown in Fig. 2.10. Insulator can be ceramic only or ceramic as well as SiO_2 located between the ceramic and the Si substrate.

Al_2O_3 was used as a dielectric to sense humidity [2.29-2.31]. Al_2O_3 was formed using reactive ion plating [2.29] or anodic oxidation [2.30][2.31]. The response of the sensor was significantly dependent on deposition rate, pressure and Ar-O_2 gas ratio in reactive ion plating [2.29]. Rogers et al. [2.30] reported that the sensor with anodized Al_2O_3 showed a large hysteresis at the first test cycle. The test cycle was carried out by increasing and decreasing humidity between 0% RH and 100% RH. The hysteresis decreased at the seventh cycle. This implies that aging affects hysteresis. The result of the aged sensor, which was boiled in distilled water for ten minutes prior to electrode formation showed the improvement of hysteresis. The improvement of hysteresis, however, reduced the sensitivity.

Fig. 2. 10. MIS structure of capacitive type ceramic humidity sensor

Nahar et al. [2.31] formed Al_2O_3 thin film using anodic oxidation technique in 10% sulphuric acid solution after aluminium deposition. It was found that the anodic current density exerted a significant influence on the sensor response. Sensors produced with the low current density, 10 mA/cm^2, exhibited low sensitivity in low humidity range and steep rise in high humidity range. On the other hand, sensors produced with the high current density, 20 mA/cm^2, exhibited improved sensitivity in low humidity range and suppressed the steep rise in high humidity range. In other words, a more linear response was achieved. If the anodization current density is increased, surface porosity of Al_2O_3 film decreases. That is, the anion content of the film increases.

Li et al. [2.32] has tested humidity response with Sr_{1-x} La_x TiO_3. A MIS structure was employed consisting of interdigitated top electrodes, Sr_{1-x} La_x TiO_3, SiO_2 as an insulator, and silicon as a substrate. This argon ion-beam sputtered Sr_{1-x} La_x TiO_3 film is an n-type semiconducting ceramic. This film exhibited temperature and light dependence but this dependence had little influence on the humidity measurement. The measurement made under ac current conditions is shown in Fig. 2.11. It is clear that the sensitivity is a strong function of ac input voltage at 0.5 kHz. That is, the larger the input voltage, the greater the sensitivity obtained. Non-linear response and hysteresis were observed at all applied voltages. The hysteresis is likely to originate from the effect of chemisorption because desorption of chemisorption require higher energy.

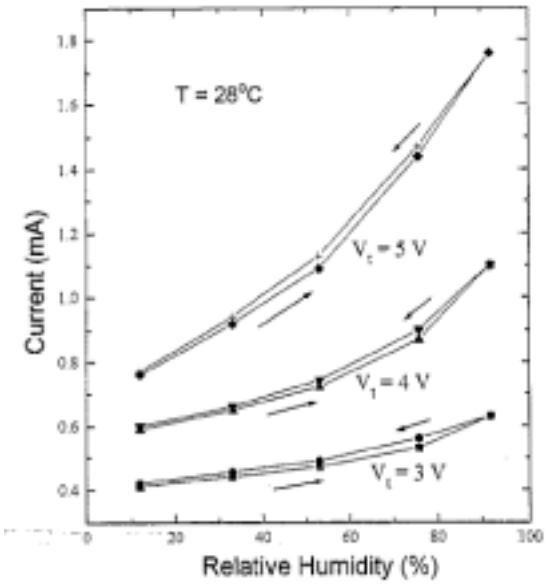

Fig. 2. 11. Current response as a function of relative humidity at various input voltages at 0.5 kHz [2.32]

2.3.5. Example of solid-electrolyte-type humidity sensor

Shuk et al. [2.35] studied $HZr_2(PO_4)_3$ as an impedance type solid-electrolyte film for humidity sensors. This material was used with the aim of high temperature applications. Interdigitated electrodes were formed on an alumina substrate. $HZr_2(PO_4)_3$ was printed over the electrodes using a thick-film technique. The resultant film indicated porous structure. The sensor responses in Fig. 2.12 were obtained under current measurement at 1 V. It is evident that the thicker film has larger sensitivity. The author repeated experiments up to 250 °C and commented on a good and reproducible response. The reported response speed is 10 – 15s.

Miura et al. [2.36] constructed an antimony phosphate ($HSb(PO_4)_2$) humidity sensor, exploiting protonic conductivity. This sensor constructed in parallel-plate structures showed an exponential decrease in resistance as the humidity increased. This sensor had a large sensitivity in the low humidity range and temperature dependence. These sensor responses can be seen in Fig. 2.13. Unlike semiconductor-type sensors, this sensor showed superior stability under the exposure of reducing gases such as H_2, CO, methane (CH_4), and propane (C_3H_8).

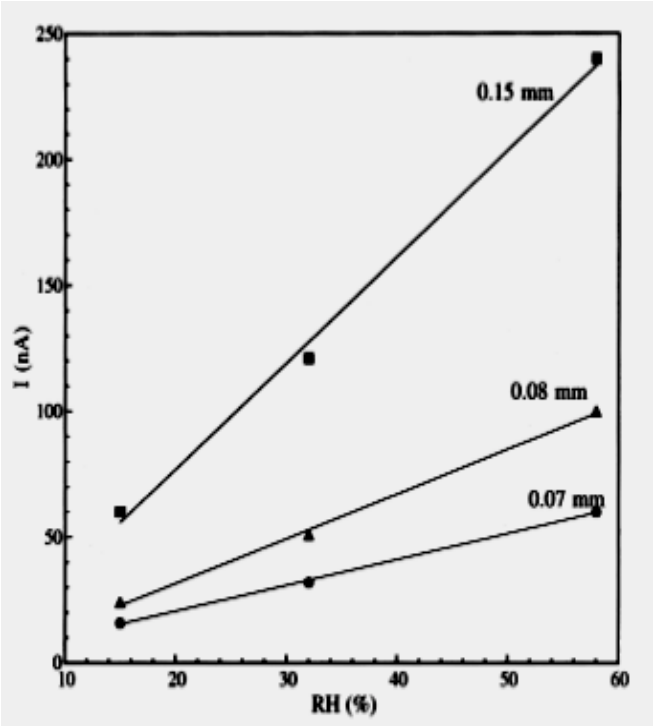

Fig. 2. 12. Sensor response as a function of film thickness [2.35]

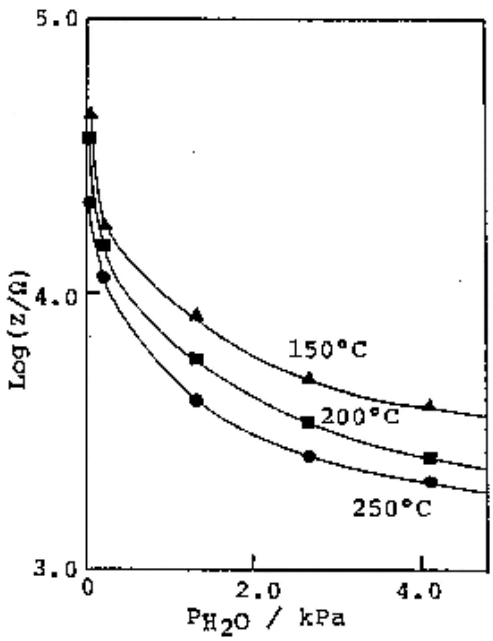

Fig. 2. 13. Dependence of impedance on water vapor pressure at various temperature [2.36]

2.4. Polymer-based humidity sensors

Polymer based humidity sensors have a longer history than that of ceramic sensors [2.37], and one of them was demonstrated using a plastic in the 1960's [2.38]. A variety of polymers has also been investigated and continue to be studied. Some polymers used as humidity sensing materials are listed in Table 2.1, classified as polyelectrolyte and dielectric types. The detection principle reported with the materials is capacitive, resistive, surface acoustic wave (SAW), and piezoresisitive types.

Table 2. 1. List of selected materials for polymer-based humidity sensors

	Sensing material	Ref.
Polyelectrolyte type	• Sodium sulphonated polystrene + cellulose-based polymer	[2.39]
	• Styrene sulfonate monomer	[2.40]
	• Sulfonated polystyrene branch grafted on tetrafluoroethylene (PTFE) film	[2.41]
	• Various copolymer of ionic and nonionic monomers	[2.42]
Dielectric type	• Polyimide	[2.6][2.45-2.53]
	• Polymethyl methacrylate (PMMA)	[2.54-2.56]
	• Poly(ethyleneterephthalate) (PET)	[2.57]
	• Polysulfone (PSF)	[2.58]
	• Cellulose acetate butyrate (CAB)	[2.59-2.61]
	• Polyethynylfluorenol (PEFl)	[2.62][2.63]

2.4.1. Sensing mechanism of polymer types

(1) Polyelectrolyte-type humidity sensor

Polymers with ionic monomers are classified as polyelectrolyte type. Ionic type materials exploit ionic conductivity, which increases as the humidity increases. Ionic mobility and/or charge carrier concentration is responsible for this type of mechanism [2.19]. The polyelectrolyte resin is a cross-linked structure with charged polar groups attached to the polymer chain. The charge is balanced by mobile ions of the opposite charge that are attracted to the fixed polar groups by electrostatic forces. When water is

absorbed by the material, the mobility of the electrostatically held ions increases, allowing transport to occur among neighboring sites more freely, and the resistance decreases accordingly [2.37]. Since polymer electrolyte is weak against water or dew condensation, crosslinking a hydrophilic polymer, copolymerization, or coating protective material has shown the improvement of durability [2.19][2.40].

(2) Dielectric-type humidity sensor

In dielectric type sensors, water molecules are bound at suitable sites in the polymeric network during absorption and desorption processes. Since the dielectric constants of water and polymers are about 80 and 5, respectively, the water molecules in polymer influence their dielectric constant. It can be expected that the dielectric constant increases as the content of water molecules in the polymers increases. If electrodes consist of a parallel-plate, the principle of operation of the capacitive type humidity sensor is based on a familiar expression defined as

$$C = \varepsilon_o \varepsilon_r \frac{A}{d} \tag{2.4.1}$$

where C is capacitance, A is area, d is thickness of polymer film, and ε_r is relative permittivity of polymer film. It is obvious that the sensor has a larger capacitance if the area increases or thickness of polymer film decreases. It is known that the dielectric constant of polymer film changes due to absorption or desorption of moisture into the film. Therefore, variation of capacitance as a result of a change in dielectric constant of the polymer film is measured.

(3) SAW type humidity sensor

Instead of sensing capacitance as a direct change of dielectric constant, other humidity sensing methods based on the SAW detection principle and piezoresistive transduction principle have been demonstrated. Their detection mechanisms utilize physical effects such as weight change of a polymer layer or polymer swelling.

The SAW detection technique has been used to measure humidity with the aid of the hygroscopic nature of the polymer. Acoustic devices are classified into five types

based on the propagation style of acoustic waves on the substrate: Rayleigh SAW, shear horizontal SAW (SH-SAW), Love wave mode, acoustic plate mode (APM), and flexural plate wave (FPW) [2.43]. Rayleigh SAW is useful for humidity detection because of a good functionality for mass loading type applications [2.43][2.44].

The type of acoustic wave is defined by the material properties of the substrate, crystal cut, and structure of electrodes, which form the transmitter and receiver of the acoustic waves. An interdigital transducer (IDT) which is an electrode formed on the piezoelectric substrate converts electrical energy into mechanical energy and vice versa. A pair of IDTs launch and detect the SAW. The typical SAW design can be represented as in Fig. 2.14. The distance between two neighboring fingers should be equal to half the elastic wavelength, which is given as

$$d = \lambda_R / 2 \tag{2.4.2}$$

where d is the distance between two neighboring fingers and λ_R is the elastic wavelength [2.43]. The frequency f_0 being launched is defined as

$$f_0 = v_R / \lambda_R = v_R / 2d \tag{2.4.3}$$

where v_R is the acoustic wave velocity. The formula (2.4.3) implies that the smaller the distance between two neighboring fingers, the higher the frequency generated.

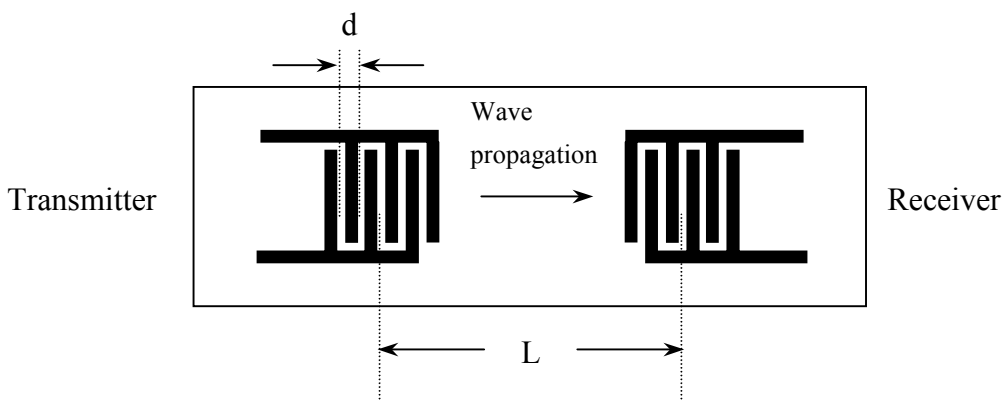

Fig. 2. 14. Interdigitated transducers in determination of acoustic wavelength

The operating bandwidth BW is determined by the number of finger pairs of IDT's, N and operating frequency f_o as [2.44]:

$$BW = f_o / N \tag{2.4.4}$$

The time delay τ equals the length of center-to-center separation of IDTs L divided by the acoustic wave velocity v_R [2.44],

$$\tau = L / v_R \tag{2.4.5}$$

When perturbation takes place on the wave propagation path, the change in the phase or the frequency of the wave can be measured. The change in the acoustic velocity v_R of the wave is related to the change in the resonant frequency f of the SAW as following [2.43][2.44]:

$$\frac{\Delta v_R}{v_R} = \frac{\Delta f}{f_o} \tag{2.4.6}$$

An increase in dielectric constant, mass, or electrical conductivity of humidity sensing materials resulting from absorption of moisture causes the decrease in velocity of SAW. A change in receiver output can result from a change in velocity, frequency or phase of the wave.

2.4.2. Example of polyelectrolyte-type humidity sensor

Hijikigawa et al. [2.40] reported the results of sensor response, durability against dewdrops and organic vapors, and long-term stability at different temperatures. Styrene sulfonate crosslinked with vinyl polymers was coated on an alumina substrate, on to which an interdigitated electrode was made beforehand. The response curve in Fig. 2.15 obtained when humidity was increased showed high sensitivity and linear response over a large humidity range. The dewdrop test was carried out by spraying or dipping the sensor into water and measuring the sensor response. The sensor showed very stable

output over 400 repetitions of the dewdrop test. The sensor also indicated good stability under the exposure of ethanol, acetone and ammonia. It is clear that the method of crosslinking improved the durability of the sensor made from polyelectrolyte type material. The contamination test was conducted with cigarette smoke and oil. The result showed that the sensor was not influenced by these contaminations due to the protection layer of cellulose ester. A long-term stability test was conducted under three different temperatures at room temperature, –20 °C and 80 °C, and high humidity condition in the range of 90 to 95% RH. Quite stable results were reported in all cases during test period of 2500 to over 3000 hours.

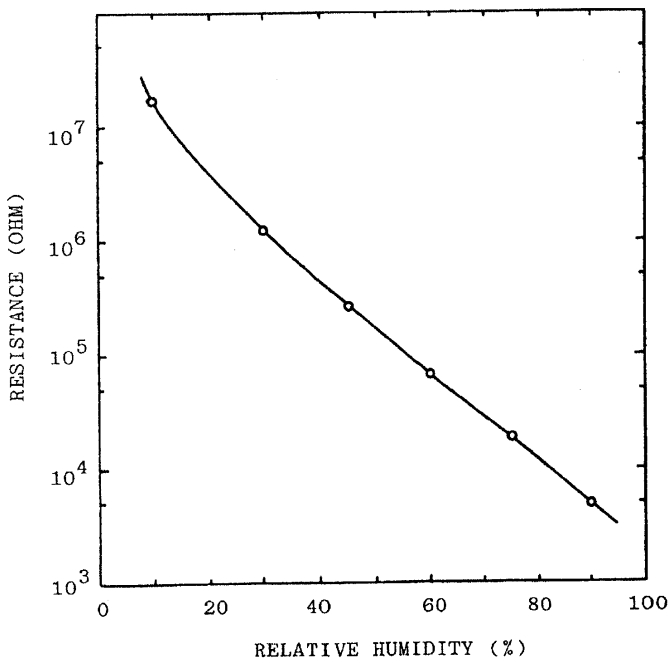

Fig. 2. 15. Sensor response as a function of film thickness [2.40]

2.4.3. Example of dielectric-type humidity sensor

Among the numerous possible polymers, one frequently used material is polyimide. The reason of this popularity is that polyimide is compatible with modern semiconductor fabrication processes and is high durability against chemical and contaminations. The polyimide has been used as an interlayer dielectric, a buffer layer and an overcoat in integrated circuits due to low dielectric constant and immunity against α particles.

Kang et al. [2.50] presented a novel structure to improve the response speed. Using multiple micro polyimide columns as Fig. 2.16 shows, response speed of 1.0s in increasing humidity was achieved. The increased surface area created with the cylindrical structure allows moisture to diffuse into the polyimide film quicker. The difference of type A, B and C in Fig. 2.17 is mainly the spacing and diameter of polyimide columns. The diameters of polyimide columns for each type are A=5 μm, B=10 μm, and C=15 μm. It is clear from the figure that sensor response is quite linear.

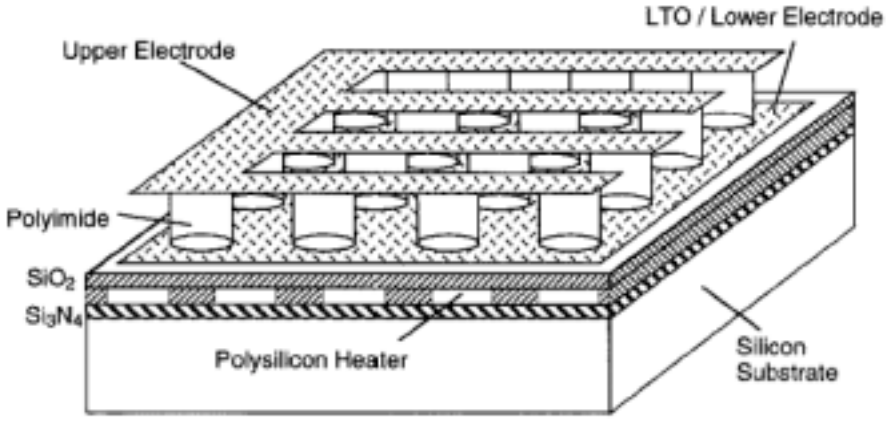

Fig. 2. 16. Schematic diagram of the high-speed capacitive humidity sensor [2.50]

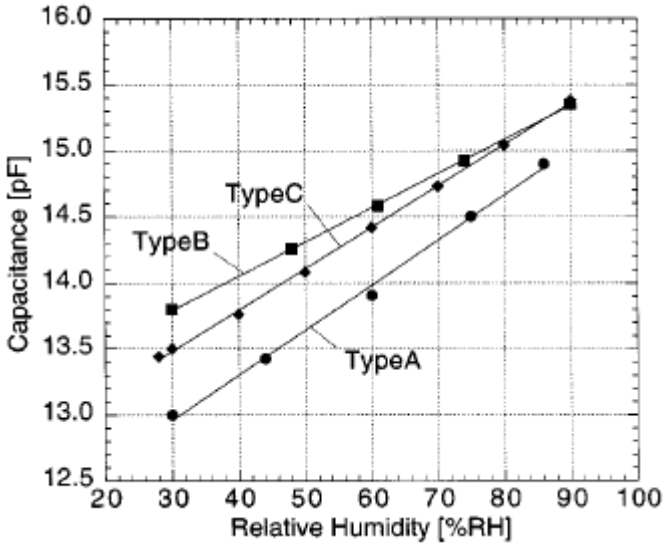

Fig. 2. 17. Sensor output as a function of relative humidity at room temperature with polyimide column diameters, A=5 μm, B=10 μm, and C=15μm [2.50]

Matsuguchi et al. [2.55] reported the results of durability of linear PMMA and crosslinked PMMA with ethylene glycol dimethacrylate at 90 °C and 170 °C. The test was conducted as follows. The sensor was exposed to acetone for 20min in a closed container for this test because acetone is a good organic solvent for PMMA. It was then placed in a humidity and temperature controlled vessel and the humidity varied from 0 to 90% RH and returned to 0% RH. This cycle was repeated three times. Drift was observed in all PMMAs but the crosslinked at 170 °C PMMA had very small drift. The crosslinked at 170 °C PMMA returned to almost original response at the third cycle but the others did not recover. The Figs. 2.18 and 2.19 are results of durability test carried out with linear and crosslinked PMMA, respectively. The crosslinked PMMA sensor showed the drift under the exposure to tabacco smoke, which was less than ±2% RH. This drift was disappeared after returning to an office environment.

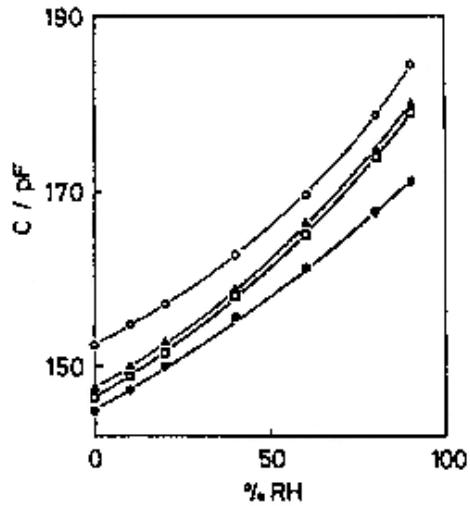

Fig. 2. 18. Durability of linear PMMA for acetone measured at 100 kHz, 30 °C in increasing RH. (●) initial value before exposure to acetone, (○) first measurement, (Δ) second, and (□) third measurement after exposure[2.55]

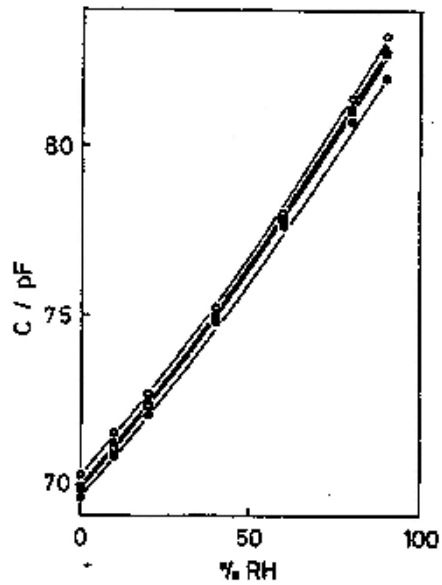

Fig. 2. 19. Durability of cross-linked PMMA with ED for acetone measurement at 100 kHz, 30 °C in increasing RH. The symbols are the same as in Fig. 2.18 [2.55]

Ralston et al. [2.54] investigated humidity sensors with PMMA treated in four different ways. Linear PMMA (no cross-linked), cross-linked PMMA with 4.9 wt.% ethylene glycol dimethacrylate (EGDM), low density plasma deposited PMMA (LD-PMMA), and high density plasma deposited PMMA (HD-PMMA) were used. The structure was parallel-plate with slotted top electrode. The responses were summarized as follow:

- Linear PMMA: linear response and the lowest hysteresis
- Cross-linked PMMA: nonlinear above 90% RH and hysteresis at high RH
- LD-PMMA: linear with very small hysteresis
- HD-PMMA: linear with largest hysteresis among the cases.

The authors commented that as the amount of cross-linking agent (EGDM) increased, the water sorption also increased. However, linear and cross-linked PMMAs did not show a distinct difference in sensitivity of the sensor.

A humidity sensor constructed with cellulose acetate butyrate (CAB) was investigated [2.59-2.61]. It featured high sensitivity to humidity, and good chemical and mechanical stability. Grange et al [2.60] reported hysteresis of the CAB-based humidity sensors. The hysteresis in the first test cycle was 3.5 – 7.5%, and the hysteresis in the second test cycle was 0.5 – 3%. In second test cycle, the sensor responded faster and showed less hysteresis. A 2-minute response time was reported until the sensor reached 98% RH. A small temperature dependence was found between 75 °F (23.8 °C) and 95 °F (35 °C) with an average temperature dependency of –0.72 pF/°C [2.59]. Typical response curves of a CAB sensor are shown in Fig. 2.20.

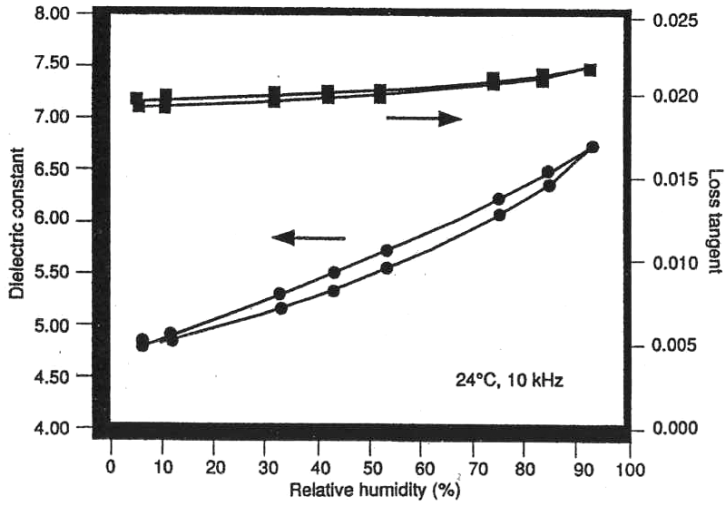

Fig. 2. 20. Electrical response of a thick-film CAB dielectric humidity sensor [2.37]

Pérez et al. [2.57] used pre-made PET film to sense humidity. PET thick-film was placed between thin gold electrodes forming a parallel-plate structure. The sensor response was fairly linear with a small temperature dependence between 25 and 35 °C as Fig. 2.21 shows. The response time was about 7 min until relative humidity reached to 85% RH from 12% RH. Exceptionally good stability of the sensor was reported over 280 days test as Fig. 2.22 shows. The authors reported a variation of output of ± 0.1 kHz.

Kuroiwa et al. [2.58] reported humidity sensor with PSF. PSF features good electrical characteristics at high frequency and durability against hot steam due to the chemical structure of diphenyl sulfone group [2.58]. This sensor was tested at 100 kHz and exhibited +0.8% RH linearity, 0.5% RH hysteresis, 0.0±0.1% RH/°C over the range of 10 to 90% RH [2.58]. PSF certainly has good material characteristics but it has to be dissolved in a hot mixed solvent of cyclohexanone, N,N-dimethylformanide and methyl ethyl ketone prior to use.

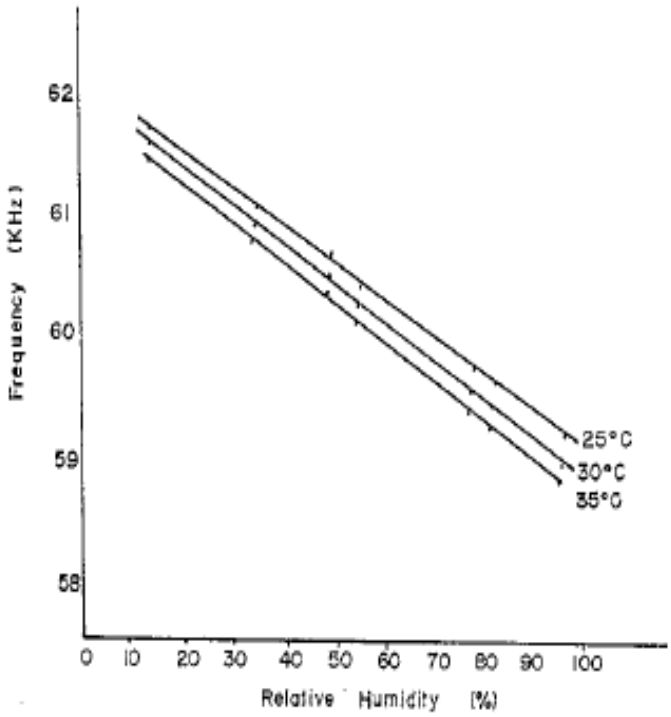

Fig. 2. 21. Temperature dependence at 25, 30, and 35 ˚C of PET film humidity sensor [2.57]

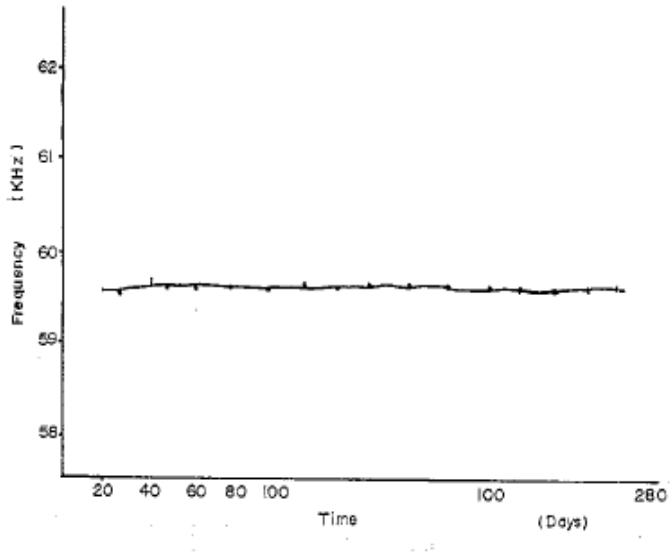

Fig. 2. 22. Stability of the PET film humidity sensor. The sensors was continuously operated at humidity of 80% RH at 25 °C [2.57]

2.4.4. Example of SAW and piezoresistive-type humidity sensors

Humidity sensors based on the SAW principle have been demonstrated using IDTs on top of piezoelectric substrate [2.1-2.4]. Polymers such as polyimide [2.1], PEFl [2.2], cellulose acetate [2.3], and polyvinyl-alcohol (PVA) [2.4] can be coated on entire substrates covering IDTs or only on the wave propagation path between the IDTs.

Penza et al. [2.4] demonstrated a SAW based humidity sensor constructed on 128°YX-$LiNbO_3$ substrate with PVA spin-coated over the wave propagation path and IDTs. The sensor fabricated is shown in Fig. 2.23. Good repeatability, good water resistance, low hysteresis at room temperature and relatively large temperature dependence between 20 °C and 60 °C were reported. The result of phase measurement as a function of relative humidity in Fig. 2.24 shows a nonlinear response with small hysteresis. The authors commented that this nonlinear behavior resulted from disproportionate swelling of PVA with water vapor content, causing structural changes in PVA film. Negligible cross sensitivity toward NH_3, NO_2, CO and H_2 but some sensitivity toward organic vapor such as ethanol and methanol was reported.

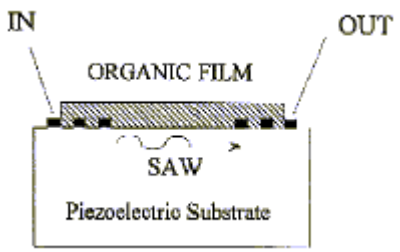

Fig. 2. 23. Schematic of SAW structure with PVA film for humidity detection [2.4]

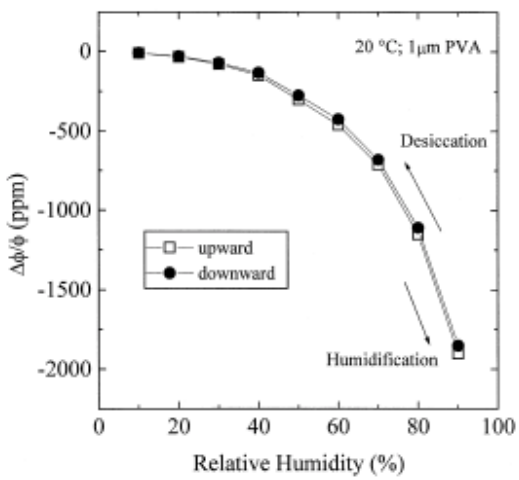

Fig. 2. 24. Hysteresis curve of SAW RH sensor using PVA film at room temperature [2.4]

Caliendo et al. [2.62] used PEFl for detecting humidity based on SAW principle. PEFl was spun onto an ST-cut, x-propagation quartz substrate. IDTs were formed on top of it, serving an operation frequency of 154 MHz. PEFl is also used for a resistive type sensor due to doping with $SnCl_2$ in 50% wt./wt. ratio [2.63]. After synthesizing PEFl, it was dried and dissolved in CH_2Cl_2 prior to spin coating. Non-linear response and temperature dependence between 30 °C and 60 °C were reported.

A novel technique used to detect humidity is the piezoresistive transducer [2.6]. Silicon was underetched to form a silicon diaphragm as in Fig. 2.25. Polyimide was located on top of the diaphragm. P^+ piezoresistors in the diaphragm form the Wheatstone bridge. This sensor is based on the swelling effect of polyimide to detect humidity. Absorption of moisture causes polyimide to swell and produce strain on the piezoresistors. The two types of polyimide layers were defined; type A consists of polyimide layer covering the entire membrane, type B consists of polyimide layer defined and located only over the piezoresistors. Type A and type B sensors achieved the sensitivity of 20 – 25 μV/% RH and 80 –100 μV/% RH, respectively [2.6]. This implied that type B sensor deforms the diaphragm more. The fairly linear response was also reported over 10 – 95% RH.

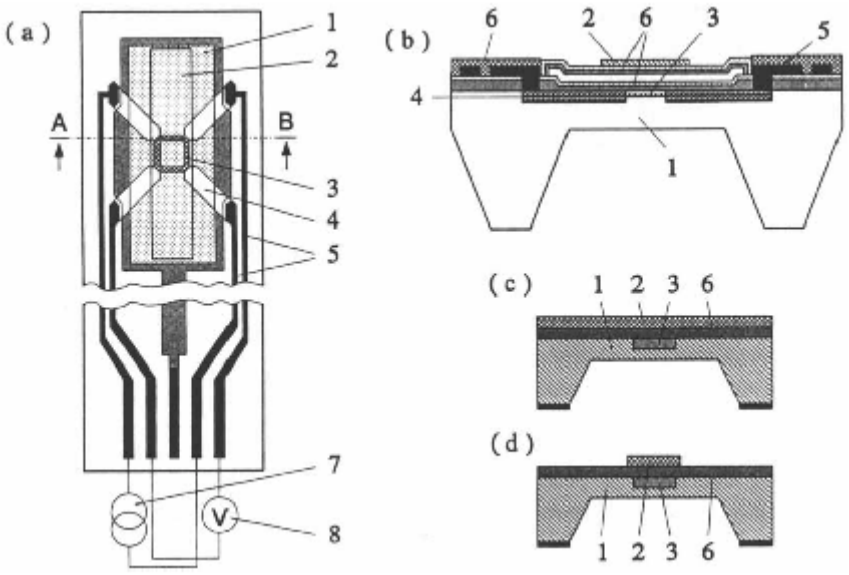

Notations: 1. silicon membrane, 2. polyimide layer, 3. piezoresistors, 4. implanted connections, 5. metallized connections, 6. passivation layer system, 7. current supply, 8. sensor output voltage

Fig. 2. 25. Schematic of the piezoresistive humidity sensor: (a) layout, (b) passivation layer system, (c-d) cross sectional view of type A and type B sensors, respectively between cross sections A and B. [2.6][2.7]

2.5. Porous silicon type

One of the humidity sensors whose fabrication can be done by conventional IC fabrication techniques with additional processes is based on porous silicon as a humidity sensing layer [2.64-2.67]. Porous silicon for vapor sensing is attractive because of increased interfacial area of the silicon. The process required to form porous silicon may employ special methods such as anodization [2.65]. Anodization can be carried out in 25% hydrofluoric (HF) solution mixed with ethanol at a constant current density of 13 mA cm^{-2} for 120s [2.65]. After this process, the silicon is converted to porous silicon. The porosity and pore size of porous silicon are important factors because they determine the sensitivity and response speed of the sensors. The porosity and pore size are controlled by doping concentration of silicon, concentration of HF

solution, and current density [2.68][2.69].

The structure presented by Kim et al. [2.65] is mesa structure as shown in Fig. 2.26.

(a) Cross-sectional view (b) Top view

Fig. 2. 26. Porous silicon humidity sensor [2.65]

The advantage of this structure is that the effect of the parasitic capacitance from other layers can be removed because both electrodes directly make contact to the porous silicon layer. At the low frequency, permittivity is significantly influenced by the orientational polarization due to induced dipole moment. This causes larger increase of the permittivity of the porous silicon layer. The measured capacitance increased by 300% at 95% RH with the application of 120 Hz signal. The response showed that the sensors had much lower sensitivity at low relative humidity than that at high humidity. This non-linearity is clear in Fig. 2.27. This nonlinear behavior is likely to be associated with a capillary effect in pores due to water condensation. The authors conducted measurements on temperature dependence and concluded that the porous silicon humidity sensor had negligible temperature dependence.

Other characteristic to note related to the porous silicon type humidity sensors is that the increased permittivity in the space charge region due to condensation within the pores may cause the large sensitivity [2.66]. Moreover, condensation in pores seems to cause large hysteresis. This can be improved with a heater attached to the substrate [2.67]. Even though porous silicon indicates very large sensitivity toward moisture, slow response times and large hysteresis are a significant disadvantage.

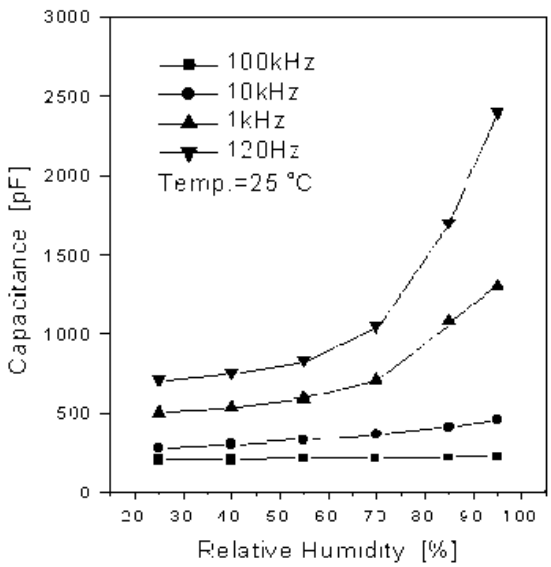

Fig. 2. 27. Response of porous silicon humidity sensor at four different frequencies at room temperature [2.65]

2.6. Single chip integration solution

Humidity sensors in this category can be classified in two types in accordance with the role of humidity sensor to generate output signal in conjunction with electronic circuitry. One type is that a humidity sensor is a part of a transistor such as field effect transistor (FET) [2.8][2.9]. The other type is where the sensing element is not a part of a transistor but integrated with signal conditioning circuitry such as an amplifier, buffer or comparator on the same die [2.12-2.14].

Advantages of the integrated sensor with signal conditioning circuitry or FET type are low cost due to batch fabrication with conventional IC technology and enhancement of sensor performance. Even though the conventional IC process technology allows cost effective batch processes, limitations of available materials and the process sequence affect the flexibility of designing humidity sensors with on-chip circuitry. Some past work employed polymer as a humidity sensing element to meet the conventional IC process as close as possible [2.8][2.12-2.14]. Among them, polyimide is absolutely compatible with the conventional IC process in industries [2.12-2.14].

The technique which incorporates a humidity-sensing element in gate of FET has been

reported [2.8][2.9]. Some of reported materials are CAB [2.8] and TiO_2 [2.9].

Hijikigawa et al. [2.8] developed a FET type humidity sensor with temperature sensing diode. The fabricated sensor was based on Insulated Gate Field Effect Transistor (IGFET) featuring n-channel enhancement mode. Humidity sensing element consists of CAB (1 μm thick) in gate, which is responsible for the change in capacitance. The mechanism of humidity detection is that the change in capacitance of CAB causes the change of ac signal applied. This varies the gate voltage, resulting in the change in drain current of IGFET. They pointed out the drift problem of output signals due mainly to various mobile charges existing in the gate insulator and the sensing material. The solution to this problem presented is called duplex-gate electrode structure. This structure consists of two gate electrodes; one is on top of the humidity sensor, the other is on top of gate insulators. The cross-sectional view and the equivalent circuit of the sensor are shown in Fig. 2.28. As Fig. 2.29 shows, the stability of the drift improved with the duplex-gate electrode. The output signal, V_{out}, is defined by:

$$V_{out} = v_o R_L g_m / (1 + C_i / C_S) \tag{2.6.1}$$

where v_o is ac input signal, R_L is the load resistor, g_m is the transconductance in saturation region of the drain current, C_i is the capacitance of the gate insulator and C_s is capacitance of humidity sensor. Fig. 2.30 shows the sensor response with 10 kHz signal and an external resistance of R_B = 10 MΩ at 25 °C. The linear response below 80% RH, ±3% RH accuracy and less than 30s response speed were reported.

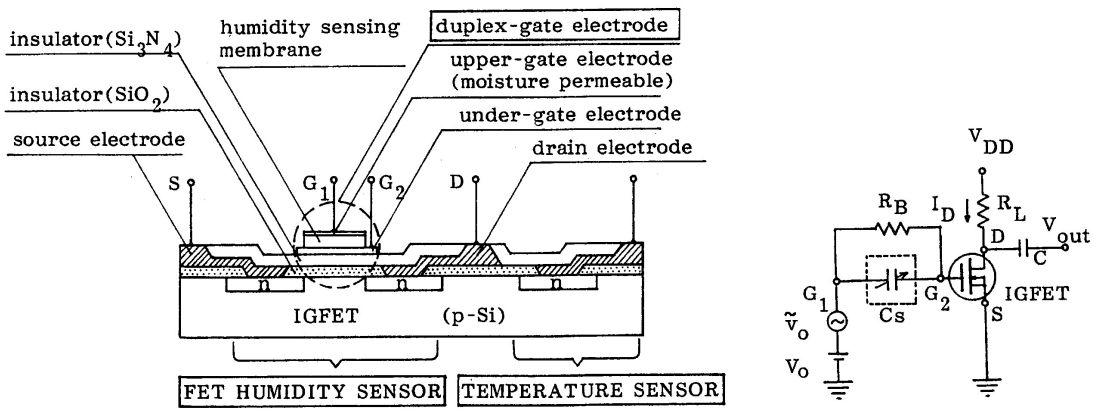

(a) Cross section of FET humidity sensor (b) Equivalent circuit

Fig. 2. 28. FET humidity sensor with CAB [2.8]

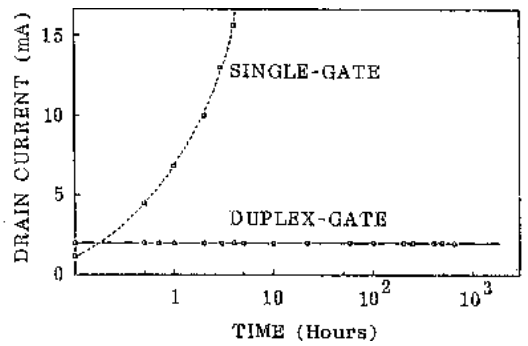

Fig. 2. 29. Stability of drain current at V_O=2.5 volts (D.C.) for FET humidity sensor with a 'duplex-gate' electrode or 'single-gate' electrode [2.8]

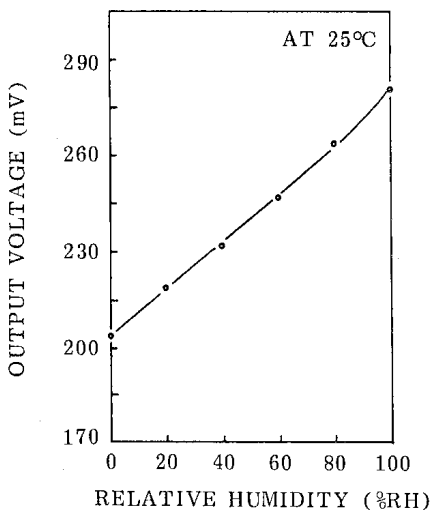

Fig. 2. 30. Output characteristic of FET humidity sensor measured at 25 °C [2.8]

Boltshauser et al. [2.13] reported the signal conditioning circuitry based on charging or discharging current. The circuitry was fabricated under CMOS process. Polyimide was coated as a post-processing step. The circuit produces an output current which is a function of reference voltage, clock frequency and sensor capacitance. The typical result between 30% RH and 95% RH is provided in Fig. 2.31.

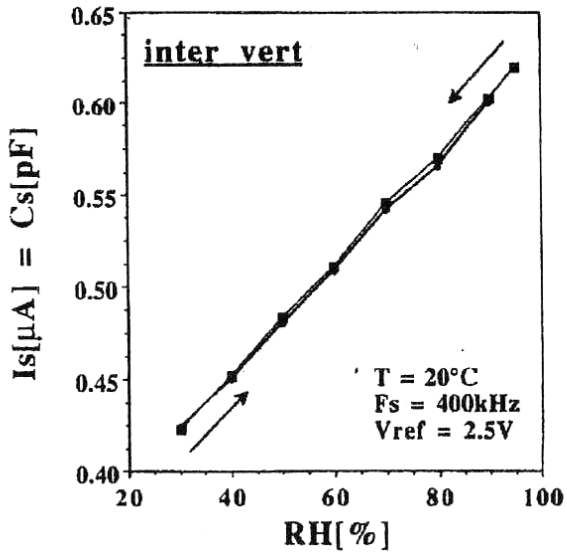

Fig. 2. 31. Hysteresis curve [2.13]

Qiu et al. [2.12] reported a humidity sensor with on-chip calibration circuit fabricated based on CMOS process. Polyimide was coated as a post processing step. The function of the circuit is charge-to-voltage conversion, using the switched-capacitor technique. The circuit diagram is shown in Fig. 2.32. This technique requires the reference capacitor consisted of oxide and capacitive humidity sensor consisted of polyimide. The output voltage is a function of the difference of capacitance of the reference capacitor and the humidity sensor as well as reference voltages. The fabricated chip and the result can be seen in Figs. 2.33 and 2.34. The calibration of the circuit was determined by sensor sensitivity and sensor offset. The maximum deviation after calibration was reported as 1.7% RH between 0 and 100% RH.

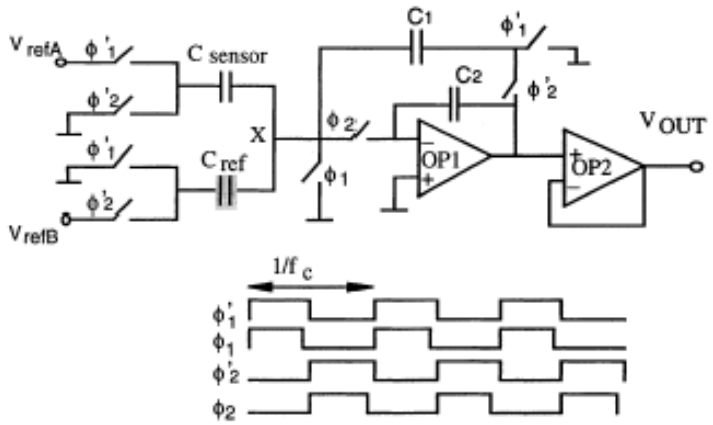

Fig. 2. 32. Sensor interface circuit [2.12]

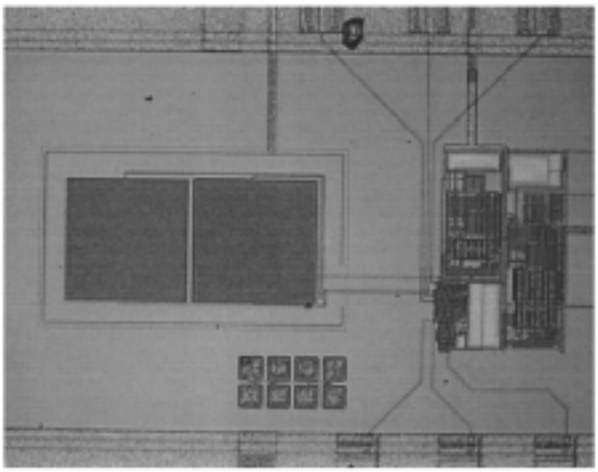

Fig. 2. 33. Photograph of chip after post-processing polyimide [2.12]

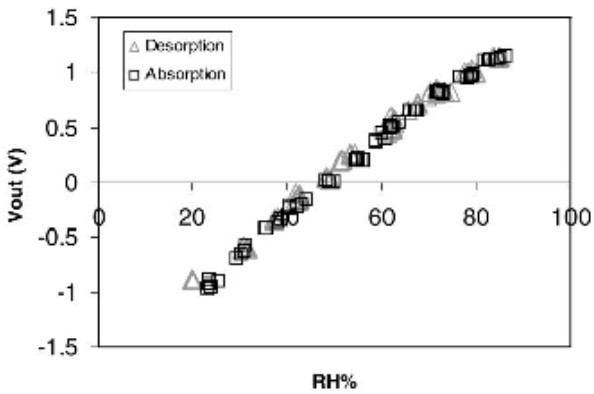

Fig. 2. 34. Typical hysteresis measurement with polyimide (PI2160) at V_{refA}=3 V [2.12]

2.7. Conclusions

Humidity sensing mechanisms of a wide variety of material types have been presented in this thesis. A summary classifying the material and sensing mechanism is listed in Table 2.2. The research reviewed was dedicated mainly to the use of new materials, new process schemes, design optimization of the structure, modification of materials and process methods in order to meet the demands of various applications. It is difficult to precisely conclude performance characteristics of all types of humidity sensors. For example, the performance of polymer-based sensor depends not only on material characteristics but also electrode design, thickness of polymer layer and physical patterning of the polymer layer. However, it is worth noting typical characteristics of humidity sensors to help select technologies suitable for particular applications.

The trend toward integration of the sensor as well as signal conditioning circuitry on-chip makes it possible to produce small size and cost effective humidity sensors using IC compatible materials. In polymer types, polyimide readily serves as a solution for integrated humidity sensor with on-chip signal conditioning circuitry. From this review, there is no perfect solution to serve all requirements stated in the subsection 2.1. In conclusion, it can be emphasized that the selection of material, sensing mechanism and structure of the sensors is very much dependent on the intended application.

In this thesis work, it was decided to progress the use of polyimide as a sensing material in a capacitive measurement configuration for the following reasons:

(a) Conventional IC process compatibility

(b) Negligible temperature dependence

(c) Good resistance against chemical contamination

This is discussed, and results are presented in the next chapter.

Table 2. 2. Typical sensors characteristics

Material category	Sensing mechanism	Advantage	Disadvantage
Ceramics	Ionic	• From low to high temperature applications (> 150 °C)	• Periodic cleaning at high temperature • Large temperature dependence • Sensitive to reducing gases
	Electronic	• From low to high temperature applications (> 150 °C)	• Periodic cleaning at high temperature • Large temperature dependence • Sensitive to reducing gases
	Solid-electrolyte	• High temperature application • Less sensitive to reducing gases	• Large temperature dependence
Polymer	Polyelectrolyte	• Small temperature dependence • Small drift	• Not suitable for high temperature applications • Crosslinking or copolymerization is required • Weak against contaminations • Resistance is very high in very dry region.
	Dielectric (Polyimide & CAB)	• Stable wide measuring range (0 to 100% RH) • No periodic cleaning at high temperature • Superior temperature and chemical stability • Small temperature dependence	• Not suitable for high temperature applications • Some long-term drift • Slow response speed • Relatively large hysteresis
Porous silicon		• Very high sensitivity • Small temperature dependence	• Slow response • May require heater to reset • Highly non-linear

References

[2.1] P.R. Story, D.W. Galipeau, and R.D. Mileham, "A study of low-cost sensors for measuring low relative humidity", *Sens. Actuators B*, vol. 24-25, 1995, pp. 681-685

[2.2] C. Caliendo, E. Verona, A. D'Amico, A. Furlani, G. Iucci, and M.V. Russo, "A new surface acoustic wave humidity sensor based on a polyethynylfluorenol membrane ", *Sens. Actuators B*, vol. 18-19, 1994, pp. 82-84

[2.3] T. Nomura, K. Oobuchi, T. Yasuda, and S. Furukawa, "Humidity sensor using surface acoustic wave delay line with hygroscopic dielectric film", *Jpn. J. Appl. Phys.*, vol. 32, Sept. 1993, pp. 4205-4208

[2.4] M. Penza, and V.I. Anisimkin, "Surface acoustic wave humidity sensor using polyvinyl-alcohol film", *Sens. Actuators* A, vol. 76, 1999, pp. 162-166

[2.5] K.A. Vetelino, P.R. Story, R.D. Mileham, and D.W. Galipeau, "Improved dew point measurements based on a SAW sensor", *Sens. Actuators B*, vol. 35-36, 1996, pp. 91-98

[2.6] G. Gerlach and K. Sager, "A piezoresistive humidity sensor", *Sens. Actuators A,* vol. 43, 1994, pp. 181-184

[2.7] Z.M. Rittersma, "Recent achievements in miniaturized humidity sensors – a review of transduction techniques", *Sens. Actuators A,* vol. 96, 2002, pp. 196-210

[2.8] M. Hijikigawa, T. Sugihara, J. Tanaka and M. Watanabe, "Micro-chip FET humidity sensor with a long-term stability", *IEEE 3rd Int. Conf. on solid-state sensors and actuators (Transducers '85)*, Philadelphia, PA, U.S.A., 11-14 June 1985, pp. 221-224

[2.9] S.P. Lee and K.J. Park, "Humidity sensitive field effect transistor", *Sens. Actuators B*, vol. 35-36, 1996, pp. 80-84

[2.10] J. Fraden, *Handbook of modern sensors: physics, design, and applications*, New York: Springer-Verlag, 1996, p.392

[2.11] S. Muto, O. Suzuki, T. Amano, and M. Morisawa, "A plastic optical fiber sensor for real-time humidity monitoring", *Meas. Sci. Technol*. vol. 14, April 2003, pp. 746-750

[2.12] Y.Y. Qiu, C. Azeredo-Leme, L.R. Alcácer, and J.E Franca, "A CMOS humidity sensor with on-chip calibration", *Sens. Actuators A*, 92, pp.80-87, 2001

[2.13] T. Boltshauser, C. Azeredo Leme and H. Baltes, "Hight sensitivity CMOS humidity sensors with on-chip absolute capacitance measurement system", *Sens. Actuators B*, vol 15-16, 1993, pp. 75-80

[2.14] S.V. Silverthorne, C.W. Watson and R.D. Baxter, "Integrated relative humidity sensor", *Technical Digest of Solid State Sensor and Actuator Workshop*, Hilton Head Island, SC, USA, 6-9 June 1988, pp.67-71

[2.15] F.C. Quinn, "The most common problem of moisture/humidity measurement and control", *Proc. of 1985 International symposium on moisture and humidity*, Apr. 1985, Washington DC, pp. 1-5

[2.16] Reference and application data, Humidity sensor HIH series, Honeywell, p.145

[2.17] E. Traversa, "Ceramic sensors for humidity detection: the state-of-the-art and future developments", *Sens. Actuators B* 23, 1995, pp. 135-156

[2.18] T. Seiyama, N. Yamazoe and H. Arai, "Ceramic humidity sensors", *Sens. Actuators*, vol. 4, 1983, pp. 85-96

[2.19] N. Yamazoe, and Y. Shimizu, "Humidity sensors: principles and applications", *Sens. Actuators*, vol. 10, 1986, pp. 379-398

[2.20] E. Traversa, "Ceramic sensors for humidity detection: the state-of-the-art and future developments", *Sens. Actuators B*, vol. 23, 1995, pp. 135-156

[2.21] G.Q. Li, P.T. Lai, M.Q. Huang, S.H. Zeng, B. Li, and Y.C. Cheng, "A humidity-sensing model for metal-insulator-semiconductor capacitors with porous ceramic film", *J. Appl. Phys.*, vol. 87, no. 12, June 2000, pp. 8716-8720

[2.22] H. Iwahara, H. Uchida, K. Ono and K. Ogaki, "Proton conduction in sintered oxides based on $BaCeO_3$", *J. Electrochem. Soc.* vol. 135, no. 2, Feb. 1988, pp. 529-533

[2.23] T. Nitta and S. Hayakawa, "Ceramic humidity sensors", *IEEE Trans. Components, Hybrids, and Manufacturing Technology*, vol. CHMT-3, no. 2, June 1980, pp. 237-243

[2.24] T. Nitta, "Development and application of ceramic humidity sensors", *Chemical Sensor Technology*, vol. 1, Kodansha, Tokyo/Elsevier, Amsterdam, 1988, pp. 57-78

[2.25] W. Qu and J. Meyer, "A novel thick-film ceramic humidity sensor", *Sens. Actuators B*, vol. 40, 1997, pp. 175-182

[2.26] H. Arai, S. Ezaki, Y. Shimizu, O. Shippo, and T. Seiyama, "Semiconductive humidity sensor of perovskite-type oxides", *Analytical Chemistry Symposia Series; Chemical Sensors*, vol. 17, Kodansha, Tokyo/Elsevier, Amsterdam, 1983, pp. 393-398

[2.27] Y. Shimizu, M. Shimabukuro, H. Arai and T. Seiyama, "Humidity-sensitive characteristics of La^{3+} - doped and undoped $SrSnO_3$", *J. Electrochem. Soc.*, vol. 136, no. 4, pp. 1206- 1210, April 1989

[2.28] T. Nitta, F. Fukushima and Y. Matsuo, "Water vapor gas sensor using ZrO_2 – MgO ceramic body", *Analytical Chemistry Symposia Series; Chemical Sensors*, vol. 17, Kodansha, Tokyo/Elsevier, Amsterdam, 1983, pp. 387-392

[2.29] Y. Nabeta, K. Suzuki and T. Inuzuka, "Characteristics and reliability of Al_2O_3 thin film humidity sensor", *Analytical Chemistry Symposia Series; Chemical Sensors*, vol. 17, Kodansha, Tokyo/Elsevier, Amsterdam, 1983, pp. 410-415

[2.30] G.J. Rogers, L.C. Westcott, R.A. Davies, H.O. Ali, G.H. Swallo and E. Read, "Humidity sensitive MOS structure", *Analytical Chemistry Symposia Series; Chemical Sensors*, vol. 17, Kodansha, Tokyo/Elsevier, Amsterdam, 1983, pp. 428-432

[2.31] R.K. Nahar and V.K. Khanna, "Ionic doping and inversion of characteristics of thin film porous Al_2O_3 humidity sensor", *Sens. Actuators B*, vol. 46, 1998, pp. 35-41

[2.32] G.Q. Li, P.T. Lai, S.H. Zeng, M.Q. Huang, and Y.C. Cheng, "Photo-, thermal

and humidity sensitivity characteristics of Sr_{1-x} La_x TiO_3 film on SiO_2/Si substrate", *Sens. Actuators A* 63, 1997, pp. 223-226

[2.33] G.Q. Li, P.T. Lai, S.H. Zeng, M.Q. Huang and B.Y. Liu, "Effects of chemical composition on humidity sensitivity of Al/$BaTiO_3$/Si structure", *Appl. Phys. Lett.*, vol. 66, May 1995, pp. 2436-2438

[2.34] G.Q. Li, P.T. Lai, S.H. Zeng, M.Q. Huang and B. Li, "A new thin-film humidity and thermal micro-sensor with Al/$SrNb_x$ $Ti_{1-x}O_3$/SiO_2/Si structure", *Sens. Actuators A*, vol. 75, 1999, pp. 70-74

[2.35] P. Shuk and M. Greenblatt, "Solid electrolyte film humidity sensor", *Solid State Ionics*, vol. 113-115, 1998, pp. 229-233

[2.36] N. Miura, H. Mizuno and N. Yamazoe, "Humidity sensor using antimony phosphate operative at a medium temperature of 150 250 °C", *Jpn. J. Appl. Phys.*, vol. 27, May 1988, pp. L931-L933

[2.37] B.M. Kulwicki, "Humidity sensors", *J. Am. Ceram. Soc.*, vol . 74, 1991, pp. 697-708

[2.38] D.E. Nelson and E.J. Amdur, "A relative humidity sensor based on the capacitance variations of a plastics film condenser", *Humidity and Moisture: Measurement and control in science and industry*, vol. 1, 1963, pp. 597-601

[2.39] M.J. Yang, Y. Li, N. Camaioni, G. Casalbore-Miceli, A. Martelli and G. Ridolfi, "Polymer electrolytes as humidity sensors: progress in improving an impedance device", *Sens. Actuators*, B vol. 86, 2002, pp. 229-234

[2.40] M. Hijikigawa, S. Miyoshi, T. Sugihara and A. Jinda, "A thin-film resistance humidity sensor", *Sens. Actuators*, vol. 4, 1983, pp. 307-315

[2.41] Y. Sakai, Y. Sadaoka and K. Ikeuchi, "Humidity sensors composed of graft copolymers", *Digest of technical papers, 1985 Int. Conf. on Solid-State Sensors and Actuators (Transducers '85),* Philadelphia, PA, U.S.A., 11-14 June 1985, pp. 213- 216

[2.43] S. Tsuchitani, T. Sugawara, N. Kinjo and S. Ohara, "Humidity sensor using ionic copolymer", *Digest of technical papers, 1985 Int. Conf. on Solid-State Sensors and Actuators (Transducers '85)*, Philadelphia, PA, U.S.A., 11-14 June 1985, pp. 210-212

[2.44] J. W. Gardner, V.K. Varadan, and O.O. Awadelkarim, *Microsensorsr, MEMS, and smart devices*, Chichester: John Wiley & Sons, 2001

[2.45] H. Wohltjen, "Mechanism of operation and design considerations for surface acoustic wave device vapour sensors", *Sens. Actuators*, vol. 5, 1984, pp. 307-325

[2.46] P.J. Schubert, and J.H. Nevine, "A polyimide-based capacitive humidity sensor", *IEEE Trans. on Electron Devices*, vol. ED-32, no. 7, pp. 1220-1223, July 1985

[2.47] M.C. Glenn and J.A. Schuetz, "An IC compatible polymer humidity sensor", *IEEE 3rd Int. Conf. on solid-state sensors and actuators (Transducers '85)*, Philadelphia, PA, U.S.A., 11-14 June 1985, pp. 217-220

[2.48] D.D. Denton, C.N. Ho, and S-G. He, "A solid-state relative humidity measurement system", *IEEE Trans. on Instrumentation and Measurement*, vol.

39, no. 3, June 1990, pp. 508-511

[2.49] H. Shibata, M. Ito, M. Asakura, and K. Watanabe, "A digital hygrometer using a polyimide film relative humidity sensor", *IEEE Trans. on Instrumentation and Measurement*, vol. 45, no. 2, pp. 564-568, April 1996

[2.50] U. Kang and K.D. Wise, "A high-speed capacitive humidity sensor with on-chip thermal reset", *IEEE Trans. Electron Devices*, vol. 47, no. 4, Apr. 2000, pp. 702-710

[2.51] M. Dokmeci, and K. Najafi, "A high-sensitivity polyimide capacitive relative humidity sensor for monitoring anodically bonded hermetic micropackages", *IEEE Journal of Microelectromechanical Systems*, vol. 10, no. 2, June 2001, pp. 197-204

[2.52] K. Sager, G. Gerlach, and A. Schroth, "A humidity sensor of a new type", *Sens. Actuators B*, vol. 18-19, 1994, pp. 85-88

[2.53] T. Boltshauser, L. Chandran, H. Balters, F. Bose and D. Steiner, "Humidity sensing properties and electrical permittivity of new photosensitive polyimides", *Sens. Actuators B*, vol. 5, 1991, pp. 161-164

[2.54] A.R.K. Ralston, J.A. Tobin, S.S. Bajikar, and D.D. Denton, "Comparative performance of linear, cross-linked, and plasma-deposited PMMA capacitive humidity sensors", *Sens. Actuators. B*, vol. 22, pp. 139-147, 1994

[2.55] M. Matsuguchi, Y. Sadaoka, Y. Sakai, T. Kuroiwa, and A. Ito, "A capacitive-type humidity sensor using cross-linked poly(methyl methacrylate) thin films", *J. Electrochem. Soc.*, vol. 138, no. 6, pp. 1862- 1865, June 1991

[2.56] K. Suzuki, Y. Nabeta and T. Inuzuka, "Mechanism of moisture sensing in organic polymer", *Tech. digest of 10th sensor symposium*, May 30-31, 1991, Tokyo, Japan, pp. 61-64

[2.57] J.M. Pérez, and C. Freyre, "A Poly(ethyleneterephthalate)-based humidity sensor", *Sens. Actuators B*, vol. 42, pp. 27-30, 1997

[2.58] T. Kuroiwa, T. Miyagishi, A. Ito, M. Matsuguchi, Y. Sadaoka, and Y. Sakai, "A thin-film polysulfone-based capacitive-type relative-humidity sensor", *Sens. Actuators B*, vol. 24-25, pp. 692-695, 1995

[2.59] P. Thoma, J.O. Colla and R. Stewart, "A capacitance humidity-sensing transducer", *IEEE Trans. on Components, Hybr. and Manufact. Technol.*, vol. CHMT-2, no. 3, Sept. 1979, pp. 321-323

[2.60] H. Grange, C. Bieth, H. Boucher, and G. Delapierre, "A capacitive humidity sensor with very fast response time and very low hysteresis", *Sens. Actuators*, vol. 12, pp.291-296, 1987

[2.61] Y. Sadaoka, M. Matsuguchi, Y. Sakai and K. Takahashi, "Effects of sorbed water on the dielectric constant of some cellulose thin films", *J. of Materials Science Lett.*, 7, 1988, pp. 121-124

[2.62] C. Caliendo, E. Verona, A. D'Amico, A. Furlani, G. Iucci, and M.V. Russo, "A new surface acoustic wave humidity sensor based on a polyethynylfluorenol membrane ", *Sens. Actuators B*, vol. 18-19, 1994, pp. 82-84

[2.63] A. Bearzotti, A. D'Amico, A. Furlani, G. Iucci, and M.V. Russo, "Fast

humidity response of a metal halide-doped novel polymer", *Sens. Actuators B*, vol. 7, pp. 451-453, 1992

[2.64] Z.M. Rittersma, A. Splinter, A. Bödecker, and W. Benecke, "A novel surface-micromachined capacitive porous silicon humidity sensor", *Sens. Actuators B*, vol. 68, 2000, pp. 210-217

[2.65] S. Kim, J. Park, S. Lee and S. Yi, "Humidity sensors using porous silicon layer with mesa structure", *J. Phys. D: Appl. Phys.*, vol. 33, pp. 1781-1784, 2000

[2.66] R.C. Anderson, R.S. Muller and C.W. Tobias, "Investigation of porous silicon for vapor sensing", *Sens. Actuators A*, vol. 21-23, pp. 835-839, 1990

[2.67] G.M. O'Halloran, P.M. Sarro, J. Groeneweg, P.J. Trimp, and P.J. French, "A bulk micromachined humidity sensor based on porous silicon", *Proc. IEEE Solid state sensors and Actuators 1997, Transducers '97*, Chicago, June 16-19 1997, pp. 563-566

[2.68] W.Lang, P. Steiner, and H. Sandmaier, "Porous silicon: a novel material for microsystems", *Sens. Actuators A*, vol. 51, 1995, pp. 31-36

[2.69] R. Heriono, G. Bomchil, K. Barla, and C. Bertrand, "Porosity and pore size distributions of porous silicon layers", *J. Electrochem., Soc.,* vol. 134, 1995, pp. 1994-2000

Chapter 3. Polyimide-based capacitive humidity sensors

3.1. Introduction

The aim of this chapter is to report on the characteristics of humidity sensors for environmental monitoring which are cost effective and use conventional IC process technology as closely as possible. Polyimide was selected as a humidity sensing material throughout this chapter because of its inherent IC process compatibility, negligible temperature dependence and good resistance against contamination.

The significant advances reported in this chapter include investigations into sensitivity improvement of the plasma treated polyimide-base humidity sensor and a new sensor structure which gives improved sensitivity over more conventional structures. It is known that plasma treated polyimide becomes more reactive towards moisture [3.1][3.2]. An analysis of the modification of polyimide chemistry and the effects on the responses of humidity sensors are presented. The new structure which consists of a top electrode – a perforated polyimide layer – a lower polyimide layer – and a bottom electrode brings approximately twice the sensitivity compared to that of a standard structure (top electrode - polyimide layer - bottom electrode) with few additional process steps.

The chapter starts with a sensitivity study of various electrode structures using the same polyimide and processes, and includes the effects of polyimide curing temperature, long-term stability, diffusion constant, sensor support electronic circuitry, study of plasma treated polyimide and a response study of the new structure. All humidity sensors presented in the thesis were tested twice in an environmental chamber shown in Fig. 3.1. The dimension of the environmental chamber is 45 cm high, 40 cm wide and 38 cm deep. It contains off-the-shelf sensors; an IC temperature sensor (LM35DZ, National Semiconductor) for data logging, a platinum thermometer for a PID controller and a humidity sensor (Elektronik, series EE06) as references. The IC

Chapter 3. Polyimide-based capacitive humidity sensors

3.1. Introduction

The aim of this chapter is to report on the characteristics of humidity sensors for environmental monitoring which are cost effective and use conventional IC process technology as closely as possible. Polyimide was selected as a humidity sensing material throughout this chapter because of its inherent IC process compatibility, negligible temperature dependence and good resistance against contamination.

The significant advances reported in this chapter include investigations into sensitivity improvement of the plasma treated polyimide-base humidity sensor and a new sensor structure which gives improved sensitivity over more conventional structures. It is known that plasma treated polyimide becomes more reactive towards moisture [3.1][3.2]. An analysis of the modification of polyimide chemistry and the effects on the responses of humidity sensors are presented. The new structure which consists of a top electrode – a perforated polyimide layer – a lower polyimide layer – and a bottom electrode brings approximately twice the sensitivity compared to that of a standard structure (top electrode - polyimide layer - bottom electrode) with few additional process steps.

The chapter starts with a sensitivity study of various electrode structures using the same polyimide and processes, and includes the effects of polyimide curing temperature, long-term stability, diffusion constant, sensor support electronic circuitry, study of plasma treated polyimide and a response study of the new structure. All humidity sensors presented in the thesis were tested twice in an environmental chamber shown in Fig. 3.1. The dimension of the environmental chamber is 45 cm high, 40 cm wide and 38 cm deep. It contains off-the-shelf sensors; an IC temperature sensor (LM35DZ, National Semiconductor) for data logging, a platinum thermometer for a PID controller and a humidity sensor (Elektronik, series EE06) as references. The IC

temperature sensor operates between 0 °C and 100 °C with ±1.5 °C accuracy. The humidity sensor operates between 0 and 100% RH with ±3.0% RH accuracy. Its operation temperature range is from –40 °C to +60 °C. This humidity sensor was counterchecked against a humidity sensor (Honeywell, HIH-3602-L) at ramping up/down rate of 1% RH/min between 15 and 90% RH and found to be appropriate to use.

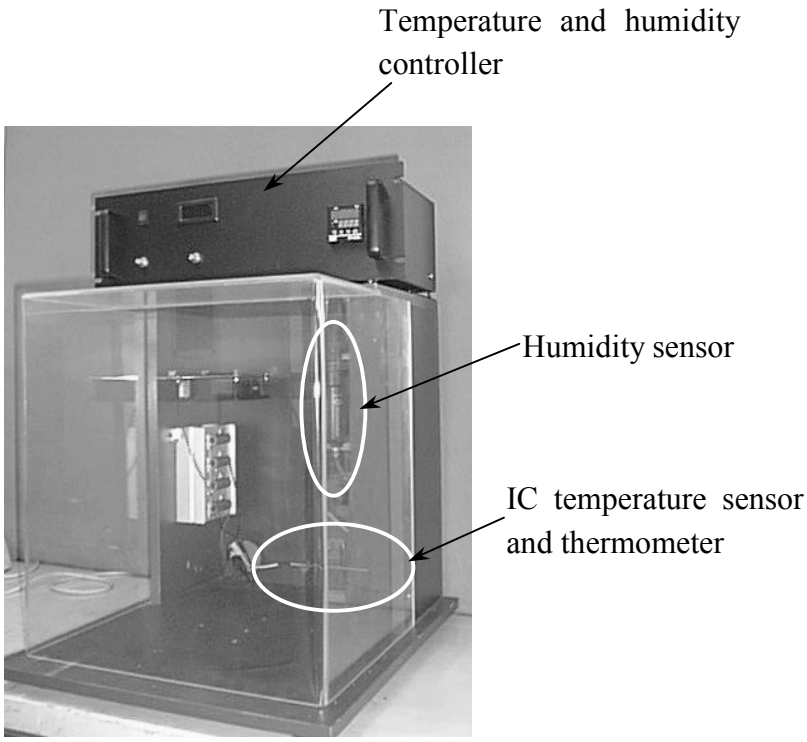

Fig. 3. 1. The custom built environmental chamber.

3.2. Electrodes

Various electrode structures have been reported in the literature including an interdigitated [2.19][2.39][2.41][2.45][3.4], parallel-plate with slot in top electrode [2.49], parallel-plate with grid top electrode [2.65], porous electrode [2.56][3.3]. Lack of information on topics such as the consistency of brand of polyimide and process methods, and numerous different types of polyimide on the market make much of this work difficult to reproduce. The purpose of the investigation here is to examine the effect on humidity sensitivity of various electrode structures while keeping the same polyimide and process methods. The polyimide used in this experiment is UR-5440 from Toray Industries Inc, which is a negative-tone photodefinable type. The electrodes investigated are interdigitated (IDT), parallel-plate with slot on top electrode (SLOT), parallel-plate with grid top electrode (GRID), porous electrode (PR), and porous with grid top electrode (PR+GRID). The IDT consists of 15 pair fingers. Some of figures of the electrodes are shown in Fig.3.2. An outline of the fabrication procedures is given in Table 3.1. The sensor with IDT requires only process steps 1 to 3 in Table 3.1. Gold was used only for the top electrode with a porous structure (PR).

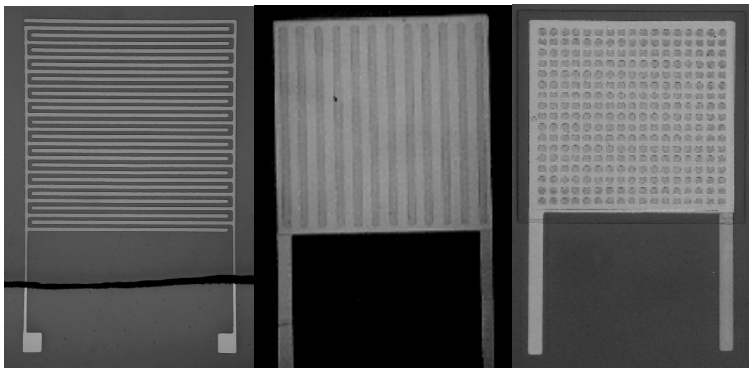

(a) (b) (c)

Fig. 3. 2. Images of fabricated humidity sensors. (a) IDT, (b) Slit, (c) Grid electrodes

Table 3. 1. Outline of humidity sensor fabrication steps

	Process names	Process conditions
1	Bottom electrode	Deposition of nickel and photolithographic patterning.
2	Polyimide layer	Spin-coat polyimide. Soft-cure at 80 °C and 100 °C for 3 min at each temperature. Photolithographic patterning.
3	Cure polyimide layer	Cure at 140 °C for 30 min followed by 350 °C for 1 h in nitrogen. And cooling to room temperature. The ramp rate between these two temperatures are 20 °C /min.
4	Top electrode	Deposition of nickel or gold followed by photolithographic patterning.

In this examination, the fabricated sensors were tested in a computer controlled environmental chamber. The outputs were measured between 20% RH and 90% RH with a ramp rate of 1% RH/min. The capacitance was read with an LCR meter (GW LCR-815) at 1 kHz with a signal amplitude of 1 V_{rms} sinusoidal waves. There is a clear difference in results between the IDT and parallel-plate electrodes. The sensor with IDT is simpler to make, however, its sensitivity in low humidity ranges of up to 50 or 60% RH is extremely low. Almost no change in capacitance around these ranges can be seen in Fig. 3.3. In contrast, the sensitivity increases in a high humidity region. This effect is pronounced when the polyimide layer becomes thicker. The IDT has been used in resistive type humidity sensors quite extensively [2.19][2.39][2.41][2.45][3.14]. Humidity sensors constructed with ceramics or polymers which detect changes in resistance have larger sensitivity with IDT. The same response cannot be offered with dielectric materials as in the result presented here. The study conducted by [2.45] [3.4] with polyimide indicated behavior similar to the results presented here.

The results of the sensors with parallel-plate electrodes are shown in Fig.3.4 and Table 3.2. The sensitivities presented in Table 3.2 were calculated using the expression:

$$S = (1/C_{20\%\,RH})(\Delta C/\Delta RH) \qquad (3.2.1)$$

where $C_{20\%\,RH}$ is capacitance at 20% relative humidity, ΔC is change in capacitance over the measured humidity range, and ΔRH is measured range in relative humidity.

Unlike the IDT electrode, the sensors with parallel-plate electrodes have greater sensitivity in low humidity regions. The largest sensitivity is found with the GRID electrode. A porous electrode constructed with nickel and gold has different sensitivity. Although the thickness of both electrodes, 20 nm, is the same, the sensitivity with gold is much higher. This could be an indication of porosity difference formed in the electrodes. There is negligible difference between GRID and PR+GRID electrodes. This means that there is no significant advantage using the PR+GRID electrode structure with nickel.

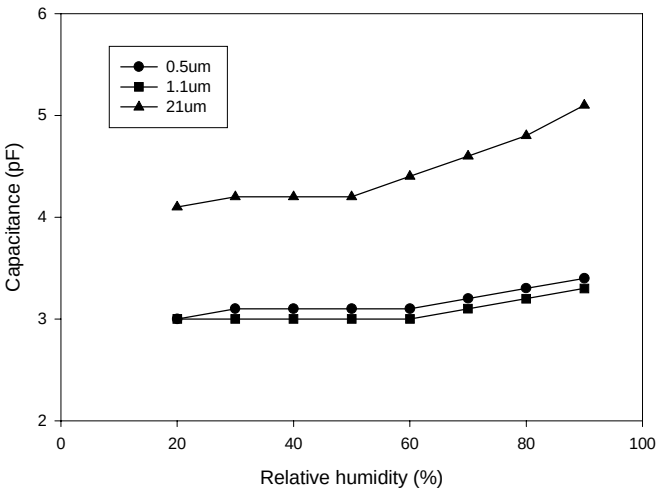

Fig. 3. 3. Sensor response with IDT electrode. Thickness of polyimide: 0.5 μm, 1.1 μm and 21 μm.

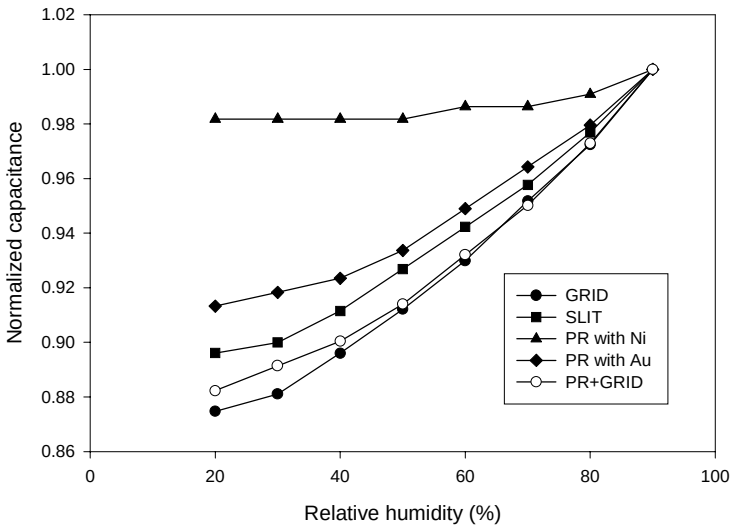

Fig. 3. 4. Sensor response with various top electrodes of parallel-plate humidity sensors; grid with nickel (GRID), slit with nickel (SLIT), porous with nickel (PR with Ni), porous with gold (PR with AU), and porous plus grid with nickel (PR+GRID). Humidity was varied at 1% RH/min.

Table 3. 2. Summary of minimum and maximum capacitance and sensitivity of five different parallel-plate electrodes.

Electrodes	Capacitance at 20% RH (pF)	Capacitance at 90% RH (pF)	Sensitivity (%)
GRID	152.3	174.1	20.4
PR+GRID	195.0	221.0	19.0
SLIT	233.0	260.0	16.6
PR-Au	179.0	196.0	13.6
PR-Ni	216.0	220.0	2.6

Hysteresis was observed in all sensors due to the different rate in absorption and desorption of moisture because the sensor output in desorption became the same output in absorption after leaving the sensor at a particular relative humidity for a long time. The maximum and minimum of hysteresis were each found from absorption and desorption curve. The data in absorption was used as a reference. A sample graph

created using data obtained for parallel-plate grid electrode is shown in Fig. 3.5. The minimum and maximum hysteresis of each electrode case are compared and tabulated in Table 3.3. The PR-Ni electrode sensor is omitted because its hysteresis is very small as a result of small sensitivity. The maximum hysteresis is found in the PR-Au electrode. The electrodes with holes tend to indicate similar hysteresis. This means that the existence of holes helps moisture leave the polyimide film quicker than the porous electrode.

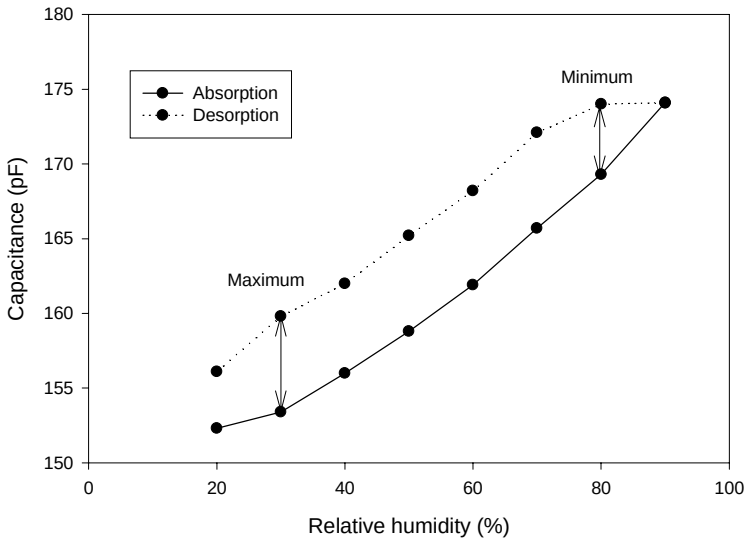

Fig. 3. 5. Absorption and desorption curves of the humidity sensor with a parallel-plate grid electrode, indicating maximum and minimum hysteresis locations.

Table 3. 3. Summary of minimum and maximum hysteresis of various electrodes

Electrodes	Minimum hysteresis (%)	Maximum hysteresis (%)	Minimum hysteresis (% RH)	Maximum hysteresis (% RH)
IDT (21 μm-thick)	0.0	4.8	0.0	10.0
GRID	2.7	4.1	12.3	20.6
PR+GRID	3.1	5.0	16.2	27.0
SLIT	2.4	4.6	15.4	28.2
PR-Au	2.1	7.2	16.0	54.2

3.3. Process temperature effect on sensitivity and temperature dependence

In this section, the effects on humidity sensitivity and sensor operating temperatures resulting from the different maximum curing temperatures of the polyimide are discussed. Four samples were prepared at maximum curing temperatures of 250, 300, 350 and 400 ^{o}C after photolithographycally patterning polyimide as the process number 3 in Table 3.1. The process temperature is known to exert influence on water uptake by weight [3.5]. It is clear that the largest sensitivity is observed at the lowest curing temperature as Fig. 3.5 and Table 3.4 show. No difference in sensitivity can be seen in the 350 ^{o}C and 400 ^{o}C samples. Stability at different operating temperatures is also an important aspect in environmental monitoring. The capacitance was recorded from 20 ^{o}C to 50 ^{o}C by 10 ^{o}C increments at selected relative humidity, 20%, 50% and 90%. The relevant results are presented in Table 3.4. The change in capacitance is calculated by referring to the difference from the value at room temperature, 20 ^{o}C. Graphical results are shown in Figs. 3.7 through 3.10. Significant temperature dependence was found when the sensor was cured at 250 ^{o}C. Very little effect was seen in the 350 ^{o}C sample even at 90% RH.

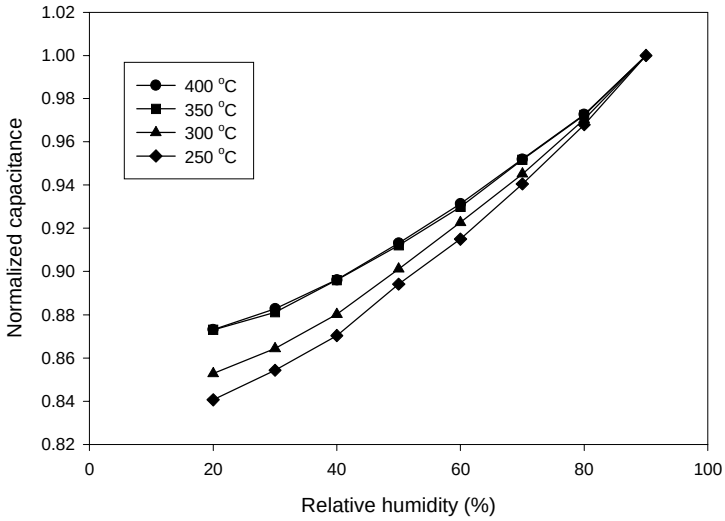

Fig. 3. 6. Comparison of change in sensor capacitance when humidity was increased. Each curve corresponds to the sensors with polyimide cured at 250, 300, 350 and 400 °C.

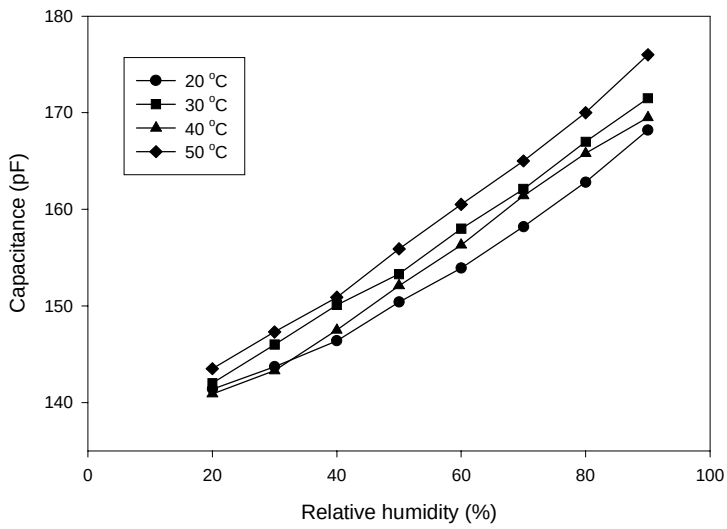

Fig. 3. 7. Temperature dependence of humidity sensor with polyimide cured at 250 °C

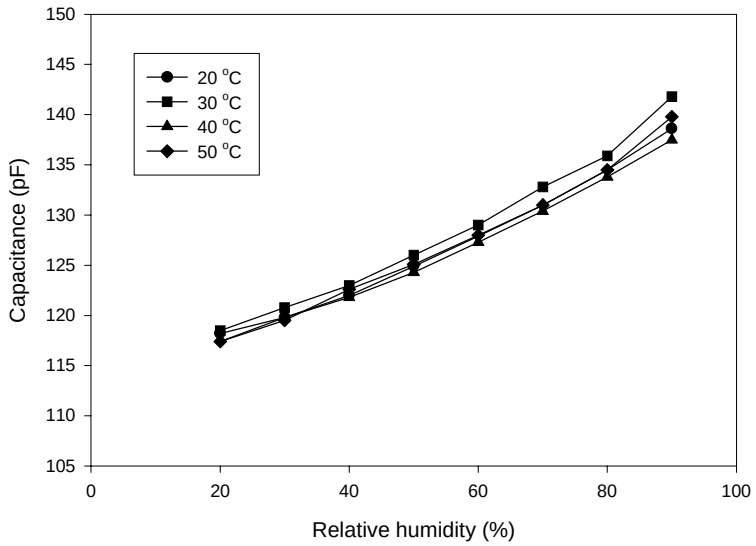

Fig. 3. 8. Temperature dependence of humidity sensor with polyimide cured at 300 °C

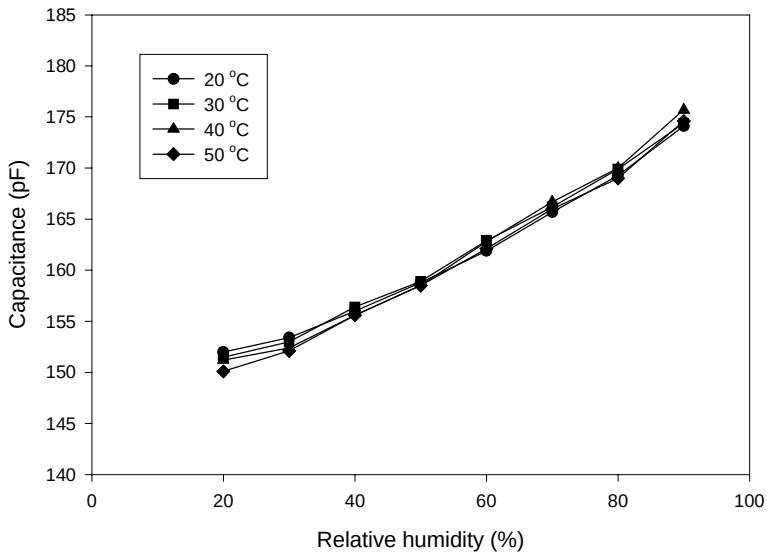

Fig. 3. 9. Temperature dependence of humidity sensor with polyimide cured at 350 °C

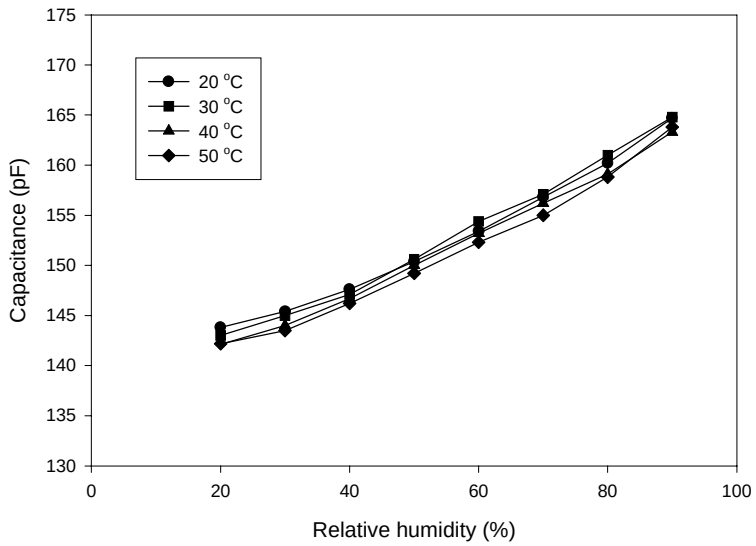

Fig. 3. 10. Temperature dependence of humidity sensor with polyimide cured at 400 °C

Table 3. 4. Summary of sensitivity and capacitance change due to temperature dependence

Cure temperature	Sensitivity (%)	ΔC @ 20% RH (%)	ΔC @ 50% RH (%)	ΔC @ 90% RH (%)
250 °C	27.1	1.49	3.66	4.64
300 °C	24.7	0.68	0.16	8.66
350 °C	20.8	1.25	0.19	0.29
400 °C	20.8	1.11	0.80	0.55

A short-term drift test was conducted at three different relative humidity levels: 20, 50 and 90% RH for ten hours. The sensor output was recorded every hour after the sensors were settled in each relative humidity for three hours. The graphs in Fig. 3.11 show the variation in output compared to the value recorded at the beginning of measurement. Note that the y-axis scale is different in the three cases. In a dry condition, very little error was observed in all sensors. Overall the sensor cured at 350 °C was very steady while the one cured at 250 °C showed the largest drift. The results obtained from

the sensor with the polyimide cured at 250 ^{o}C showed the largest sensitivity, largest temperature dependence and most unstable behavior. This may be due to the difference in degree of polyimide imidization [3.6]. At 250 ^{o}C, aromatic rings in polyimide may not be fully closed. In addition, it is possible that solvent remaining in the polyimide layer causes this instability.

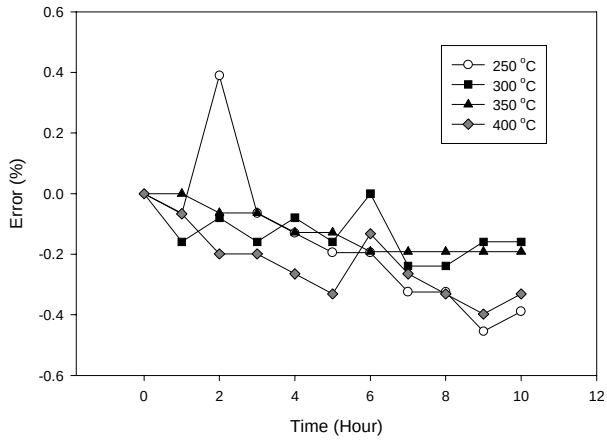

(a)

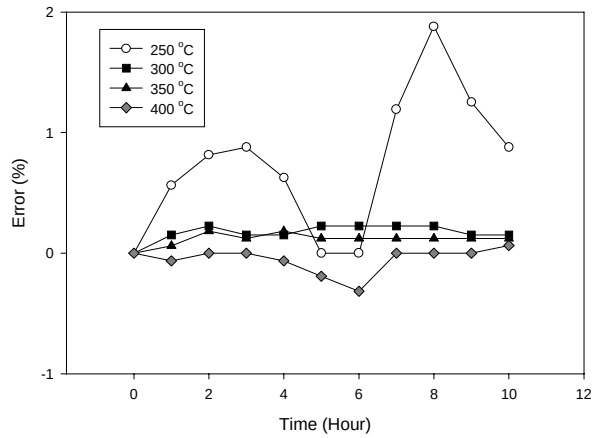

(b)

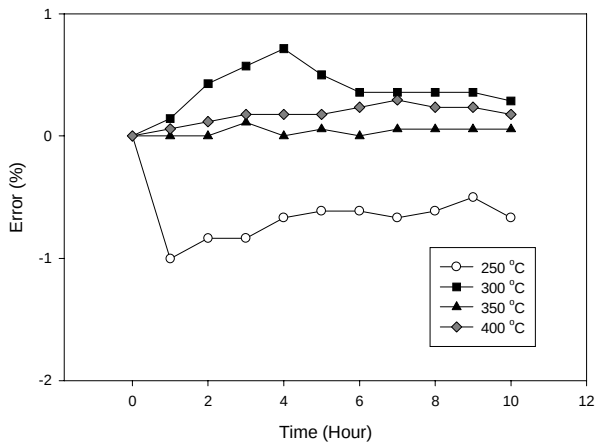

(c)

Fig. 3. 11. Short-term drift test of humidity sensors with four different polyimide curing temperatures: 250 ^{o}C, 300 ^{o}C, 350 ^{o}C and 400 ^{o}C (a) at 20% RH, (b) at 50% RH, (c) at 90% RH

3.4. Long-term stability

The long-term stability of the sensor cured at 350 ^{o}C was examined for 321 days. The sensor was left exposed in an office environment during this test period. A small drift observed from time to time is shown in Fig. 3.12. The maximum drift in terms of absolute humidity was found to be within 2%. This corresponds to 7.5% RH change but this is due to inconsistent behavior of the environmental chamber during the long period of time. Further work has to be done to monitor the long-term stability.

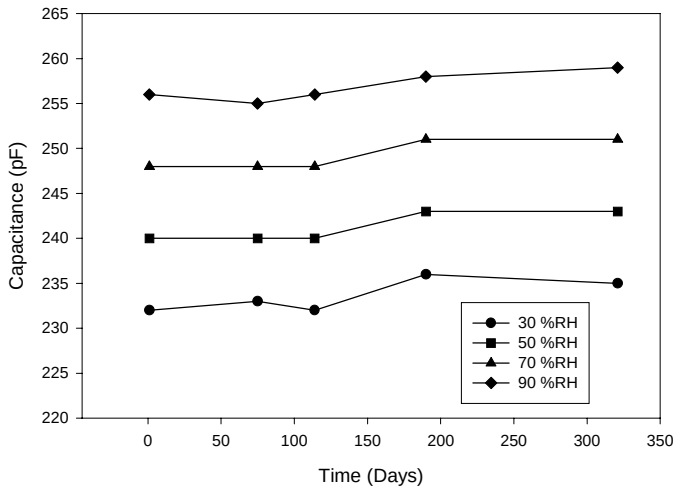

Fig. 3. 12. Long-term stability test of a polyimide-based capacitive humidity sensor for 321 days

3.5. Sensor support electronic circuitry

In this section, a method of data acquisition for a capacitive humidity sensor is presented. The output of the sensor is a DC voltage monotonically linked to the humidity sensor. The circuit built operates in pulse width modulation (PWM) mode, which is one of the functions of timer IC 555. The function block diagram is shown in Fig. 3.13. This sensor support electronic circuitry uses two timers. One timer continuously issues a pulse train in order to trigger the other timer, which operates in PWM mode. The circuit schematic diagram and the image of the constructed circuit are

given in Fig. 3.14 and Fig. 3.15, respectively.

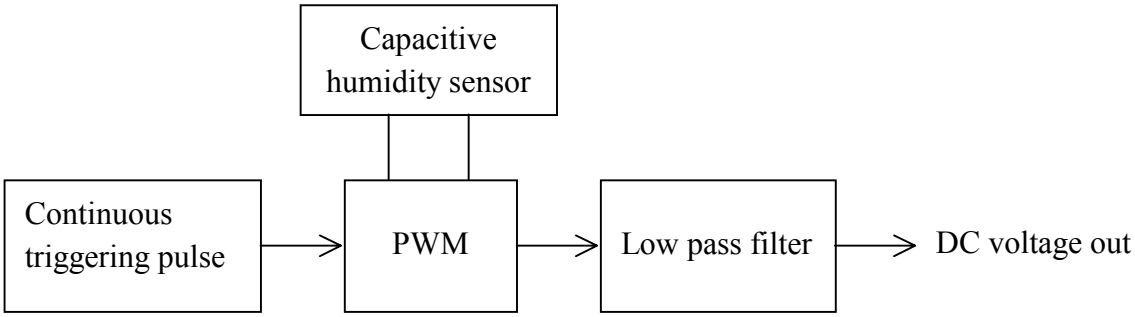

Fig. 3. 13. Block diagram of sensor output circuitry

An astable oscillator issues a pulse train at a rate of 50 kHz. The width of output pulse increases as capacitance increases, which is equivalent to an increase in humidity. The values used for the components in the circuit are as follows: R1=R3=56 kΩ, R2=39 kΩ, R4=10 kΩ, C1=180 pF, C2=0.01 μF and C3=1 μF. Capacitor C2 was inserted to avoid a dc component on the humidity sensor surface.

Measurements were carried out with this circuit configuration from 20% RH to 90% RH at a ramp-up rate of 1% RH/min. The result in Fig. 3.16 shows a quasi-linear response. A dc output voltage varied approximately 3.7 mV/% RH below 50% RH and approximately 6.0mV/% RH above 50% RH. Alternatively, PWM output can be directly fed to a microprocessor for data logging.

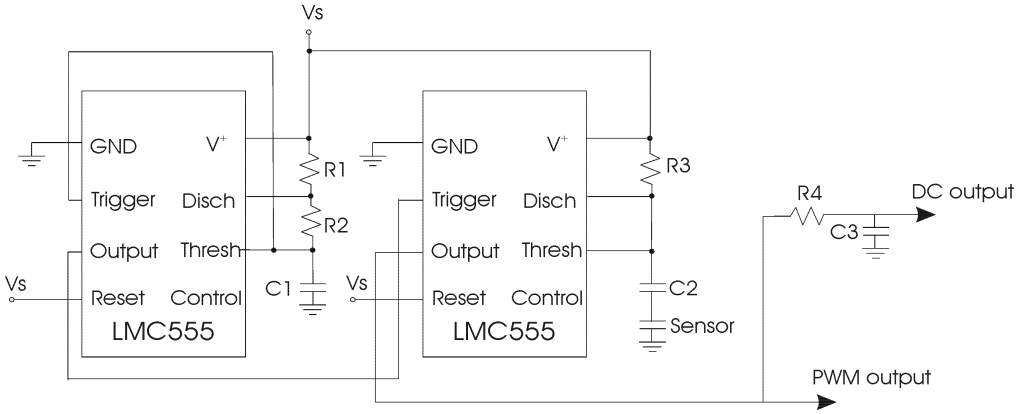

Fig. 3. 14. Schematic of electronic circuitry for humidity sensor

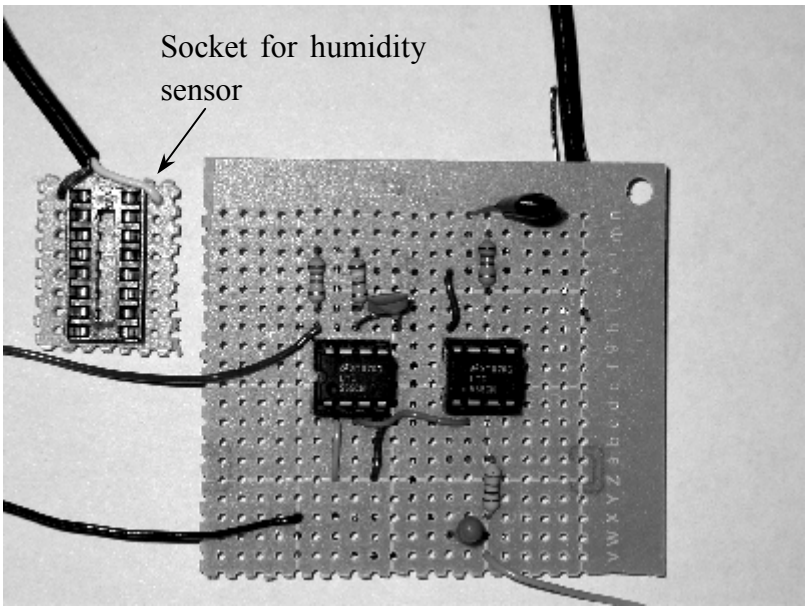

Fig. 3. 15. Constructed circuit based on the circuit diagram in Fig. 3.14.

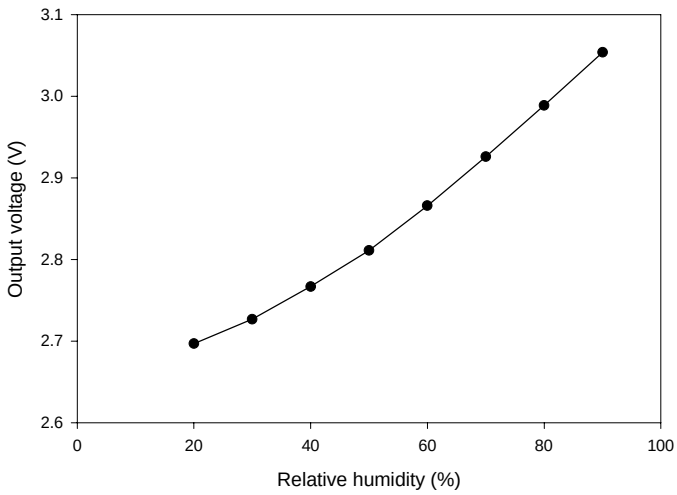

Fig. 3. 16. DC output voltage from sensor support electronic circuitry

3.6. Diffusion coefficient

The diffusion of moisture into polymer films has been studied for various applications such as interlay dielectrics, protective coatings for integrated circuits [3.6] and packaging integrated circuits [3.7]. The dry-to-wet transient analysis of moisture diffusion kinetics is based on Fick's second law, which is defined as:

$$\frac{\partial C}{\partial t} = D\frac{\partial^2 C}{\partial x^2} \tag{3.6.1}$$

where

C : water concentration in the film

D : Diffusion coefficient

Eqn. (3.6.1) is applicable for the case with a one dimensional diffusion model and a constant diffusion coefficient D. The diffusion coefficient can be derived from fitting the numerical model to experimental data. The numerical model for the structure in Fig. 3.17 is given by [3.8]

$$\frac{M_t}{M_\infty} = 1 - \sum_{n=0}^{\infty} \frac{8}{(2n+1)^2 \pi^2} exp\left(\frac{-D(2n+1)^2 \pi^2 t}{l^2} \right) \tag{3.6.2}$$

where

M_t : total mass of moisture entered the film

M_∞ : mass of moisture entered the film after infinite time

D: diffusion coefficient

l : width/thickness of the film in the same direction of diffusion taking place

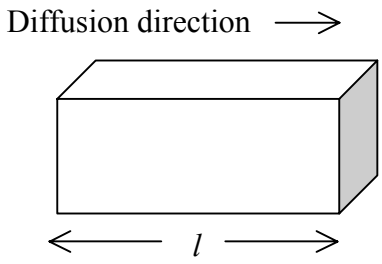

Fig. 3. 17. Geometry of plane sheet

Experiments are usually performed by measuring the weight of the film as a function of time. However, the resolution of weight is in the order of micro grams, which would require a major upgrade of the current laboratory equipment available. Instead of measuring weight of the film, the diffusion measurement was conducted by recording voltages from the support electronic circuit. Since capacitance is proportional to output voltage, the left hand side in Eqn. (3.6.2) can be cast into the form of normalized output voltage as:

$$V_{norm} = \frac{V_t - V_{dry}}{V_{wet} - V_{dry}} = \frac{M_t}{M_\infty} \tag{3.6.3}$$

where

V_t : output voltage at time t

V_{dry}: equivalent output voltage in the dry environment (<10% RH)

V_{wet}: equivalent output voltage in the wet environment (90% RH)

The sensor used in this experiment was the grid electrode type shown in Fig.3.2 (c). Since the diffusion takes place from two sides, the half of the film width l is used hence Eqn. (3.6.4).

$$V_{norm} = 1 - \sum_{n=0}^{\infty} \frac{8}{(2n+1)^2 \pi^2} exp\left(\frac{-D(2n+1)^2 \pi^2 t}{0.25 l^2} \right) \quad (3.6.4)$$

The diffusion test was conducted as follows:

- Each humidity sensor was placed in a tightly closed container with silica gel for 2 days.
- The lid of the container was opened inside the environmental chamber whose atmosphere was settled at 90% RH.

The diffusion coefficients for four cases are presented in Table 3.5. The fastest transient response after curve fitting performed with Eqn. (3.6.4) is given in Fig. 3.18. The dotted line and the solid line represent experimental data and numerical model, respectively. The experimental data is somewhat noisy but it shows the trend of water uptake into the film. The results reveal that the fastest water diffusion took place in the film cured at 250 ^{o}C. The diffusion coefficient decreased as the curing temperature increased. This is consistent with the variation in sensitivity reported earlier in this chapter.

Table 3. 5. Diffusion coefficients of polyimide cured at four different temperatures

Cure temperature	250 ^{o}C	300 ^{o}C	350 ^{o}C	400 ^{o}C
Diffusion coefficient ($\mu m^2/s$)	0.75	0.59	0.57	0.45

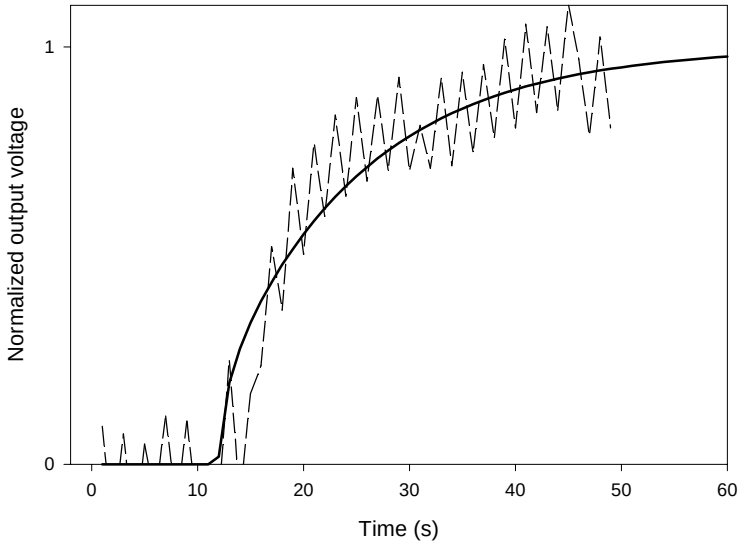

Fig. 3. 18. Response curve of humidity sensor with polyimide layer cured at maximum temperature of 250 ^{o}C when the sensor was exposed to 90% RH from dry condition created with silica gel. Dotted line = experimental data, Solid line = Numerical data

3.7. Chemical modification of polyimide film by O_2 plasma etching

The degree of change of PMDA-ODA type polyimide in terms of weight uptake and relative permittivity as a result of water absorption has been previously reported [3.1][3.5]. This type of polyimide absorbs moisture between 2.5% and 4% of its own weight at high relative humidity [3.1]. The relative permittivity, ε_r, changes approximately between 3.3 and 3.9 when the polyimide was cured at 350 ^{o}C [3.5]. Low water uptake and low relative permittivity are useful for intermetal dielectrics used in packaging and as a buffer layer of integrated circuits. From a humidity sensor point of view, contrary characterstics are desired, that is, large water uptake and large relative permittivity. This leads to high sensitivity, resulting in better signal-to-noise ratio at the output. It has been reported that plasma-treated polyimide increases the sensitivity and the response speed, however, the type of gas used in the process was not stated [3.2]. It

is known that polyimide etched with oxygen in a plasma becomes very reactive to moisture [3.1]. As plasma etching is a part of standard IC fabrication processes, it is beneficial to apply this technique in order to achieve good sensitivity and fast response time simultaneously.

The following subsections present the response of both non-plasma and plasma treated humidity sensors with a corresponding chemical analysis of polyimide in both types of humidity sensors. X-ray photoelectron spectroscopy (XPS) and the Fourier transform infrared (FTIR) were used to analyze the surface chemistry of polyimide. Atomic force microscopy (AFM) was used to study surface morphology of the polyimide. The surfaces of both the plasma treated and the non-plasma treated polyimide surfaces were scanned and the surface areas were calculated.

3.7.1. Experimental procedures of humidity sensors

The sensor in this investigation was a parallel-plate capacitive type with a perforated top electrode. The polyimide used in the humidity sensor was PI2737 from HD Microsystems. The size of the humidity sensing area was 1.8 mm × 1.8 mm. The fabrication followed the step in section 3.2 with the addition of plasma treatment after curing. The plasma etching was performed in a LAM 490 etcher for 20 s. RF power was set to 200 W at a frequency of 15.36 MHz with O_2 at a flow rate of 100 sccm in 200 mTorr. Afterwards, aluminium was evaporated and wet-etched for patterning a top electrode. The Al – polyimide – Al humidity sensor had holes of 80 μm in diameter in the top electrode to accelerate moisture uptake into polyimide. The sensor was mounted and bonded onto a ceramic IC package. The final thickness of polyimide layer was measured to be 0.55 μm for non-plasma treated and 0.4 μm for plasma treated.

3.7.2. Experimental results

A. Response of humidity sensors

The capacitance of the sensors was measured in the environmental chamber. The

relative humidity was varied from 30% to 90% at 25 °C, increased and decreased at a rate of 2% RH/min this time. The capacitance was measured using a LCR meter at 1 kHz with an amplitude of 1 V_{rms} sinusoidal waves. The outputs of the non-plasma and the plasma treated sensors varied from 201 to 207 pF and from 221 to 244 pF, respectively. The normalized outputs can be seen in Fig. 3.19 and the response is linear in both cases. The sensitivity of the non-plasma treated and plasma treated sensor is 4.9% and 17.3%, respectively. Another difference in the humidity sensors was hysteresis. The non-plasma treated sensor had a larger hysteresis as shown in Fig. 3.20. This implies that it takes the non-plasma treated humidity sensor a longer time to release moisture in polyimide. Higher sensitivity to moisture was observed in the plasma-treated humidity sensor. This was true in both the absorbing and desorbing humidity cases.

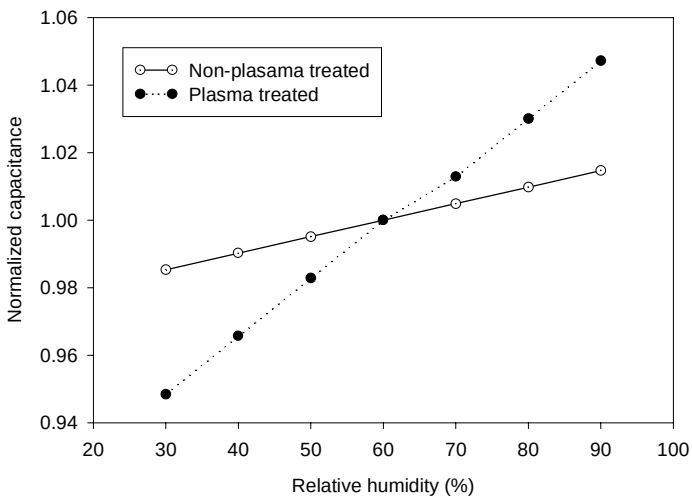

Fig. 3. 19. Measured outputs of non-plasma and plasma treated humidity sensors as a function of relative humidity.

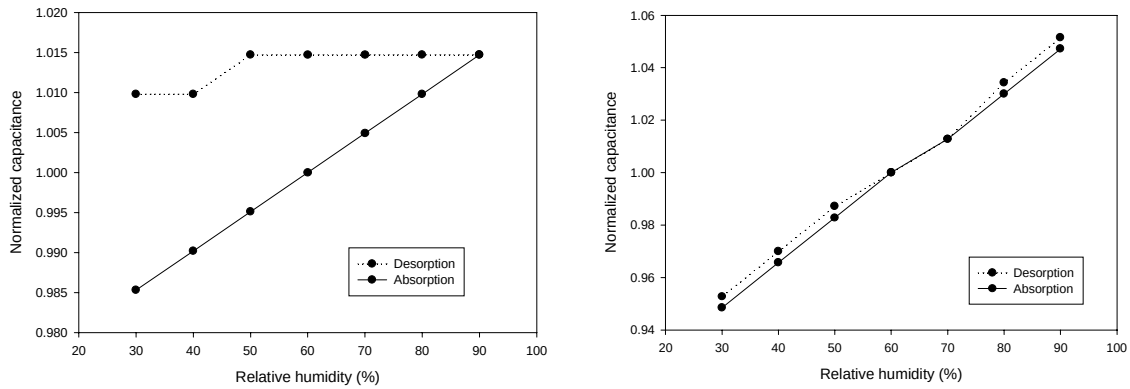

(a) (b)

Fig. 3. 20. Hysteresis of humidity sensor, (a) Non-plasma treated (b) Plasma treated

The sensor response speed was determined using the following method:

- The sensors were both placed inside a sealed tank at room temperature.
- The tank was filled with dry nitrogen until the sensor outputs became stable.
- Outputs of the sensors were recorded simultaneously.
- Steam was introduced into the tank for 60s.

As shown in Fig. 3.21, the plasma treated humidity sensor responded quicker and had a shorter rising edge. A clear comparison can be made: the plasma treated sensor had 7s rising edge between 40 and 47s, while the non-plasma treated sensor had 13s rising edge between 46 and 59s. The difference in maximum output values between two sensors was due to the difference in sensitivity. The response speed was estimated using the time to achieve 50% full-scale deflection because the plasma treated sensor has larger sensitivity and a larger maximum output. It took the plasma treated and the non-plasma treated sensors 3.5s and 6.5s to reach the level, respectively. The plasma-treated sensor responded about 1.9 times faster than the non-plasma treated one.

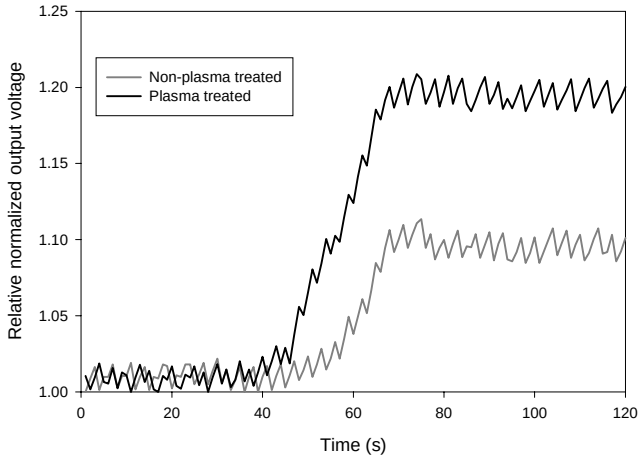

Fig. 3. 21. Response speed of the non-plasma and plasma treated humidity sensors to a burst of steam.

B. Chemical analysis in XPS

XPS was used to investigate the chemical composition of the polyimide surfaces. The data was obtained by PHI Model 560 with a nonmonochromatic Mg Kα source, 1253.6 eV. XPS survey scans were taken at a pass energy of 100 eV and multiplex scans were taken at 25 eV.

The survey scan was performed to identify the chemical composition of the surfaces. C1s, O1s, and N1s emission were found in Fig. 3.22. It can be seen that the intensity of O1s increased while C1s decreased after plasma etching. The high resolution XPS spectra for C1s, O1s and N1s are shown in Fig. 3.23. Each type of bond was identified by curve fitting based on a Gaussian function with an aid of software. The reference of binding energies was C1s peak position at 285.0 eV. Peak shifts caused by sample charging in obtained data were within 0.5 eV. The C-C peak in the C1s data at 284.7 eV is attributed to the carbon atoms of aromatic rings, which are not bonded to either O or N. The peak at 285.7 eV is attributed to the carbon atoms of aromatic rings forming single bond to O or N. The peak for carbonyl carbon, C=O,

arises at 288.5 eV. The peak at 291.1 eV is thought to be π-π* shift.

There are two peaks found in O1s. The peaks at 531.9 eV and 533.7 eV stem from carbonyl oxygen C=O and single-bonded oxygen C-O. The N1s peak is found at 401.1 eV, which is imide nitrogen. The results after plasma treatment can be seen in Fig. 3.24 where the C=O component exhibits a relative increase. In the oxygen functional group, the peak at C-O increased. Table 3.6 lists the atomic concentration in polyimide surfaces. Si is detected in the plasma treated polyimide. This can be explained as the presence of the substrate on which polyimide was spun or silicon debris inside chamber of plasma etcher. O/C ratio increased from 0.39 in non-plasma treated to 0.66 in O_2 plasma treated case. This result implies that oxidation of the polyimide surface took place during etching.

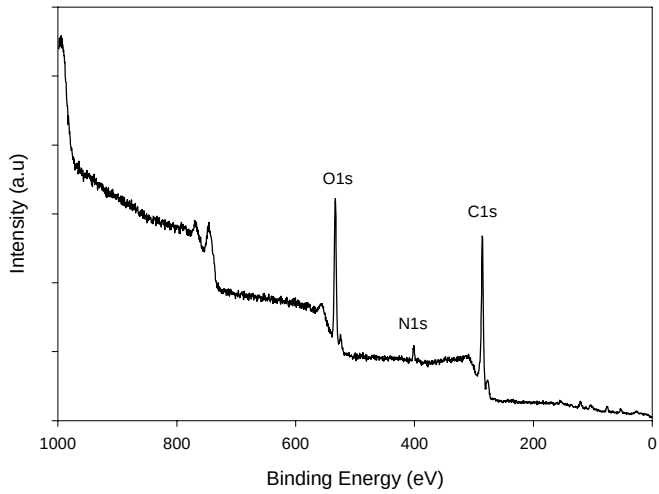

(a)

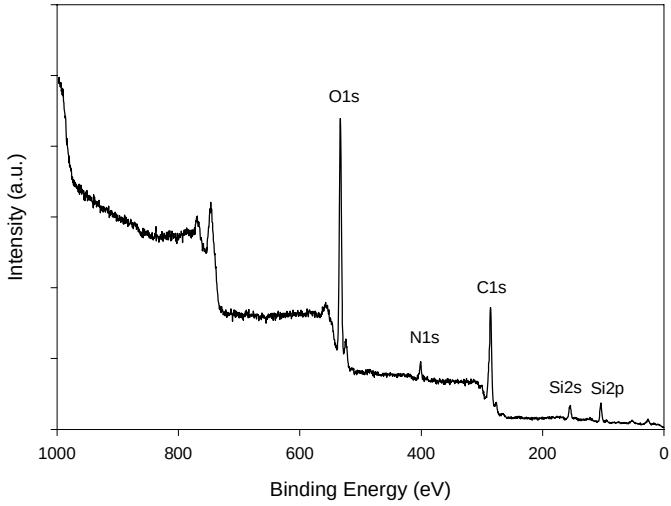

(b)

Fig. 3. 22. XPS survey scan of PI2737; (a) Non-plasma treated, (b) Plasma treated

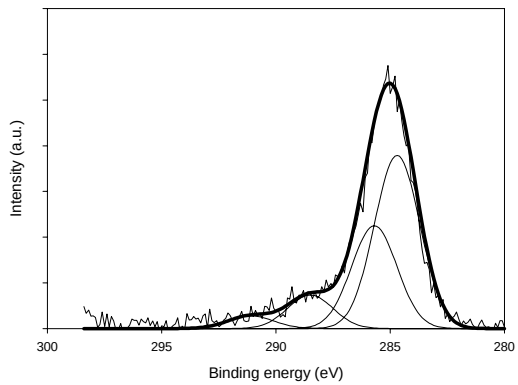

(a)

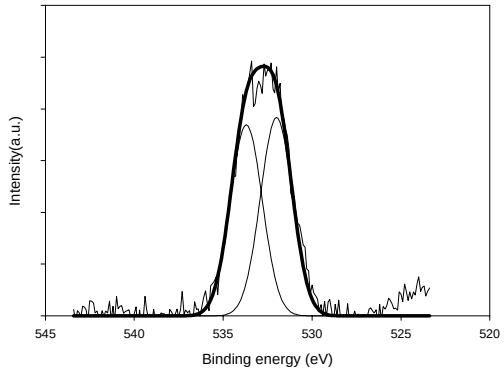

(b)

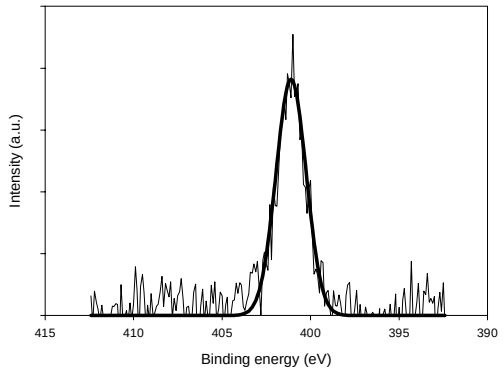

(c)

Fig. 3. 23. XPS spectra for non-plasma treated polyimide, (a) C1s (b) O1s (c) N1s.

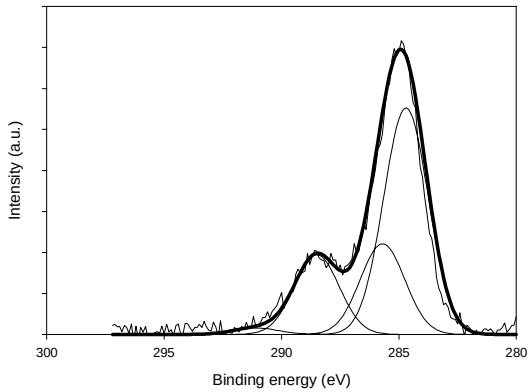

(a)

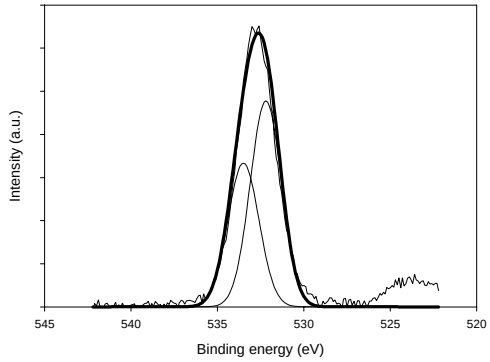

(b)

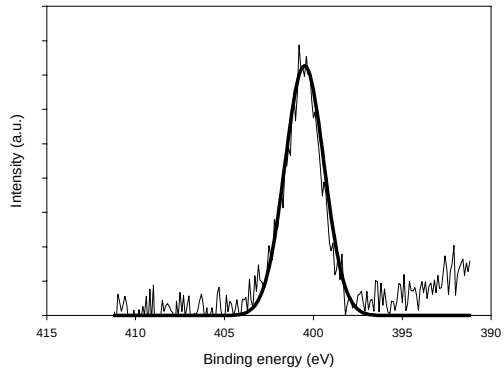

(c)

Fig. 3. 24. XPS spectra for plasma treated polyimide, (a) C1s (b) O1s (c) N1s

Table 3. 6. A summary of atomic concentration of polyimide

Element	Non-plasma treated	O_2 plasma treated
C1s	69.5 %	53.2 %
O1s	27.4 %	35.1 %
N1s	3.0 %	3.9 %
Si	0 %	7.7 %
O/C ratio	0.39	0.66

C. Chemical analysis in FTIR

FTIR spectroscopic measurements were carried out on both non-plasma and plasma treated polyimide surfaces to investigate their surface properties. The FTIR instrument used was the Nicolet, Nexus FT-IR, with a resolution of 4 cm^{-1}. The subtraction spectrum is given in Fig. 3.25, which represents the difference in intensity of plasma and non-plasma treated polyimide surfaces. In other words, the spectrum in Fig. 3.25 represents the amount of particular chemical components left on the plasma treated polyimide surface which is larger than that on the non-plasma treated one.

There is a sharp peak at 1473 cm^{-1}, which corresponds to the stretching of the aromatic rings in polyimide. The peaks at ≈1720 cm^{-1}, and 1380 cm^{-1} are C=O, and C-N stretch, respectively. The amount of C=O and C-N on plasma treated polyimide is larger. This agrees with the XPS results.

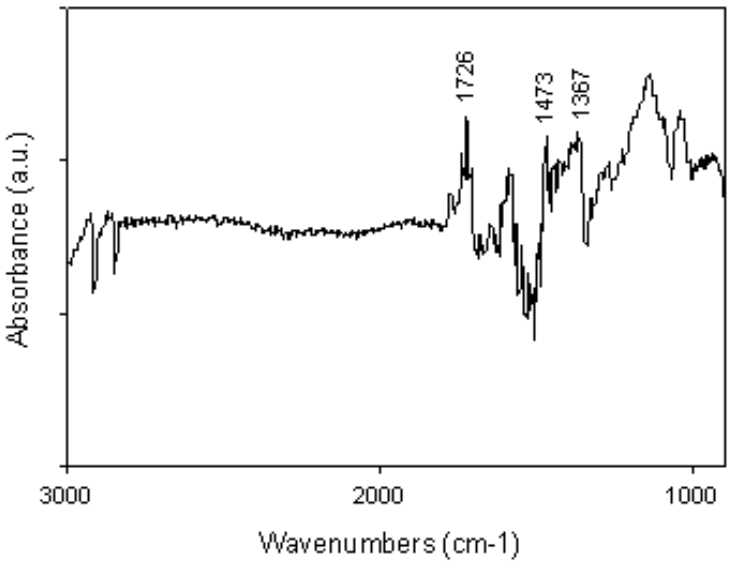

Fig. 3. 25. FTIR subtraction spectrum of PI2737

D. Surface properties

AFM was used to observe surface roughness of non-plasma and plasma treated polyimide. AFM used was the JEOL, JSPM-4200, with 25 × 25 and 85 × 85 μm^2 tube scanner and a beam-shaped Ultrasharp NT-MDT micro-fabricated Si doped tip. The surface morphology can be seen in Fig. 3.26. All units in Fig. 3.26 are in nanometers. The scanned areas of the non-plasma and the plasma treated polyimide in Fig. 3.26 are 536 × 536 nm, and 879 × 879 nm, respectively. Without considering the surface roughness, the surface area of the sensor was 3.24 mm^2. The estimated surface areas, including roughness based on the data from the scanned areas, were 5.07 mm^2 and 3.51 mm^2 for the non-plasma and the plasma treated polyimide, respectively. The surface area of the plasma-treated polyimide had increased by 44%.

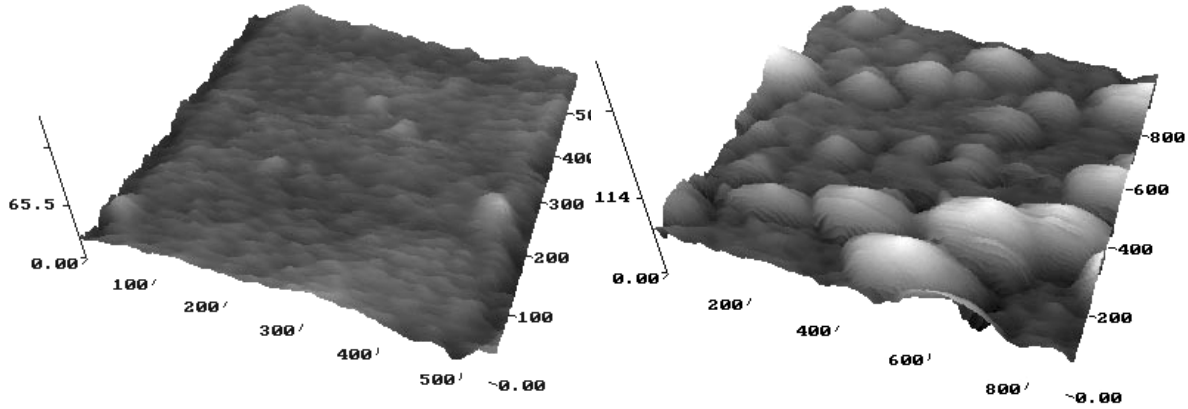

(a) (b)

Fig. 3. 26. AFM images of topography of polyimide surfaces without top electrode, (a) Non-plasma treated (b) Plasma treated

3.7.3. Discussion

XPS spectra shows the increase in intensity of carbonyl carbon and carbonyl oxygen after treating polyimide in O_2 plasma. Plasma treated polyimide in pure O_2 causes an increase in carbonyl groups, which has also been reported [3.9], however, the polyimide used was pyromellitic dianhydride-oxydianiline (PMDA-ODA) type. Leu et al. [3.10] reported that this indicates oxidation of PMDA-ODA type polyimide surface. The result of FTIR also shows the higher intensity in carbonyl carbon in plasma treated polyimide surface. The possible site where additional oxygen atoms were bonded is the benzene ring carbons. Similar observations have been reported [3.2][3.10][3.11].

With regard to the humidity sensor, the increase in carbonyl groups on the polyimide surface is likely to play a key role in sensitivity to moisture. Since carbonyl groups are very polar, a degree of this intensity should effect the intermolecular attraction and repulsion. Hydrogen in water molecules may be attracted to oxygen in carbonyl groups. The increased carbonyl groups may allocate more locations for water molecules to contribute to the sensitivity or cause the balance in dipole-dipole forces to attract more water molecules. Taking the response time into consideration, water molecules may be bonded to carbonyl groups weakly. It implies that the humidity sensor treated in O_2 plasma absorbs and desorbs water molecules faster, resulting in

smaller hysteresis. In addition, a roughened surface of polyimide with plasma effectively increases the surface area being exposed to moisture and may help the sensor uptake moisture faster. This assumption would be reasonable because although the number of carbonyl groups has increased, the amount of polyimide would decrease due to plasma etching. This means that increased surface roughness would dominate the response speed rather than the sensitivity. Since the rate of sensitivity, 240%, increased more than that of surface area, 44%, after plasma treatment, chemical modification is most likely to improve the sensitivity and hysteresis of the sensor significantly. Interestingly, linearity was maintained before and after plasma treatment. It implies that the dielectric constant in polyimide still changed linearly.

3.8. New structure for improved sensitivity

Capacitive humidity sensors commonly consist of three parts - a top electrode, a sensing layer (in this case polyimide) and a bottom electrode. This will be referred to as a non-perforated type. Since the principal of a parallel-plate polyimide-based humidity sensor is based on the change in the dielectric constant of the polyimide due to humidity, capacitance and sensitivity per % RH increase as both the area of sensor increases and thickness of the polyimide decreases. A small area is desirable from the IC industry's point of view. Alternatively, a thinner polyimide layer has more probability of pinholes through the polyimide layer. The plasma etching has been applied to increase the sensitivity of the polyimide [3.2][3.12], however, long-term stability is unknown. The new structure does not employ the approach mentioned above. This new structure consists of a top electrode – a polyimide layer with holes – a continuous polyimide layer – a bottom electrode. This will be referred to as a partially perforated type. The new structure has approximately twice the sensitivity. This improvement is observed with two types of the polyimide, which are UR-5440 and BG-2430 by Toray Industries. The advantages of this structure are few additional process steps and IC compatible process without increasing sensor area and decreasing the thickness of polyimide critically. The following subsections provide comparisons of the response characteristics in hysteresis, temperature dependence and the frequency effect with the sensors constructed in the non-perforated type and the partially perforated type.

3.8.1. Structure and fabrication

Cross-sectional figures of two types of sensors are shown in Fig. 3.27. The size of the humidity sensing area is 1.8 mm × 1.8 mm. The substrate is silicon with silicon dioxide as an insulating layer. The same process steps are applied to both types of polyimide. The differences in fabrication method between the two structures are the post bake after forming the first polyimide layer and the addition of the second polyimide layer. The first polyimide layer in the partially perforated type sensor is employed to avoid

shorting between the electrodes in the case of water condensation at high humidity. The mask used to pattern the second polyimide layer is the negative image of that used for patterning the top electrode as the polyimide used is a negative-tone photodefinable type. Holes of 80 μm in diameter are created in the top electrode in order to accelerate moisture uptake into polyimide. The final thickness of polyimide is provided in Table 3.7. The sensor was mounted and bonded onto a DIL ceramic chip carrier as Fig. 3.28 shows. Epoxy was dispensed around the sensor to prevent any short-circuit, which could occur at high humidity during measurement.

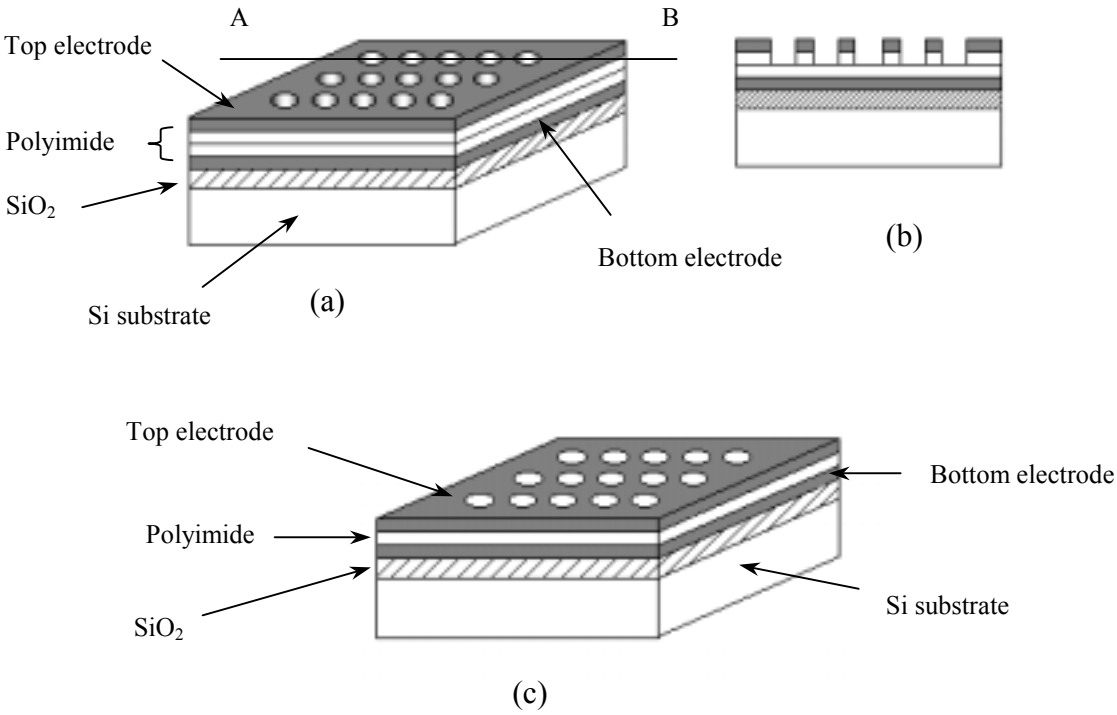

Fig. 3. 27. Sensor structures (a) Partially perforated polyimide type (b) Cross-section of the partially perforated polyimide type between A and B (c) Non-perforated polyimide type

Table 3. 7. Major specifications of fabricated humidity sensors

	UR-5440		BG-2430	
	Partially perforated	Non-perforated	Partially perforated	Non-perforated
Thickness of polyimide (μm)	(T) 0.3	0.3	(T) 0.44	0.4
	(B) 0.3		(B) 0.4	
Capacitance (pF)	222 ~ 285	274 ~ 312	162 ~ 192	210 ~ 227
ΔC (pF)	63	38	30	17
Sensitivity (%)	40.5	19.8	26.5	11.6

(T): Top layer, (B): Bottom layer

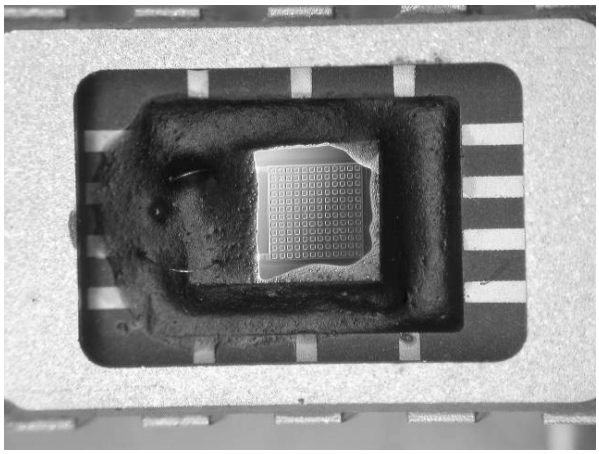

Fig. 3. 28. Humidity sensor mounted in DIL ceramic chip carrier

3.8.2. Sensitivity, linearity and hysteresis

Fig. 3.29 shows the normalized capacitance measured when the humidity increased at 25°C. The actual capacitances measured from 20% RH to 90% RH at a ramping-up rate of 1% RH/min are given in Table 3.7. The sensor fabricated with polyimide UR-5440 showed larger responses than with polyimide BG-2430. This difference resulted from their differing abilities regarding the amount of water uptake into the polyimide. It is clear from the results that the sensitivity of the sensors with the partially perforated type is approximately twice as large as that of the sensors with non-perforated type. The sensitivity of the sensor with the partially perforated type, BG-2430, is slightly more than double compared with that of the non-perforated one.

Hysteresis is observed in all cases as Figs. 3.30. and 3.31 show. The minimum and maximum of hysteresis are listed in Table 3.8 in percentage with respect to the values in increasing humidity. The minimum and maximum of hysteresis decreased in the partially perforated type in the sensor constructed with BG-2439 as Table 3.8 shows. However the large hysteresis was not reduced in the partially perforated type constructed with UR-5440.

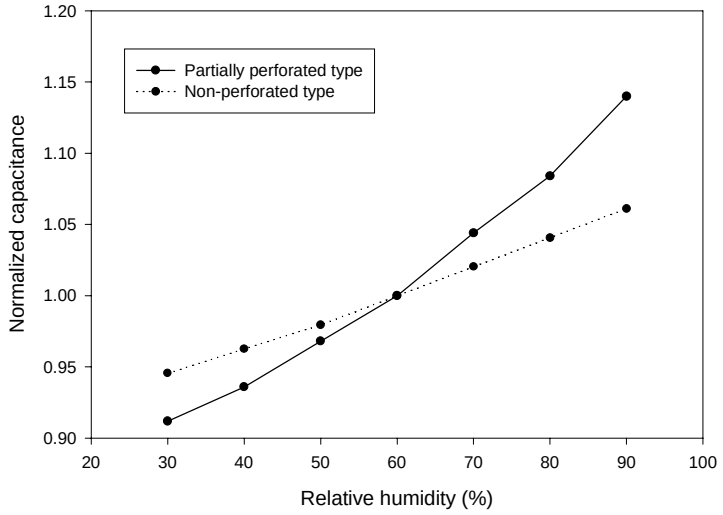

(a)

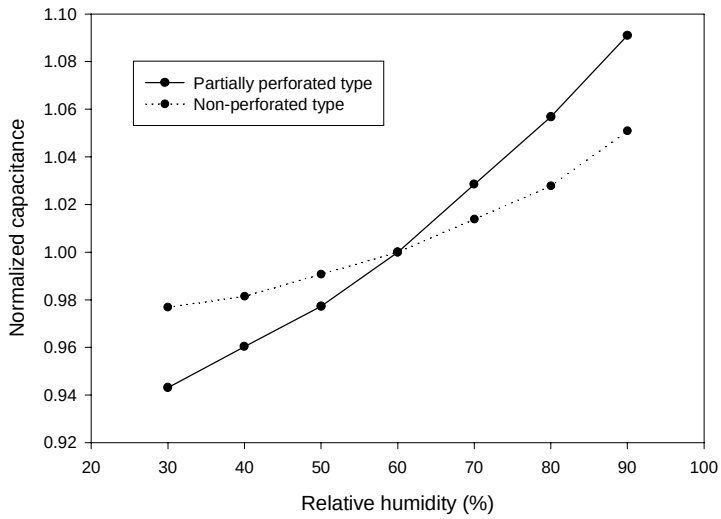

(b)

Fig. 3. 29. Normalized sensor responses in capacitance at 60% RH with 1% RH/min ramping for partially perforated type and non-perforated type (a) UR5440 (b) BG-2430

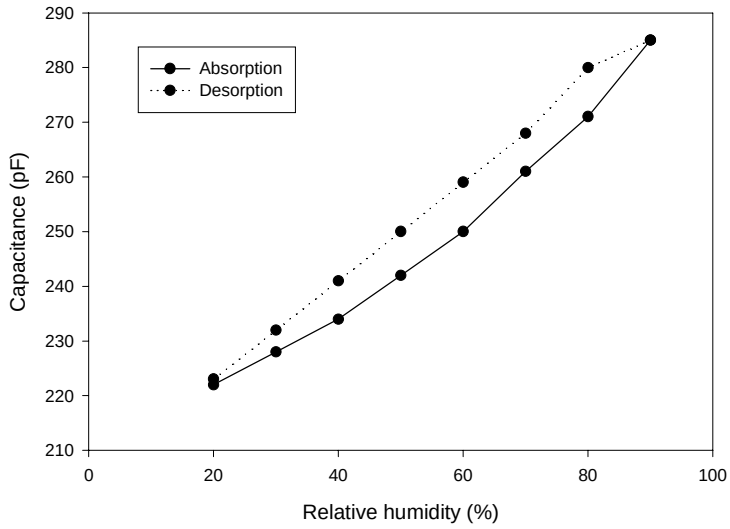

(a)

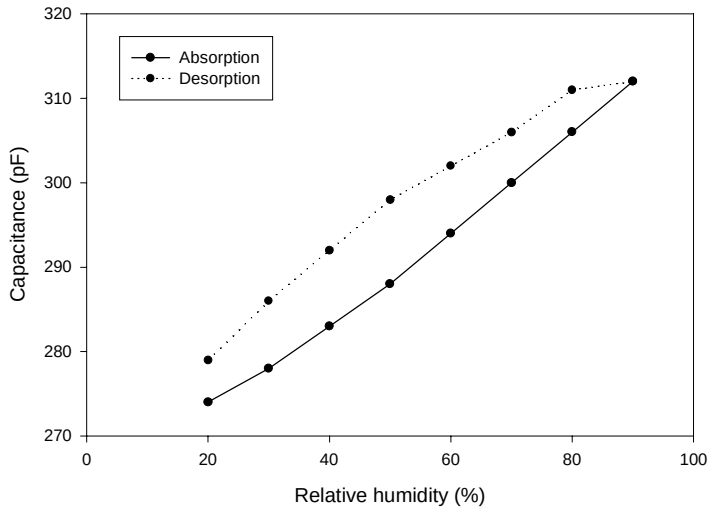

(b)

Fig. 3. 30. Hysteresis of the sensors with polyimide UR-5440 at 1% RH/min ramping (a) Partially perforated type (b) Non-perforated type

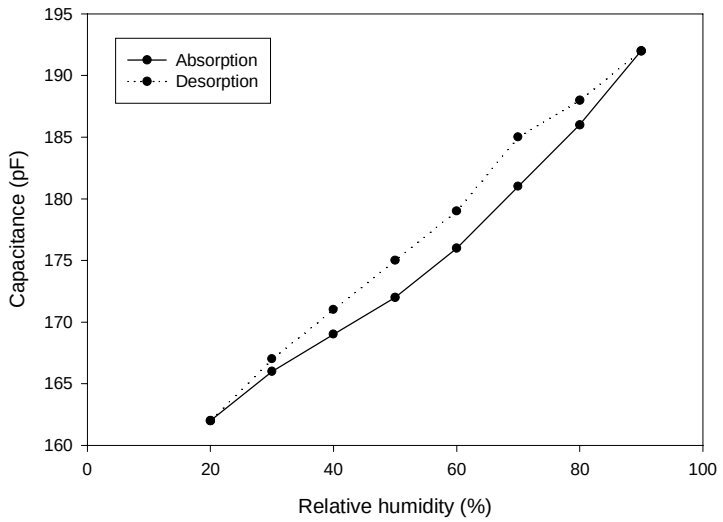

(a)

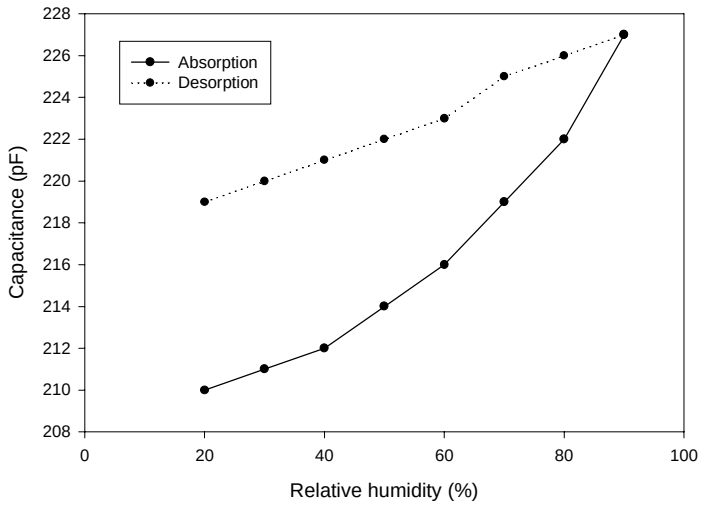

(b)

Fig. 3. 31. Hysteresis with the sensors polyimide BG-2430 at 1% RH/min ramping (a) Partially perforated type (b) Non-perforated type

Table 3. 8. Summary of minimum and maximum of hysteresis in non-perforated and partially perforated type sensors

Types	Minimum hysteresis (%)	Maximum hysteresis (%)
Non-perforated UR-5440	1.8	3.5
Partially perforated UR-5440	0.5	3.6
Non-perforated BG-2430	1.8	4.3
Partially perforated BG-2430	0.0	2.2

3.8.3. Temperature effect

Temperature effects of the sensors fabricated with both UR-5440 and BG-2430 were observed at 25˚C, 35˚C, and 45˚C. The results in Figs 3.32 and 3.33 were obtained when the humidity increased at a rate of 1% RH/min. In all cases, the temperature effect was negligibly small. This implies that water uptake by polyimide was not accelerated at elevated temperatures within the temperature range used. This is a useful characteristic for the humidity sensor.

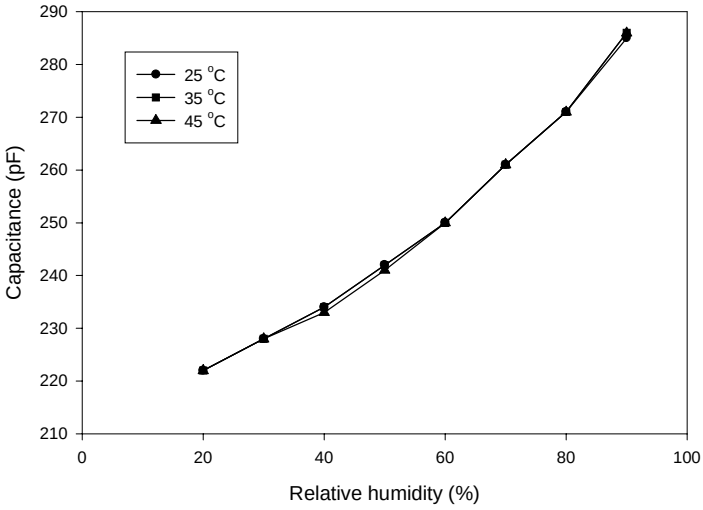

(a)

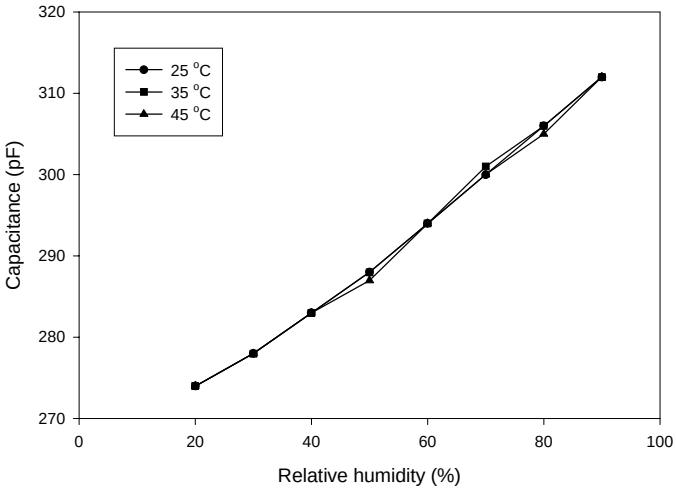

(b)

Fig. 3. 32. Temperature effect of the sensors with polyimide UR-5440 at 1% RH/min ramping (a) Partially perforated type (b) Non-perforated type

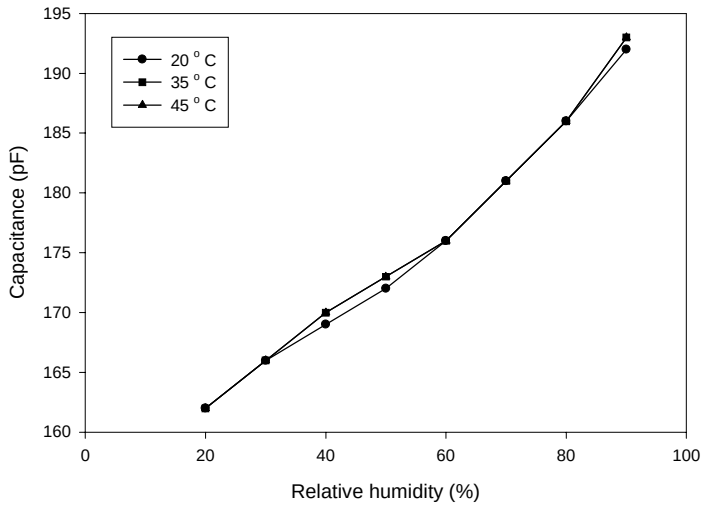

(a)

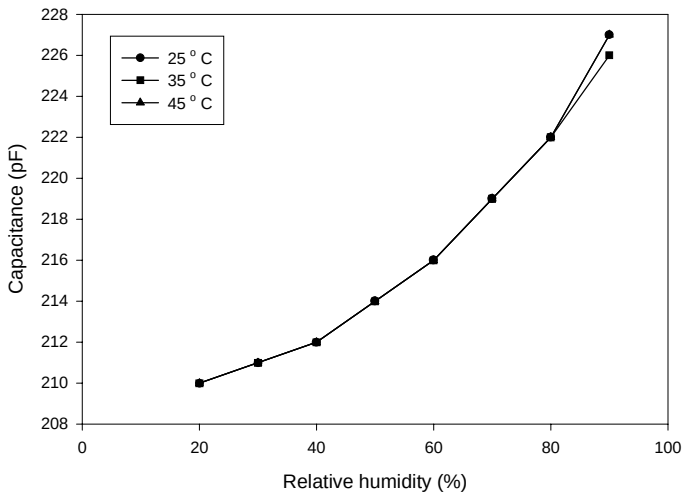

(b)

Fig. 3. 33. Temperature effect of the sensors with polyimide BG-2430 at 1% RH/min ramping (a) Partially perforated type (b) Non-perforated type

3.8.4. Frequency response

The frequency responses of the sensors fabricated with both UR-5440 and BG-2430 were observed at 500 Hz, 1 kHz, 10 kHz, 50 kHz, and 100 kHz. A LCR meter, HP 4284A, was used to measure capacitance with an amplitude of 1 V_{rms} sinusoidal signals. The results in Figs 3.34 and 3.35 were obtained when the humidity increased at a rate of 1% RH/min, 25˚C. It is clear that the largest base capacitance is observed at the lowest frequency. With regard to sensitivity, it was likely to decrease as the frequency increased. This result can be seen clearly with BG-2430 in Fig. 3.35.

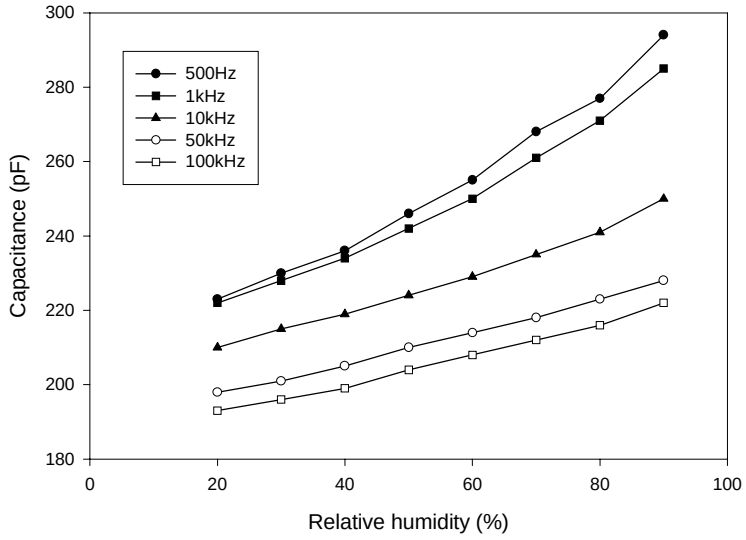

(a)

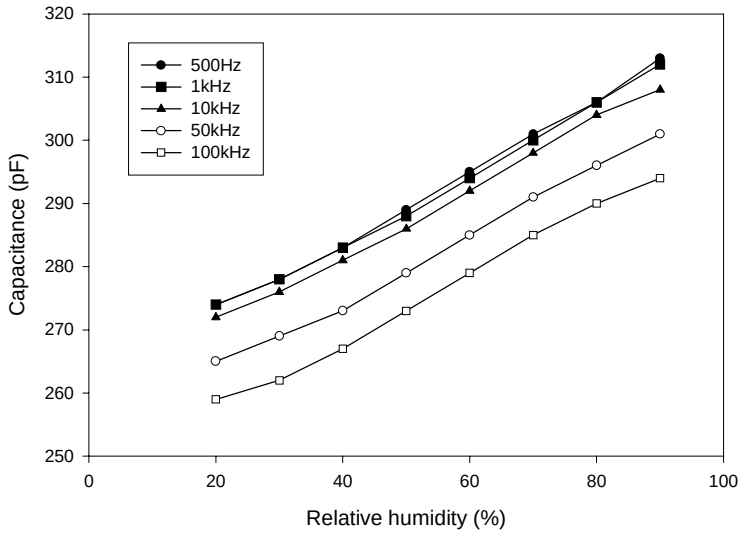

(b)

Fig. 3. 34. Frequency response of the sensors with polyimide UR-5440 at 1% RH/min ramping (a) Partially perforated type (b) Non-perforated type

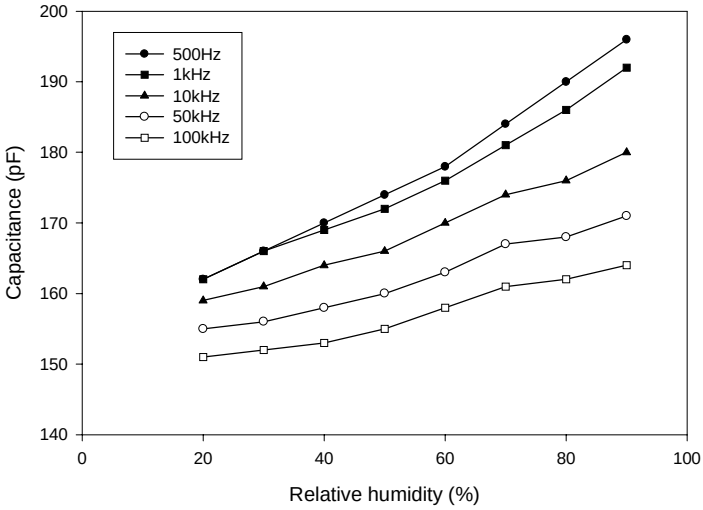

(a)

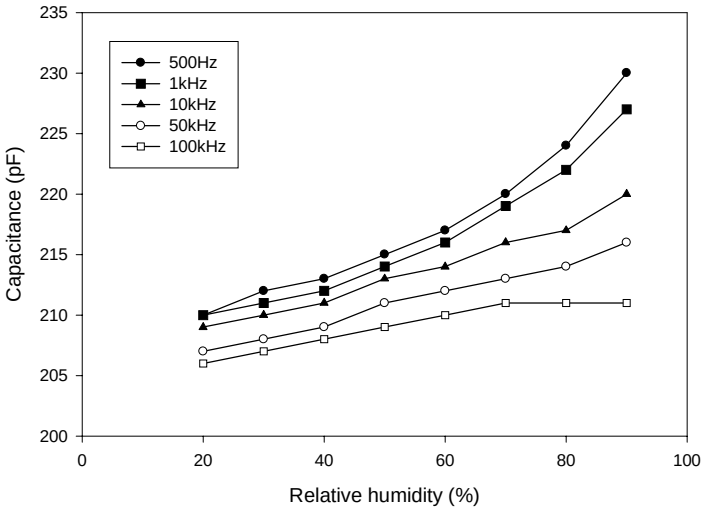

(b)

Fig. 3. 35. Frequency response of the sensors with polyimide BG-2430 at 1% RH/min ramping (a) Partially perforated type (b) Non-perforated type

3.8.5. Discussion on sensitivity

Since the structure of the sensors is parallel-plate, the dielectric constant of the polyimide is the dynamic parameter used to determine the sensor sensitivity. The dielectric constant of the same polyimide is considered to change the same manner over the same relative humidity range. One possible mechanism for the dielectric constant of polyimide to increase at different rates is the amount of water molecules incorporated in a polyimide layer. This possibility can be found with the partially perforated humidity sensor because of the increase in the polyimide's surface area. Considering moisture diffusion behavior into polyimide, it is known that the moisture absorption in polyimide is a bulk phenomenon [3.1]. It implies that water molecules diffuse through the entire polyimide layer. Two sites in the polyimide chain where the water molecule can be bound were reported [3.13]. Based on the bulk effect and bounding water molecules in the polyimide chain, the sensor with the partially perforated polyimide would allow water molecules to diffuse deeper into the polyimide layer and more effectively bound with the polyimide chain due to vertically increased surface area of the polyimide as Fig. 3.36 illustrates. This implies that the change in dielectric constant is larger due to the increased number of water molecules bounded in the polyimide chain. On the other hand, in the non-perforated type, diffusion of water molecules would easily take place in the vertical direction where holes in the top electrode and would not take place easily in horizontal direction where the electrodes are located. This implies that the change in dielectric constant is smaller.

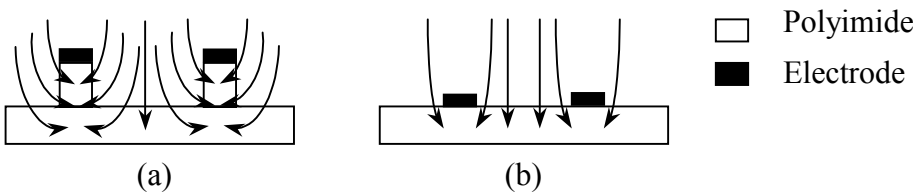

Fig. 3. 36. Illustration of water diffusion paths into a polyimide layer (a) Perforated polyimide layer case (b) Non-perforated polyimide layer case

3.9. Conclusions

Throughout this chapter, characteristics of humidity sensors are presented in terms of effects of electrode structures, curing temperature of polyimide, temperature and frequency dependences. All sensors were tested twice and found to behave similar manner.

A perforated top electrode is found it to be an effective structure for moisture uptake. The sensor treated at the lowest curing temperature, 250 ^{o}C, for polyimide showed the highest sensitivity and the fastest diffusion coefficient, however, that sensor has the largest temperature dependence and some instability. The most stable results are found with the sensor cured at 350 ^{o}C.

O_2 plasma treated humidity sensor exhibited improved moisture sensitivity. The rates of increase between the sensitivity and the surface area are not directly related. The increase of carbonyl groups is likely to be responsible for increasing sensitivity towards moisture and minimizing hysteresis. Increased surface roughness may contribute to faster water uptake. The response is governed by three possible mechanisms: the saturation capacity of the polyimide, the thickness of the polyimide, and the surface area of the polyimide. The increased response corresponds to an increase in the change in dielectric constant. The increased speed of response corresponds to an increase in surface area. The polyimide thickness affects the H_2O-free base line capacitance value of the sensor.

A new structure demonstrated the improvement of moisture sensitivity with few additional process steps. The sensors with the partially perforated polyimide layer do not show apparent inferior characteristics in temperature and frequency dependences compared with the sensors which have a non-perforated layer of polyimide. Some of results have been published [3.12] (See Appendix A – Reproduced by permission of The Royal Society of Chemistry).

References

[3.1] S.Wu, D.D.Denton, and R.D. Souza-Machado, "Dielectric behavior of O_2/CF_4 plasma etched polyimide exposed to humid environments", *J. Vac. Sci. Technol.*, A 11(2), Mar/Apr, 1993, pp. 291-300

[3.2] C.Laville, J.Y.Delétage, and C.Pellet, "Humidity sensor for a pulmonary function diagnostic microsystem", *Sens. Actuators B*, 76, June 2001, pp. 304-309

[3.3] T. Kuroiwa, T. Hayashi, and A. Ito, "A thin film polyimide based capacitive type relative humidity sensor", *Sens. Actuators B*, 13-14, pp. 89-91, 1993

[3.4] C. Laville and C. Pellet, "Comparison of three humidity sensors for pulmonary function diagnosis microsystem", *IEEE Sensors Journal*, vol. 2, no. 2, April 2002, pp. 96-101

[3.5] J.E. Morris, *Electronics packaging forum: Multichip module technology issues*, New York, NY: IEEE Press, 1993

[3.6] M.K. Ghosh and K.L. Mittal, *Polyiimides : fundamentals and applications*, New York, NY : Marcel Dekker, 1996

[3.7] H. Pranjoto and D.D. Denton, "Moisture uptake of bisbenzocyclobutene (BCB) films for electronic packaging applications", *Proc. Mat. Res. Soc. Symp*, vol. 203, pp. 295-302, 1991

[3.8] J. Crank, *The Mathematics of Diffusion*, London, Oxford Univ. Press, UK, 1975

[3.9] J. Chou, J. Paraszczak, E. Babich, J. Heidenreich, Y. S. Chaug, and R. D. Goldblatt, "X-ray photoelectron and infrared spectroscopy of microwave plasma etched polyimide surfaces", *J. Vac. Sci. Technol.*, A 5(4), Jul/Aug. 1987, pp. 1321-1326

[3.10] J. Leu and K.F. Jensen, "Fourier transform infrared studies of polyimide and poly(methylmethacrylate) surfaces during downstream microwave plasma etching", *J. Vac. Sci. Technol.*, A 9(6), Nov/Dec. 1991, pp. 2948-2962

[3.11] F.D. Egitto, F. Emmi, and R.S. Horwath, "Plasma etching of organica materials. I. polyimide in O_2-CF_4", *J. Vac. Sci. Technol.*, B 3(3), May/June 1985, pp. 893-904

[3.12] T.Suzuki, P. Tanner, and D.V. Thiel, "O_2 plasma treated polyimide-based humidity sensors", *Analyst*, vol. 127, pp. 1342-1346, 2002

[3.13] J. Melcher, Y. Daben, G. Arlt, "Dielectric effects of moisture in polyimide", *IEEE Trans. on Electrical insulation*, vol. 24, no. 1, pp.31-38, Feb. 1989

[3.14] F. Uchikawa, K. Miyao and K. Nakanishi, "Surface OH concentration and electrical resistance of humidity-sensitive silicon composite films", *Ceramic Bulletin*, vol. 63, no. 8, 1984, pp.1043-1046

Chapter 4. Multiple sensor fabrication strategies

4.1. Introduction

There are many reasons for considering integrated multiple sensors. The desired multiple sensors should be designed considering not only the number of parameters recorded but the cost effective production and small in size, particularly if the design can be manufactured using conventional IC process technologies. It is also advantageous in terms of small substrate area consumption if multiple sensors are designed and integrated on top of one another in contrast to a side-by-side arrangement. This saves on the required substrate area such as silicon, resulting in a larger number of sensors per wafer. The multiple sensors also save on packaging costs. However, there is always a compromise between the complications of process flow and the effectiveness of process cost if comparison is made between the multiple sensors and the individually made sensor, having the same functionality. This can be understood from the fact that a single defect in one of sensors ruins the whole multiple sensor.

The integrated multiple sensor dealt with throughout this chapter includes humidity, wind speed/direction and temperature sensors. This chapter reports the experimental results of thermal isolation along with silicon bulk etched and polyimide plateau structures. This experiment revealed the design consideration and importance of process feasibility in order to establish good thermal isolation for the wind speed/direction sensor, producing a low-power fast response sensor. The chapter concludes with an emphasis on the process strategies to fabricate the multiple sensors employing MEMS technology with a single-sided mask aligner.

4.2. Experimental study of thermal isolation

This study was conducted to determine the design and fabrication process of the wind speed/direction sensor, which is a part of the multiple sensor. The wind speed/direction sensor operates on the principle of a self-heating temperature-dependent resistor. The operating principle and results of this sensor can be found in [4.1]. The sensor was made on the surface of silicon nitride diaphragm, which was created using silicon back etching so called bulk micromachining. This sensor consists of four resistive elements made of nickel thin films oriented orthogonal each other. The resistive elements are heated at constant power and detect wind speed/direction simultaneously. Airflow over the resistive elements induces a temperature gradient. The upstream element is cooler than the downstream counterpart resulting in a temperature gradient in the direction of airflow. The sensor outputs are sine and cosine functions of wind direction. The direction of the temperature gradient represents the wind direction. The flow angle is determined from the ratio of the two signals obtained for north-south and east-west directional sets. The magnitude of the sensor output represents wind speed.

In order to make the sensor useful, good thermal isolation is one of the important parameters. A widely employed method is the removal of bulk silicon under a diaphragm made of silicon dioxide or silicon nitride for the purpose of achieving good thermal isolation between the silicon substrate and a sensor on a diaphragm [4.2-4.5]. Bulk silicon etching can be achieved from the underside of a silicon substrate if a double-sided mask aligner is available to center the structures. An example of front-to-back alignment procedure implemented in a commercial double-sided aligner is published in [4.6]. Alignment marks are created on the front side of a wafer first in a similar way to that used with a single-sided mask aligner. In creating alignment marks on the other side of the wafer, alignment marks on a glass mask are stored electronically before loading the wafer under the mask. The wafer is then loaded under the glass mask. The alignment marks initially created on the wafer are viewed through a microscope situated under a wafer stage. The wafer is now aligned to the stored image. Once this is

done, exposure is performed. This is the completion of front-to-back alignment. The procedure is relatively simple and makes a double-sided mask aligner a useful piece of equipment.

In this section, an experimental study of thermal isolation is reported. It was carried out in order to seek alternative structures which may provide flexibility in fabrication using a single-sided mask aligner. The results of the studies are presented with an emphasis on the following matters:

- The degree of difference in thermal isolation between a silicon substrate and heating elements for the wind speed/direction sensor, and
- Issues from the process control point of view.

Two structures were used to confirm the effectiveness of thermal isolation as in Fig. 4.1. Figs. 4.1(a) and (c) are the cross sections of silicon nitride film after back etching silicon and polyimide plateau, respectively. Their top views are shown in Figs. 4.1(b) and (d). A serpentine track was made with nickel and served as a heater. Thermopiles were made to measure the temperature change as a result of generated heat. Good thermal isolation makes it possible to operate for the wind speed/direction sensor at small power consumption [4.1]. The method of the investigations involved measuring the required power to heat the structures in Fig. 4.1 to preset temperatures.

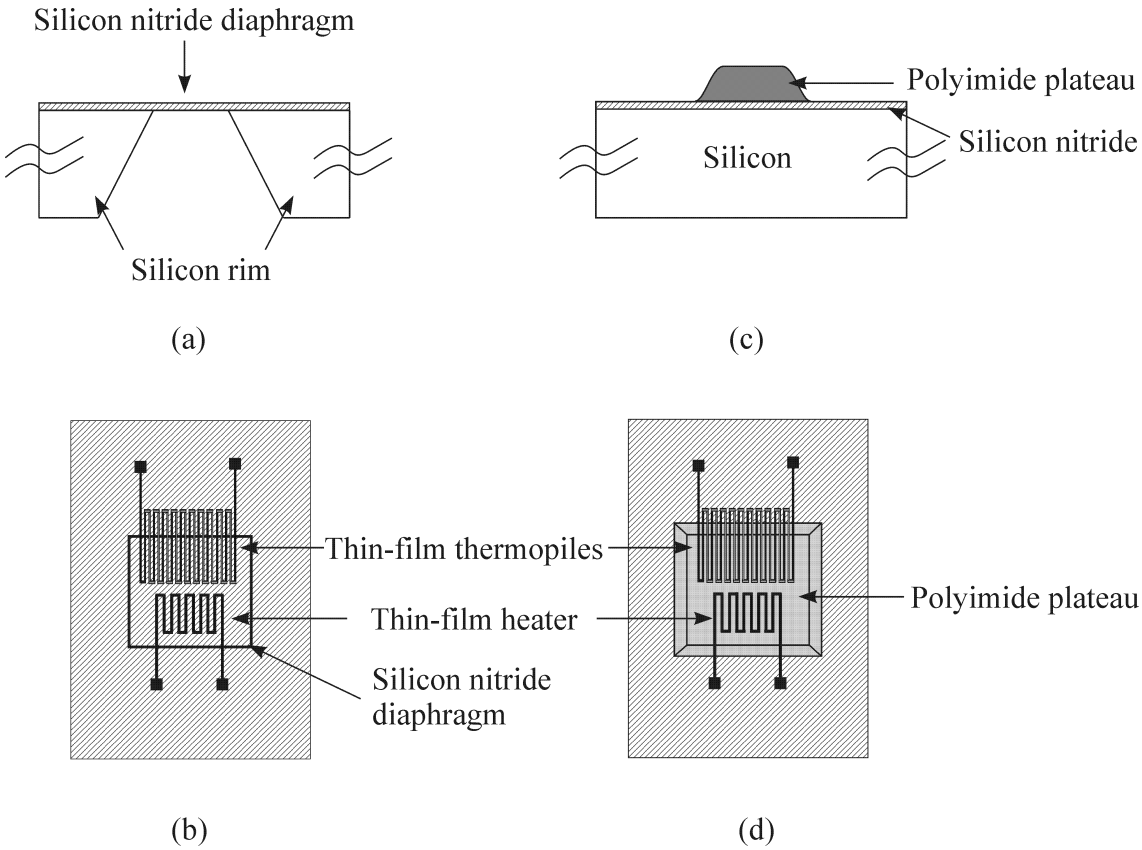

Fig. 4. 1. Structures built to test thermal isolation, (a) Cross-section of bulk micromachined silicon with silicon nitride diaphragm (b) Top view of test structure built on silicon nitride diaphragm (c) Cross-section of polyimide plateau (d) Top view of test structure built on polyimide plateau

Before presenting the results of thermal isolation, the characteristics of thin-film thermopiles were investigated. Since the e.m.f. of a single thermocouple junction varies in the order of μV/°C, employing thermopiles increases the sensitivity of the output. The junctions of the thermopiles were connected in series alternately between hot and cold junctions. The output e.m.f. ΔV_s from the number of thermocouples N at temperature difference ΔT between the hot and cold junctions can be calculated as [4.7]:

$$\Delta V_s = N(\alpha_A - \alpha_B)\Delta T \tag{4.1}$$

where α_A and α_B are the Seebeck coefficients of materials A and B, respectively.

Three types of thermopiles were fabricated in this investigation with the metals listed in Table 4.1. Each junction was formed with the combination of nickel and nichrome (NiCr), tungsten (W) or molybdenum (Mo). The nickel deposition was made using thermal evaporation. NiCr, W and Mo were deposited by RF sputtering. Ten junctions were created with the metals on the 1.5 μm-thick silicon nitride diaphragm. The silicon was etched away with TMAH (tetramethyl ammonium hydroxide) solution to create a silicon nitride diaphragm for thermal isolation.

In order to measure the temperature response of the thermopiles, a nickel heater was separated from the hot junctions by 100μm. The heater element and hot junctions of the thermopile were placed on a silicon nitride diaphragm. Cold junctions were placed on the silicon rim covered with silicon nitride. One of fabricated thermopiles with a nickel heater is shown in Fig. 4.2. The area of the diaphragm is 1.3 mm × 1.3 mm. A cross mark in Fig.4.2 is the location where an additional thermocouple was placed for monitoring heat transfer from the heater to the silicon substrate. The resistance of an individual nickel heater incorporated in three substrates was measured to be approximately 235 Ω at room temperature. The temperature coefficient of the nickel between room temperature and 100 ˚C was calculated to be 0.0065 K^{-1}. Thus the temperature of the element can be calculated from its resistance once the value is established. Fig. 4.3 shows the temperature change of the heater as a function of power supplied to the heater. The heater burnt out when the power exceeded 68.5 mW.

Table 4. 1. Materials used in thermopiles

	Metal A	Metal B
Tp1	Nickel	Nicrhome (80 Ni : 20 Cr)
Tp2	Nickel	Tungsten
Tp3	Nickel	Molybdenum

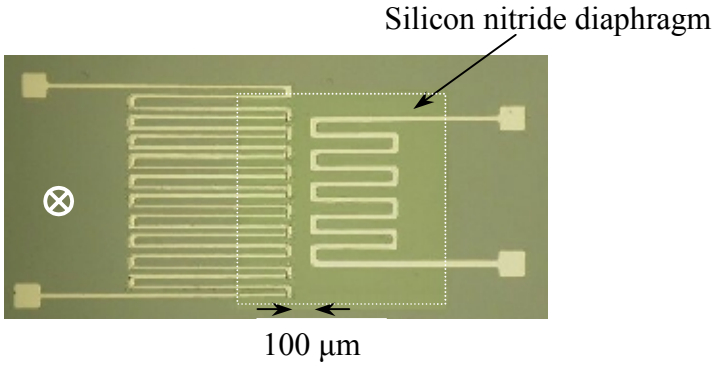

Fig. 4. 2. Fabricated thermopiles and a heater on a silicon nitride diaphragm

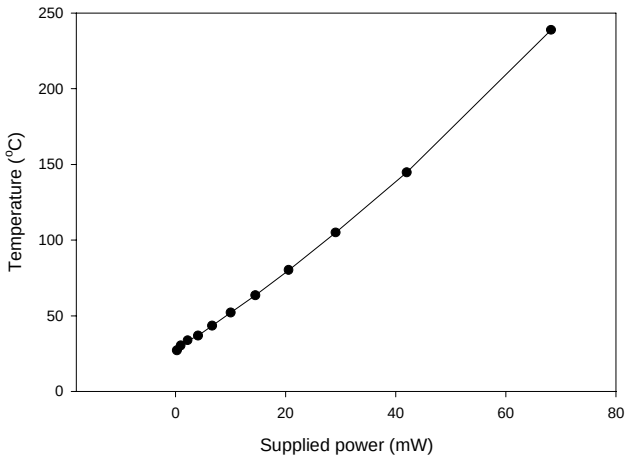

Fig. 4. 3. Temperature output of the nickel heater as a function of supplied power

With this heater, temperature measurements were carried out using the three thin-film thermopiles Tp1, Tp2 and Tp3. The setup used for this measurement is shown in Fig. 4.4. Each sample was placed between the glass slides to lift a sample from the metallic stage. The equipment used for this measurement was HP4145B, Semiconductor Parameter Analyzer. The analyzer supplied specified current for 20s at each measurement, which was sufficient duration for establishing a steady reading. The output voltage of thermopiles was read by increasing heater power to approximately 68

mW. The results are plotted in Fig. 4.5 and show reasonably linear response. The thermoelectric power of Ni-NiCr, Ni-W and Ni-Mo are found to be 0.14 mV/K, 0.045 mV/K and 0.085 mV/K, respectively. The relative non-linearity of Ni-NiCr was found to be 9.5%. In order to find out the source of this non-linearity, thermal conductivity loss from the diaphragm to nearby silicon substrate was investigated. The thermocouple was placed where a cross symbol is located in Fig. 4.2. The worst thermal loss to the silicon substrate equated to 1 ˚C when the heater generated temperature was approximately 216 ˚C. This temperature loss represents only 0.46% of the generated heat. Other causes of thermal loss may include thermal radiation from the heater to air, the quality of the junction made of two dissimilar metals, or non-identical property of each junction due to contaminations.

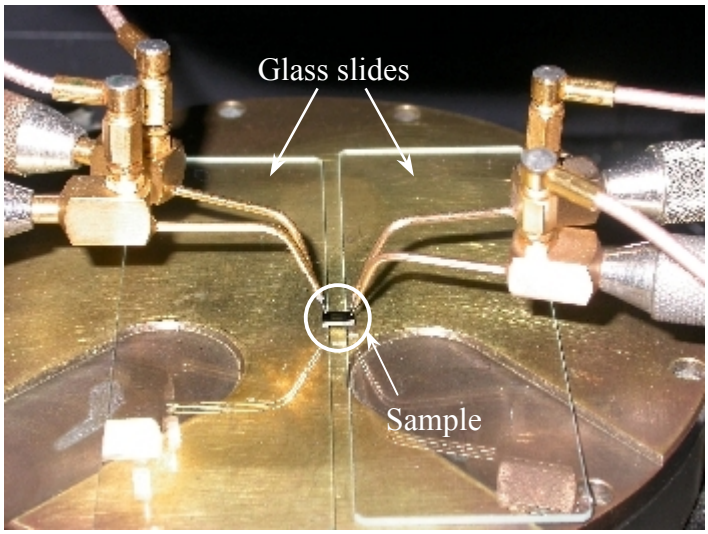

Fig. 4. 4. Probe station setup for testing responses of thermopiles

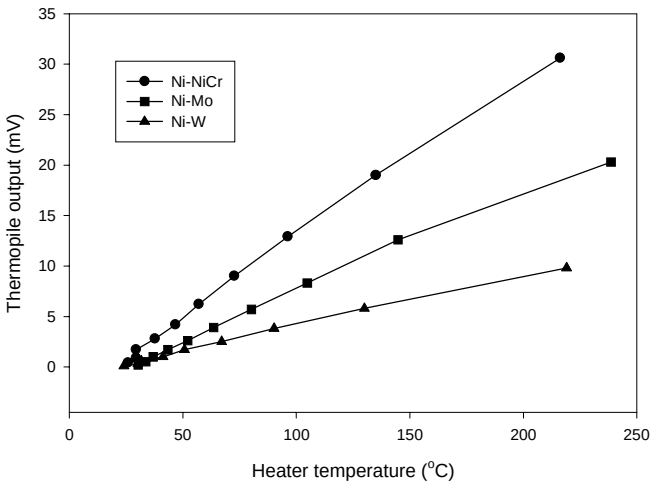

Fig. 4. 5. Outputs of thermopiles as a function of nickel heater temperature

Since the experimental results show the largest thermoelectric power was obtained from Tp1 (Ni-NiCr thermopile), this thermopile was fabricated on a thick polyimide plateau on a silicon nitride layer coated on a silicon substrate in conjunction with a nickel heater. A picture of this structure is shown in Fig. 4.6. The thickness, top and bottom areas of the polyimide plateau are 27 μm, 1.65 mm × 1.7 mm, and 1.95 mm × 1.98 mm, respectively.

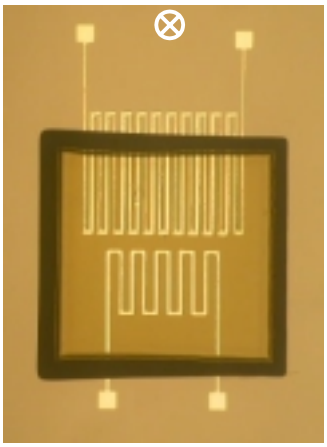

Fig. 4. 6. Fabricated 27 μm-thick polyimide plateau with nickel heater and Ni-NiCr thermopiles

A comparison can be made in power consumption of the heaters on the silicon nitride diaphragm presented earlier and the polyimide plateau when the heaters were heated. As Fig. 4.7 shows, much higher power is consumed in the heater created on the polyimide plateau to generate the same amount of heat. The e.m.f.s of the Tp1 thermopiles on the diaphragm and the polyimide plateau were also compared when the heaters were heated in the same way as in Fig. 4.7. The output of the thermopile on the polyimide plateau was very small, which can be seen in Fig. 4.8. In order to check how much heat was transferred to bulk silicon, a thermocouple was placed where a cross mark is located. The temperature increase at this location was about 4 ˚C when the heater reached 151 ˚C. Namely, 2.6% heat loss was found at the furthest location from the heater. This implies that there is heat conduction from the heater through the polyimide plateau into silicon substrate.

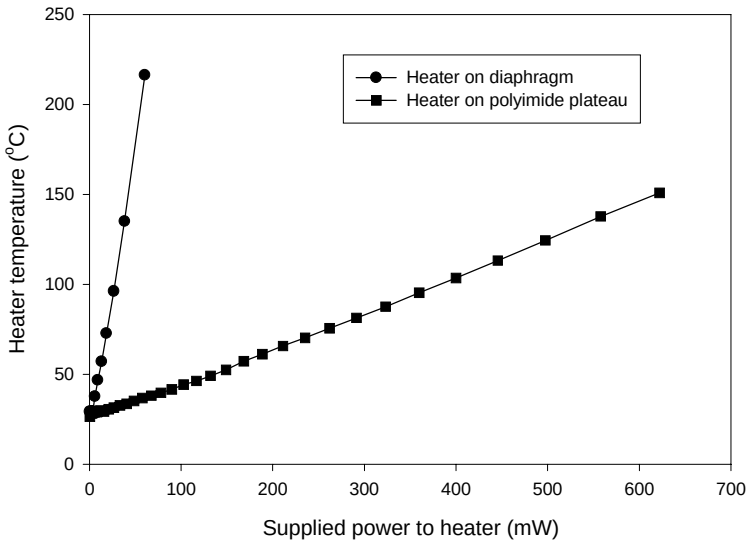

Fig. 4. 7. Comparison of nickel heater temperature as a function of supplied power to the heaters on silicon nitride diaphragm and polyimide plateau

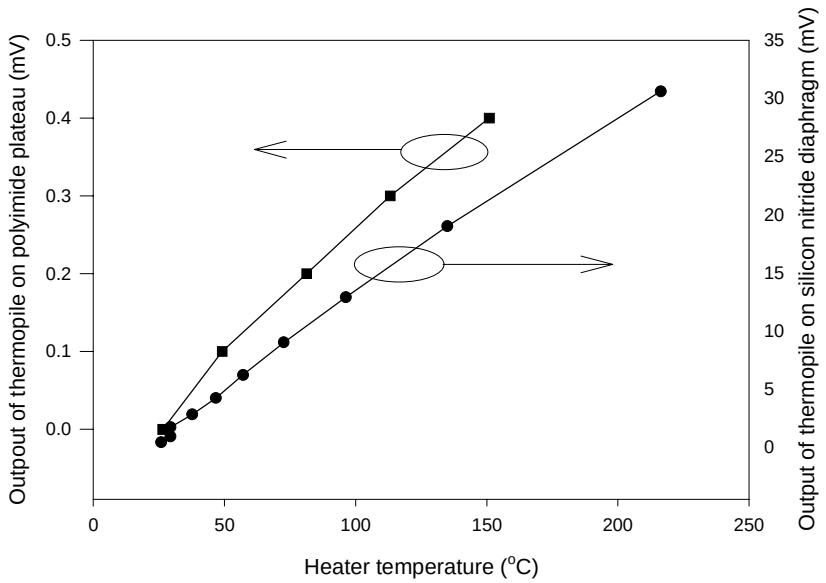

Fig. 4. 8. Comparison of thermopile outputs on the silicon nitride diaphragm and the polyimide plateau as a function of nickel heater temperature

In addition to poor thermal insulation of the polyimide plateau, the disadvantages of this structure were discovered from a process control point of view. The fundamental issue is that tight fabrication control is required to create a constant slope along the polyimide edges. This slope helps step coverage of the metallization between the top and bottom of the polyimide plateau. Unlike steppers commonly used in IC processes, depth of focus (DOF) point is not of concern with mask aligners. The DOF of steppers is typically between 1.0 and 1.5 μm [4.8], meaning the stepper cannot focus high aspect ratio structures. However, a good definition of photoresist starts becoming difficult if a mask is too far from the photoresist layer even when a mask aligner is used. This is the case with the polyimide plateau. As Fig. 4.9 illustrates, a good definition of photoresist is achievable on top of the polyimide plateau due to contact exposure but there is no contact outside the polyimide plateau due to a 27 μm gap. Another issue is the uneven photoresist along the sidewall of the polyimide plateau. This was observed on the sidewall facing the center of a wafer as illustrated in Fig. 4.10.

This results from the centrifugal force while spinning the photoresist. The thick polyimide plateau prevents photoresist from spreading evenly. This uneven photoresist also results in poor pattern definition.

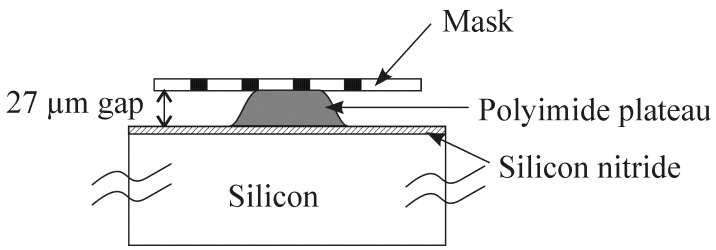

Fig. 4. 9. Illustration of photolithography conditions with polyimide plateau

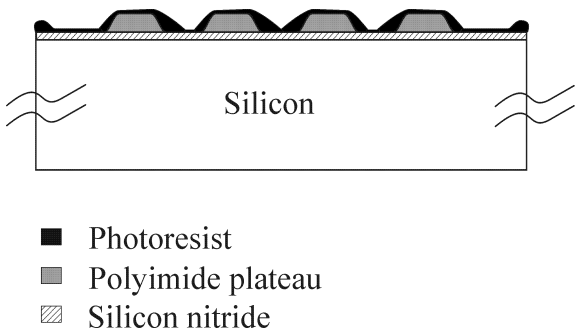

Fig. 4. 10. Illustration of unevenly spun photoresist

4.3. Key strategies for multiple sensor fabrication

As the results in section 4.2 indicate, the structure with a diaphragm created by etching the silicon underneath results in good thermal isolation. Thus, the multiple sensor elements (humidity, wind speed/direction and temperature) were created on top of a silicon nitride diaphragm. A cross sectional view and a top view of the sensor are illustrated in Fig. 4.11. Nickel was used for electrodes and wind speed/direction sensor. Polyimide was used for the humidity sensing material.

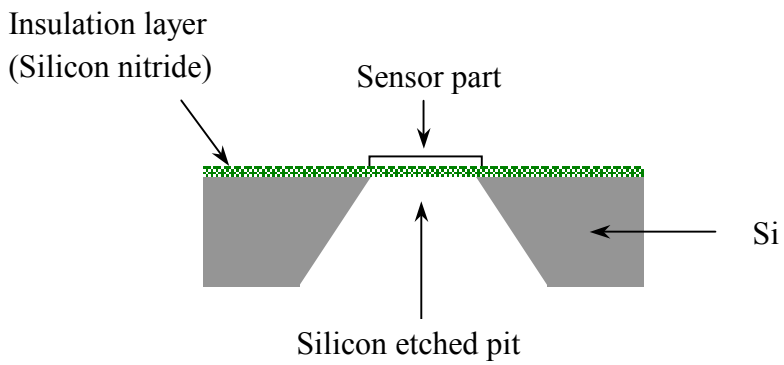

(a)

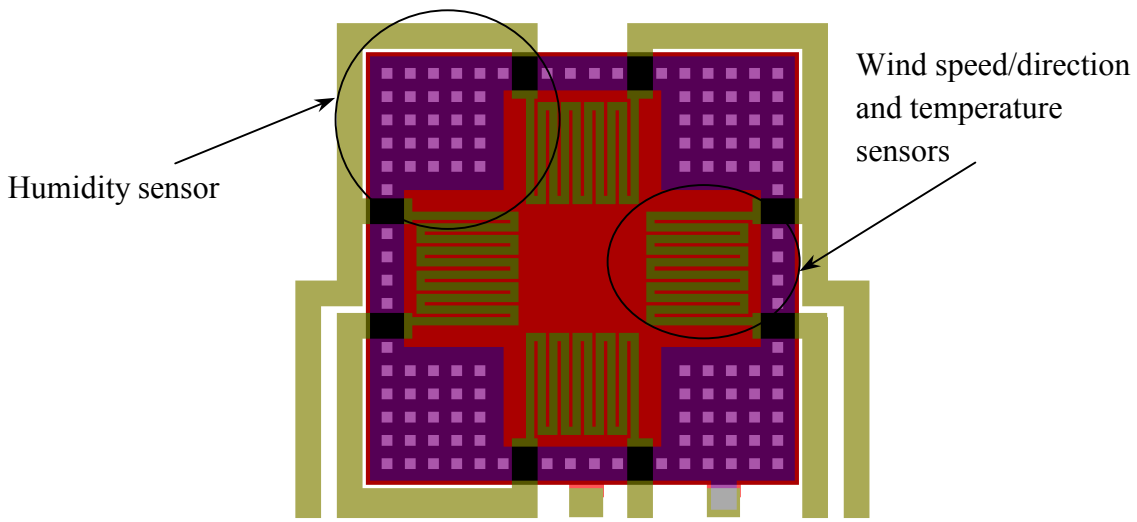

(b)

Fig. 4. 11. Illustration of multiple sensor: humidity, wind speed/direction and temperature sensors (a) Cross sectional view (b) top view

The highlights in this section are strategies to fabricate multiple sensors with bulk micromachining techniques using a single-sided mask aligner. The key challenges of the fabrication are:

- Alignment strategy between front and back side of alignment marks
- Photoresist removal strategy without damaging polyimide after etching nickel
- Sensor protection strategy while back-etching silicon

The solutions to the issues that made it possible to fabricate the multiple sensors successfully are listed in Table 4.2.

Table 4. 2. Lists of solutions to the key issues for fabricating the multiple sensors

Issues	Solutions
Alignment strategy	Create alignment marks by etching silicon through wafer
Photoresist removal strategy	Use PAN* wet etchant
Sensor protection strategy	Use resin on sensor side

* Combination of Phosphoric acid, Acetic acid, Nitric acid

Alignment marks were used for patterning both the front and back sides of a wafer. The alignment marks were created with an anisotropic wet etching method (so called bulk micromachining). The alignment through-holes depend on the silicon crystal orientation. {100} crystal orientation wafers were used in this fabrication. This crystal orientation is commonly used in CMOS processes [4.9], which are useful with a view to integration of the sensors together with sensor support electronic circuitry. It was decided that the alignment through-holes were to be parallel to the primary flat of a wafer as illustrated in Fig. 4.12 (a). The size of alignment through-holes was predictable and proved fairly accurate with this alignment method. The size of window to be

opened on the back surface of wafer needed to be larger than that on the front side of wafer by $\sqrt{2} \times$ thickness of wafer. This is due to the characteristics of the profile after anisotropic wet etching, which is shown in Fig. 4.12 (b). Since {111} is the slowest plane to be etched, the size of windows opened on the back of the wafer parallel to the primary flat is virtually the same after etching. In other words, unlike the window opened in parallel to {100} planes, the alignment through-holes presented here do not expand beyond the window size opened in silicon nitride on the back of the wafer.

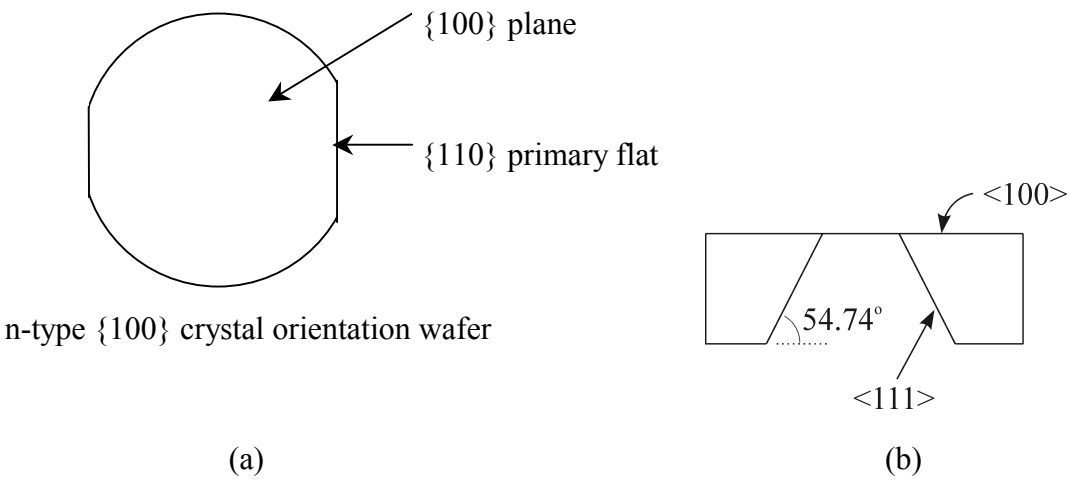

Fig. 4. 12. Crystal orientation of wafers used, (a) wafer cut for n-type {100} wafer (b) slope after anisotropic wet etching {100} wafer aligned parallel to {110} plane

The wet etching method used to etch metals generally requires the photoresist to be heated at high temperatures - so called a hardbake process. This ensures that the photoresist stays intact in acid etchant after patterning the photoresist. Once the etching is complete, the photoresist must be removed. This can be done by plasma etching or commercially available photoresist removal solution. The drawback of these methods is the damage to the polyimide. Photoresist can be etched with oxygen gas in plasma etching. However, polyimide is also known to be etched away with oxygen gas in plasma etching. Commercially available photoresist removal solutions are most likely to damage polyimide. It is also important to examine if nickel etchants require photoresist for hardbake. Some of known nickel etchants are listed in Table 4.3.

Table 4. 3. Some examples of nickel wet etchant [4.10]

1	5 HNO_3, 5 CH_3COOH, 2 H_2SO_4 + H_2O as desired
2	1 HNO_3, 1 HCl, 3 H_2O
3	3 HNO_3, 1 H_2SO_4, 1 H_3PO_4 (98%), 5 CH_3COOH

The photoresist used throughout the experiment was SPR-511A from Shipley, Inc. It was found that they all required hard-baked photoresist. The solution to this problem is finding an alternative etchant, which does not require photoresist for hardbake. The reason is that if the photoresist is not baked hard, acetone can be used to remove it without difficulty. This problem was solved with the application of PAN etchant, which is commonly used as an aluminium wet etchant. PAN is prepared as follows:

- Mixing ratio = 80 parts of 85 % H_3PO_4 : 16 parts of 100% CH_3COOH : 4 parts of 70 % HNO_3 .

This PAN etchant is not aggressive under certain temperatures so that photoresist is left at softbake. The working temperature of PAN is, however, very important. The etch rate of nickel at room temperature is extremely low. On the other hand, the etch rate of nickel increases significantly at temperatures above 60 ºC. If the working temperature is too high, softbaked photoresist is attacked, and over-etching of nickel becomes significantly larger, which no longer maintains the designed dimension of nickel metallization structures. The working temperature was determined to meet three requirements; fast etch rate, no effect on softbaked photoresist and minimal over-etching on nickel metallization. The suitable working temperature was determined to be between 50 ºC and 55 ºC. Alternatively, the lift-off technique might be suggested for nickel patterning. The lift-off technique, however, tends to be unreliable once dimensions become small. In addition, this technique cannot accommodate heating

substrate during metal deposition, which was required in this multiple sensor fabrication process.

After creating all sensors on the silicon nitride coated front surface, bulk micromachining was used to etch away the silicon underneath the sensors. Some form of protection on the sensor side is required because polyimide is also etched away while etching silicon with KOH (potassium hydroxide) or TMAH anisotropic etching solutions. On the other hand, KOH and TMAH solutions do not etch nickel metallization. A jig to protect the sensor side was not employed to allow flexibility with handling a variety of substrate sizes. Instead, the terpene-phenol based resin was applied to protect sensor side while etching silicon. The resin also provides the diaphragm under the sensor with mechanical support. The resin is applicable to any size of substrate and removed easily after etching.

4.4. Process details

In this subsection, fabrication process details of the multiple sensor are presented using the strategies described in 4.3. Wafers used in the multiple sensor fabrication are n-type, {100} crystal orientation with a thickness of 600 μm. A 1.5 μm-thick PECVD silicon nitride film was deposited on both sides of the wafer. Initial wafer cleaning was required but it is not described here as it is a standard process. The major process steps are presented sequentially in this section.

(1) Create alignment marks

Nickel was deposited on both sides of the silicon substrate in order to ensure that damage in silicon nitride was minimized in the subsequent silicon etching process and wafer handling. During nickel deposition with an RF sputterer, the substrate was heated to 200 ºC to improve adhesion. This nickel layer serves primarily as one of the masks used during silicon etching.

Photoresist was spun on the front side followed by the hardbake process.

Photoresist spun on the underside was patterned with the mask in Fig. 4.13. The mask was aligned along (110) crystal plane. After hardbake photoresist, the nickel was etched with PAN, and silicon nitride was etched in boiling buffered hydrofluoric acid (BHF). Once the silicon nitride was etched away, the photoresist was removed. Resin was coated onto the front side of the substrate. The substrate was immersed in TMAH solution at 90 ºC to etch silicon where alignment marks were created. Once etching was complete, the resin was removed.

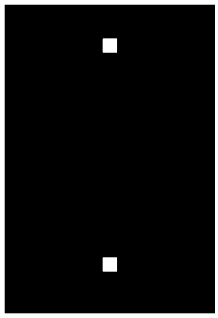

Fig. 4. 13. Mask for front-to-back alignment through holes

(2) Pattern silicon nitride where etched pits will be created under the sensors

Photoresist was spun on the front side followed by the hardbake. Photoresist spun onto the reverse side was patterned with the mask in Fig. 4.14, which created windows in silicon nitride for etching silicon underneath the sensors. After the hardbake photoresist, silicon nitride was etched in boiling BHF. After etching the silicon nitride was complete, the photoresist was then removed.

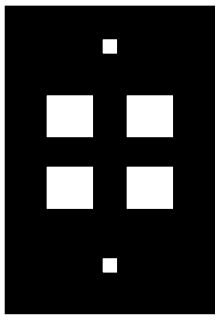

Fig. 4. 14. Mask for creating etched pits under the sensors

(3) Create bottom electrode of humidity sensor

Nickel deposition was carried out by an RF sputterer while heating the substrate at approximately 180 ºC. The thickness of nickel was approximately 100 nm. After spinning and softbake photoresist, the bottom electrode of the humidity sensor was pattered as Fig. 4.15 shows. Nickel was etched with PAN etchant in a warm bath kept between 50 ºC and 55 ºC. The photoresist was removed with acetone after etching.

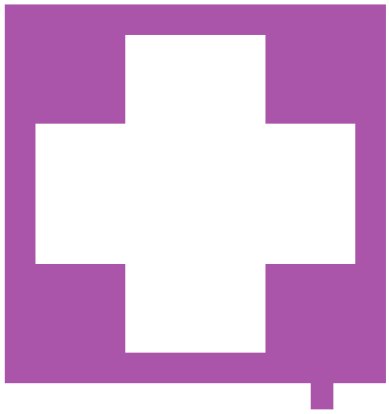

Fig. 4. 15. Pattern for bottom electrode of humidity sensor

(4) Humidity sensing 1st polyimide layer

Polyimide was spun at 4000 rpm for 30s after initial spread at 500 rpm for 5s. The polyimide was heated on a hot plate at 80 ºC for 3 min followed by at 100 ºC for 3 min. Since this polyimide is negative type, the polyimide remained at the clear part of the mask. The polyimide was developed and rinsed as the manufacturer specified. The polyimide remained as Fig. 4.16 shows once development was complete. In preparation for the next polyimide coating, a soft cure was carried out at 140 ºC for 15 min. This temperature removed the solvent, which reacts with UV and allows the patterning of structures.

Fig. 4. 16. Humidity sensing 1st polyimide layer after patterning

(5) Humidity sensor 2nd polyimide layer

Polyimide was spun and heated as the same way as the 1st layer previously mentioned. After completing development and rinsing, the polyimide was cured at 140 ºC for 30 min initially, ramped up with a rate of 20 ºC/min to 350 ºC and maintained at 350 ºC for 1 h. Gradual cooling was necessary until room temperature was reached. Nitrogen was continuously supplied into a furnace throughout the entire curing process. Fig. 4.17 shows the 2nd polyimide layer at the end of this process. At this point, the thickness of each polyimide layer was about 0.3 μm.

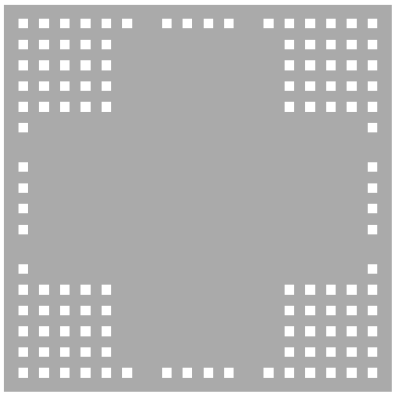

Fig. 4. 17. Humidity sensing 2nd polyimide layer after patterning

(6) Creating the top electrode of the humidity sensor

The top electrode was created as the same way as the bottom electrode in process (3). Fig. 4.18 shows the top electrode following completion of this process step. The thickness of nickel was about 100 nm.

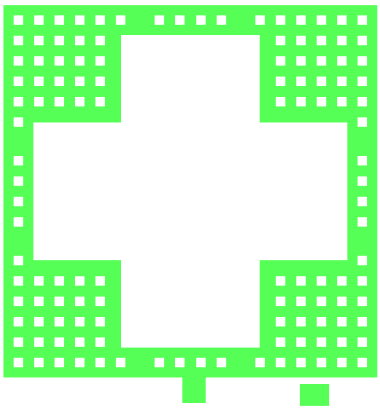

Fig. 4. 18. Pattern for top electrode of humidity sensor

(7) Insulation layer

Polyimide was spun the same way as the 2nd polyimide layer of humidity sensor in process (5). The mask used was the same as that for the 1st polyimide layer in (4). This insulation layer was necessary to electronically isolate the humidity, the wind speed/direction and the temperature sensors that were created in step (8).

(8) Wind speed/direction and temperature sensors

These sensors require a good temperature coefficient of nickel to achieve a high degree of sensitivity. Thermally evaporated nickel met the requirement in our fabrication facilities. It was, however, discovered that thermally evaporated nickel suffered from poor adhesion on silicon nitride. Sputtering a thin nickel, 30 nm before evaporating nickel was a solution to this problem. Heating the substrate at 180 ºC during evaporation was also necessary. The process of etching nickel was the same as that used for the electrodes of humidity sensor. Fig. 4.19 shows the wind speed/direction and

temperature sensors after patterning nickel.

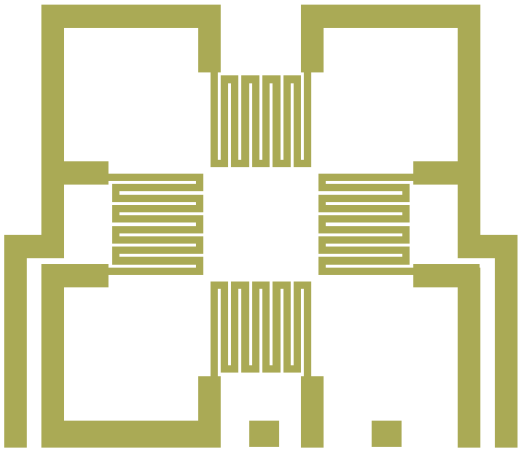

Fig. 4. 19. Pattern for wind/speed direction and temperature sensors

(9) Back etching silicon

Resin was spun on the front surface and cured until the solvent was evaporated. The substrate was immersed into 14 wt% TMAH solution at approximately 70 ºC for 10 hours. After completion, the resin was removed with isopropyl alcohol.

A picture of the completed multiple sensor is shown in Fig. 4.20, in which the diaphragm is lit from the back. The size of the sensor after dicing is approximately 4.2 mm × 3.7 mm. A cross-sectional view is shown in Fig. 4.21, revealing a profile of <111> walls on silicon. To our knowledge, this is the first time that the integration of humidity, wind speed/direction and temperature sensors has been achieved. This multiple sensor has been designed and fabricated under a CRC **micro**Technology project supported by Motorola Inc. When integrated with signal conditioning and sensor control circuitry, it is envisaged that this multiple sensor will become a valuable product in such applications such as agriculture, building HVAC systems and many others.

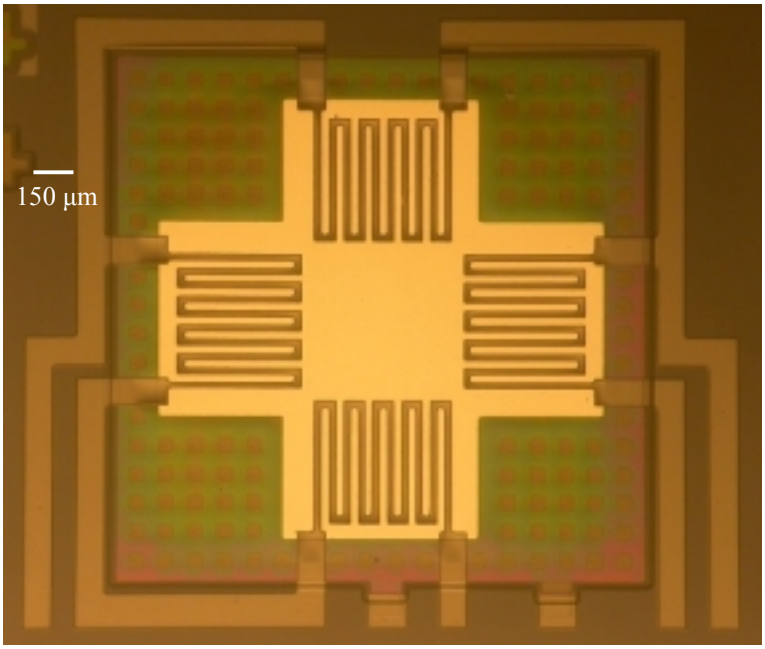

Fig. 4. 20. Photograph of completed multiple sensor with back lit to show silicon nitride diaphragm

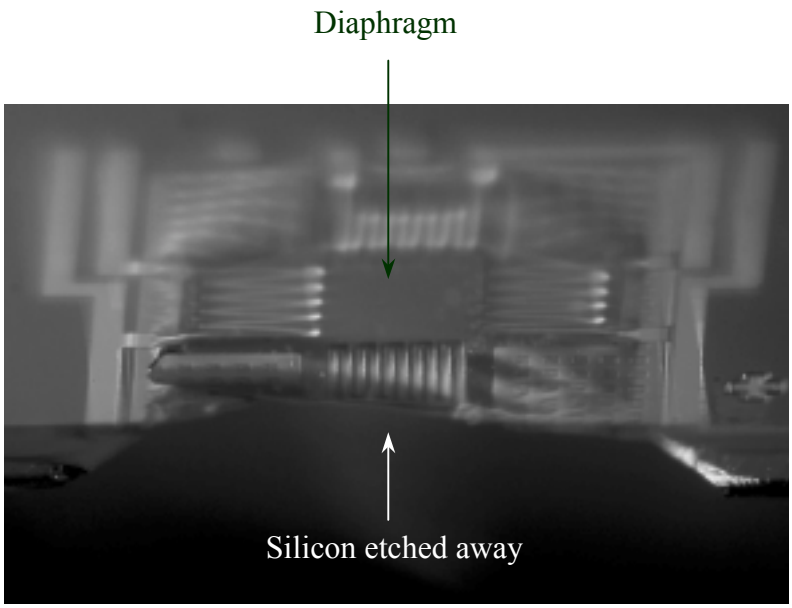

Fig. 4. 21. Cross-sectional view of multiple sensor

4.5. Conclusions

Structural differences greatly affected the thermal isolation methods used in thermal sensors. This was demonstrated with thermopiles and a nickel heater fabricated on a silicon nitride diaphragm and polyimide plateau. The silicon nitride diaphragm isolated heat very effectively, on the other hand the polyimide plateau acted as a large heat sink. In addition, maintaining constant process control was difficult with the polyimide plateau. Another concern of the polyimide plateau is that this structure may cause disturbance to the laminar flow due to a large bump on the airflow path. Based on the experimental results, the multiple sensor was fabricated on a silicon nitride diaphragm. The fabrication issues, namely the alignment between the front and back of the wafers using a single-sided mask aligner, the removal of photoresist without damaging polyimide and back etching without a protection jig on the sensor side, were overcome. The process strategies presented in this chapter are a good example of how to fabricate a structure, which requires a bulk micromachining without a double-sided mask aligner. The fabrication techniques of the multiple sensor reported here require eight masks and four materials; silicon, silicon nitride, nickel and polyimide. The yield of the multiple sensor was found to be above 80%.

References

[4.1] R.J. Adamec, D.V. Thiel, and P. Tanner, "MEMS wind direction detection: From design to operation", *Conf. on IEEE Sensors 2003*, Toronto, Canada, 21-24 Oct. 2003, pp. 340-343

[4.2] A.W. Van Herwaarden, D.C. Van Duyn, B.W. Van Oudheusden and P.M. Sarro, "Integrated thermopile sensors", *Sens. Actuators A*, vol. 21-23, pp. 621-630, 1989

[4.3] T.M. Betzner, J.R. Doty, A.M. Hamad, H.T. Henderson and F.G. Berger, "Structural design and characteristics of a thermally isolated, sensitivity-enhanced, bulk-micromachined, silicon flow sensor", *J. Micromech. Microeng.* vol.6, pp. 217-227, 1996

[4.4] D. Jaeggi, H. Baltes and D. Moser, "Thermoelectric AC power sensor by CMOS technology", *IEEE Electron Device Lett*., vol. 13, no. 7, July 1992, pp. 366-368

[4.5] K. Petersen, J. Brown and W. Renken, "High-precision, high-perfprmance mass-flow sensor with integrated laminar flow micro-channels", *IEEE 3rd Int. Conf. on solid-state sensors and actuators (Transducers '85)*, Philadelphia, PA, U.S.A., 11-14 June 1985, pp. 361-363

[4.6] N. Maluf, *An introduction to microelectromechanical systems engineering*, Artech House, Norwood, MA, 2000

[4.7] S.C. Allison, R.L. Smith, D.W. Howard, C. González, and S.D. Collins, "A bulk micromachined silicon thermopile with high sensitivity", *Sens. Actuators A*, vol. 104, pp. 32-39, 2003

[4.8] C.Y. Chang and S.M. Sze, *ULSI Technology*, McGraw-Hill, Boston, M.A., 1996, p. 273

[4.9] J.D. Plummer, M. Deal and P.B. Griffin, *Silicon VLSI Technology, Fundamentals, Practice and Modeling*, Prectice Hall, Upper Saddle River, N.J., 2000

[4.10] J.L. Vossen and W. Kern, *Thin film processes*, Academic press, New York, 1978

Chapter 5. Hot embossing for packaging intelligent environmental sensors

5.1. Introduction

The hot embossing technique is becoming popular for fabricating microstructures in plastic. For example, this technique has been applied in microfluidic devices [5.1-5.3], microparts [5.4], and optical component [5.5] areas, adopting its inherent low cost and ability to replicate structures for mass production. In microfluidic devices, some demonstrated structures are reservoirs and microchannels for fluid to flow. In microparts, cogs and interdigitated combs have been presented [5.4]. In optical components, an anti-reflective grating has been made [5.5]. Instead of using the hot embossing technique to create the structures mentioned above, this chapter introduces a new application of the technique. The new technique is used to embed an integrated circuit (IC) fabricated on silicon into plastic sheet. To our knowledge, this application of the hot embossing technique for packaging IC has never been made. Our novel hot embossing technique was developed especially with an emphasis on the application for packaging support electronics in conjunction with environmental sensors. The environmental sensors such as humidity, temperature, air flow, pressure and gas sensors cannot accept the molding package type which is widely used in industry these days. Among currently available packaging methods, the flip-chip technique may be the method with the most potential for packaging both an environmental sensor and its support IC within the same housing. Flip-chip technology is known to protect the front side of a die as well as having the advantages of small parasitics and small footprints if a single die is used [1.11]. This technology features upside down mounting of a die and protection with underfill. If this technique is applied for packaging both an environmental sensor and its support IC stacked one upon the other, a problem arises in establishing electrical interconnection between the support electronics and the sensor. Since they are stacked, the interconnection has to be established using the techniques

such as through-holes and sidewalls of dice stated in the review section of packaging in Chapter 1. Polycarbonate (PC) encapsulation presented here avoids the creation of vertical interconnection. There are two major features of this technique. The first is that an IC in bare die form is faced down against PC and pushed into it, meaning that the PC protects the front side of the die. The second is the interconnection between the die and a sensor. The interconnection is established by bonding wires and copper tracks evaporated on to the PC. Encapsulation with PC provides environmental sensors and support IC with a packaging solution while protecting the support circuit from the environment. This package solution achieves the minimum number of access terminals for a sensor system; sensor output, power, and ground. This arrangement minimizes the size of the environmental monitoring system and presents a convenient process of replication for mass production.

The important points addressed are as follows:

Ensuring the embossed IC fabricated on silicon is functional.

The plastic is able to hold the brittle silicon die at room temperature after insertion.

Interconnection between the embossed IC and an environmental sensor is feasible.

The following subsections cover the process theory, material considerations, process details, results of experiments and potential extensions of the technology.

5.2. Polycarbonate encapsulation using hot embossing

The PC sheet in this experiment was manufactured by General Electric. Its size was approximately 40 mm 40 mm and its thickness was 1.5 mm. A commercially available IC die, LM324, was selected for hot embossing. A single die of LM324 contains four bipolar operational amplifiers. It was diced to the size of 1.5 mm 1.8 mm. The thickness of the die was 340 m. The surface of the die was covered with

silicon nitride except for bonding pads according to the data sheet given by manufacturer. The size of bonding pads was 80 m 80 m. Copper tracks on the PC were formed by thermal evaporation and patterned by photolithography to create electrical connections to components. A humidity sensor was used to test functionality in conjunction with the embossed die after embedding a LM324, and placing a humidity sensor as well as surface mount resistors. The humidity sensor used here is a parallel-plate capacitive type with a single polyimide layer as described in Chapter 3. The circuit built in this experiment is shown in Fig. 5.1. It generates square waves with R = 100 k and V^+ = +5 V supply. The capacitive humidity sensor varies the output frequency in accordance with absorption and desorption of moisture as a result of the change in the dielectric constant of the polyimide.

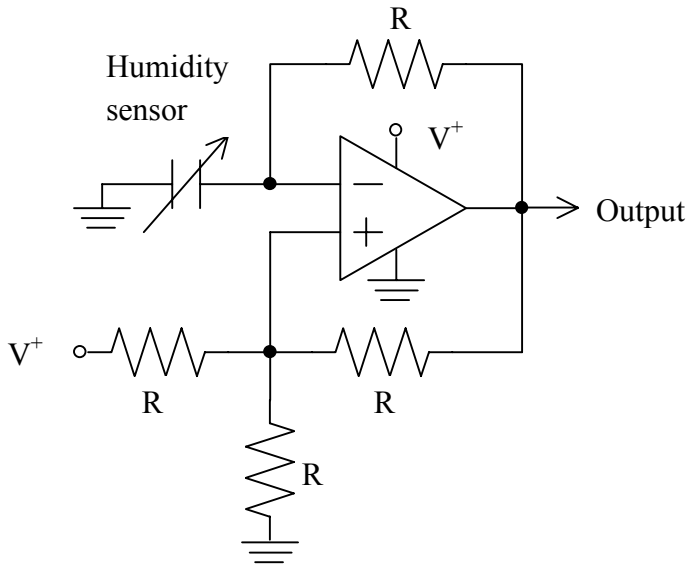

Fig. 5. 1. Square wave oscillator using an LM324 single power supply operational amplifier

5.3. Hot embossing machine

Initially a manually operated embossing machine was used to investigate whether it was suitable for embossing an integrated circuit die (ICD) fabricated on silicon into PC. In trials, securely embossing ICs was not a simple task as the ICs cracked most of the time. There was a need to design a custom built machine in order to securely insert the ICD into PC. The machine designed is capable of controlling the following: pressure, temperature of the plates (top and bottom), pre-heating, time settings for each stage and the accurate control of actual embossing of the ICD. The process required to emboss the ICD in PC is significantly different from that used for embossing metal or other parts. This is due to the brittle nature of silicon and the sensitivity of the electrical contacts established on the ICD. Traditional embossing machines operate manually where the pressure and other variables cannot be controlled uniformly. Moreover, embossing is performed in a single step process.

To achieve a successful embossing of the ICD and to satisfy all requirements, a semi-automatic machine was required so that the embossing could be done in a controlled environment (regarding pressure, temperature, time, pre-heating and embossing), and human involvement could be kept to a minimum. The pressure was set and maintained using a pressure regulator and the applied pressure depended on the size of the ICD and other variables. The temperature on the top and the bottom plates was controlled by heating elements and four thermocouples. Temperature was maintained accurately on both top and bottom plates at any location within a tolerance of ± 1 °C. A custom made hot embossing machine was designed by Neeli MadhusudanRao and built in Singapore.

The hot embossing machine (HEM) in Fig. 5.2 operates on pneumatics using compressed air from an air cylinder via a pressure regulator. It contains two brass plates, top and bottom where the embossing is performed. The temperature controller limits the activation of the complete system until the temperature settings are achieved. Embossing is performed in two stages; (1) When HEM is activated, the top plate moves

down and pre-heats the sample ICD resting on the bottom plate. (2) After pre-heating, the preset regulated pressure is applied from the top plate and embossing of the ICD occurs. A built-in timer controls embossing time before the plates are released. Once this time is elapsed, the pressure is released and the ICD is allowed to cool to room temperature.

Fig. 5. 2. The custom built hot embossing machine at Griffith University

5.4. Process theory and requirements

5.4.1. Environmental protection

One objective in the encapsulation process is to protect the ICD from the environment. Thus, identification of various environmental factors is necessary in order to determine if the polycarbonate encapsulation offers sufficient environmental protection. The sources of environmental contamination include dirt, dust, moisture and physical damage on the front surface of a bare ICD. Dirt, dust and physical damage can be minimized because the ICD is flipped over and embossed into PC. Minimizing the moisture level is important because moisture causes corrosion of the exposed metal on

the ICD. This metallization is commonly aluminium in most integrated circuits.

5.4.2. Interconnects

Electrical interconnection from the 80 m 80 m bonding pads on the ICD was achieved with gold wires between bonding pads on the die and tracks on PC. One vital part of the process was to ensure the wires remained intact after embossing. Two types of wire bonding machines were tested in our laboratory. One was a thermocompression bonder with gold wire. The other was an ultrasonic bonder with aluminium wire. The contact area between bonding wire and bonding pad is important. Because the head of the aluminum wire bonded by the ultrasonic bonder on a bonding pad was smaller than that of the gold wire bonded by the thermocompression bonder, the tension exerted on the aluminium wire during embossing caused an open circuit. On the other hand, the gold ball at the tip of gold wire secured the adhesion to bonding pad. This difference is inherent to the difference in operational principles of the two bonders. That is, the ultrasonic bonder creates adhesion and cuts a wire with heat created by vibration of a wedge, resulting in a small size of head as Fig. 5.3(a) shows. The thermocompression bonder creates a gold ball with an electrical spark in preparation for the next bonding cycle, resulting in a larger size of head as Fig. 5.3(b) shows. Since gold wires bonded by the thermocompression bonder did not break after embossing, interconnects between the ICD and tracks on PC were formed with gold wires throughout the experiment.

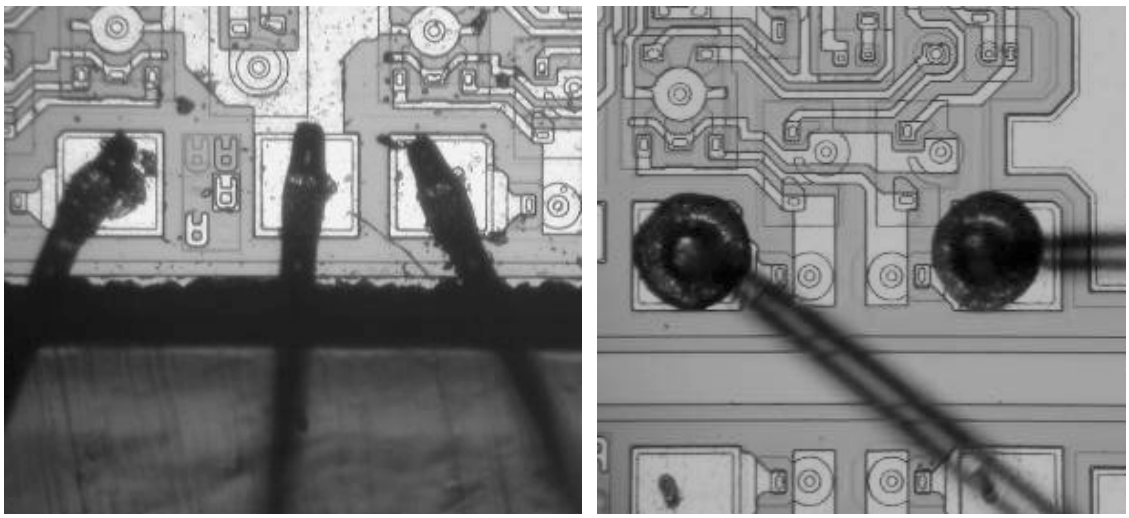

(a) (b)

Fig. 5. 3. Images of head parts of bonding wires (a) Aluminium wires bonded with an ultrasonic bonder (b) Gold wires bonded with a thermocompression bonder

5.4.3. Electrical insulation

Since wires used for electrical interconnection are not insulated, an electrical short circuit between the wires and the sidewall of the ICD is a common problem after performing hot embossing. There are two insulation methods to prevent this problem. One is growing silicon dioxide (SiO_2) on the side of the ICD. The other is coating the ICD with insulation material. Growing SiO_2 thermally around the ICD appears to be simple because this is a commonly used fabrication process for silicon integrated circuits. This method was not used because of the drawbacks listed in Table 5.1. This table contains the drawbacks when growing SiO_2 thermally either after or before wire bonding ICDs.

Table 5. 1. List of drawbacks in growing SiO_2 thermally

	After wire bonding	Before wire bonding
Drawbacks	Melting temperature of the aluminium (660 °C) on bonding pads on op amp is much lower than the temperature to grow SiO_2.	Alignment to open windows in SiO_2 for bonding pads is not practical due to extremely small die size. The alignment has to be done individual dies, not wafers. Etchant of SiO_2 used to open windows for wire bonding also strips SiO_2 on sidewall of the die.

Instead of growing SiO_2 thermally, chemical vapor deposition (CVD) is an alternative method to grow SiO_2 at lower temperature than 500 °C. CVD is an attractive method, however, the alignment process to open windows in SiO_2 for bonding wires is not practical. The cause of this problem is that the size of the ICD is too small for the alignment process. The problem of etching SiO_2 to open windows for wire bonding still remains as stated in Table 5.1.

Alternatively, the following insulation materials were investigated experimentally: silicon-based conformal coating for printed circuit board (PCB), polyimide, and polydimethylsiloxane (PDMS). Each material has merits and demerits. Block diagrams illustrating the sequential process employed are shown in Fig. 5.4. The merits and demerits of polymer-based insulator are listed in Table 5.2. Conclusions were made from experimental results.

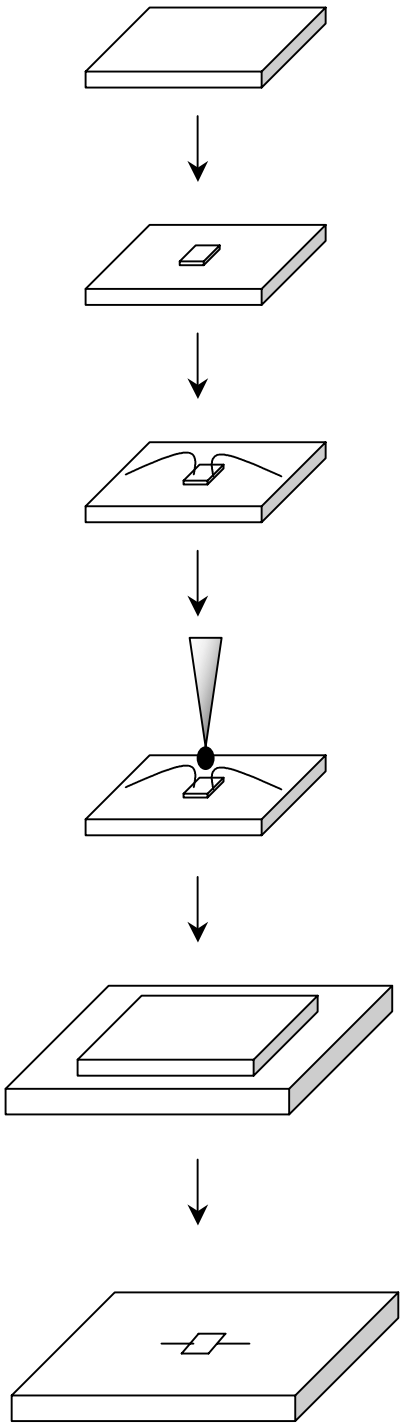

Prepare aluminium coated silicon dummy substrate

Glue a die on the dummy substrate

Bond with gold wires, terminated on ICD pads and pads on the dummy substrate

Dispense insulator over the die. Dry the insulator as it is.

Flip over the dummy substrate and emboss into polycarbonate

The die separates from the dummy substrate naturally and is transferred into polycarbonate.

Fig. 5. 4. Block diagram of application of insulator and process sequence of hot embossing.

Table 5. 2. List of merits and demerits of polymer based insulation materials

Material names	PCB conformal coating	Polyimide	PDMS
Merits	Quick dry at room temperature Thin film	Good insulator Easy to apply Thin film	Good insulator Easy to apply Relatively thick film Curing temperature is low (<150 °C).
Demerits	Adhesion is too strong to remove die from dummy substrate	Curing temperature is too high (300 °C).	Tool is required to remove die from dummy substrate Curing time can be very long if temperature is lower than 100 °C.

Embossing was not successful with PCB conformal coating and PDMS mainly due to strong adhesion between the ICD and the dummy substrate. The ICD was not transferred into PC from the dummy substrate during hot embossing because of this strong adhesion. The process developed for electrical insulation was coating the die with polyimide dielectric after bonding wires. The polyimide coating covers the entire ICD including the sidewall of the die. Polyimide was found suitable for embossing the die when it was cured at 150 °C. The ICD was embedded into PC without the aid of tools to separate the die from the dummy substrate. Electrical insulation between the wires and the die was tested with an arrangement of a non-inverting amplifier and confirmed the validity of electrical insulation. This method was tried several times and found to be repeatable.

5.4.4. Mechanical constraints

During insertion experiments, breakage of ICDs was observed. Two reasons were identified. One is inadequate heating temperature of PC and excess pressure applied when embossing. The other is the cooling procedure of PC after embossing. From this experience, it is important to examine the effects caused by the difference in material properties of PC and silicon. Some mechanical and thermal properties of silicon and PC are listed in Table 5.3.

The elastic modulus of PC varies according to temperature significantly as Fig. 5.5 shows. Glass transition temperature (T_g) is an important parameter to note for polymers as it determines the boundary between elastic and viscous behavior of materials. If PC is heated at the temperature much lower than T_g, it is rigid enough to break the silicon piece mechanically or the silicon piece pops out from the PC in the hot embossing process. If PC is heated well above T_g, the silicon piece is embedded well below the surface of PC. The mechanical aspects of silicon wafers are important because they are sliced along specific crystal planes to produce the particular crystal orientation wafers: {100}, {110}, and {111}. From experience, excessive force breaks silicon along these crystal planes. It is, however, useful to quantitatively understand how much silicon wafers with particular crystal orientations withstand under mechanical stress. Wilson et al. [5.7] conducted a test with a microcantilever beam created by etching {100} silicon wafers. Load was applied from the side of the beam to determine the silicon crystalline plane on which fracture occurs as Fig. 5.6 shows. Dimensions of the beam were: width = 100 m, length = 300 400 m and thickness = 18 400 m [5.7]. In fact, fracture stress (strength) varies in different crystal orientations. Fracture stress of p-type single crystal silicon with resistivity of 10 ·cm is listed in Table 5.4.

Table 5. 3. Some mechanical and thermal properties of silicon and polycarbonate

	Silicon [4.6]	Polycarbonate [5.6]
Density (g/cm^3)	2.4	1.2
Modulus of elasticity (GPa)	160	2.1 / 2.4
Poisson's ratio	0.22	0.39
Coefficient of linear thermal expansion (10^{-6} K^{-1})	2.6	70
Thermal conductivity (W/mK)	157	0.20
Glass transition temperature (C)		145

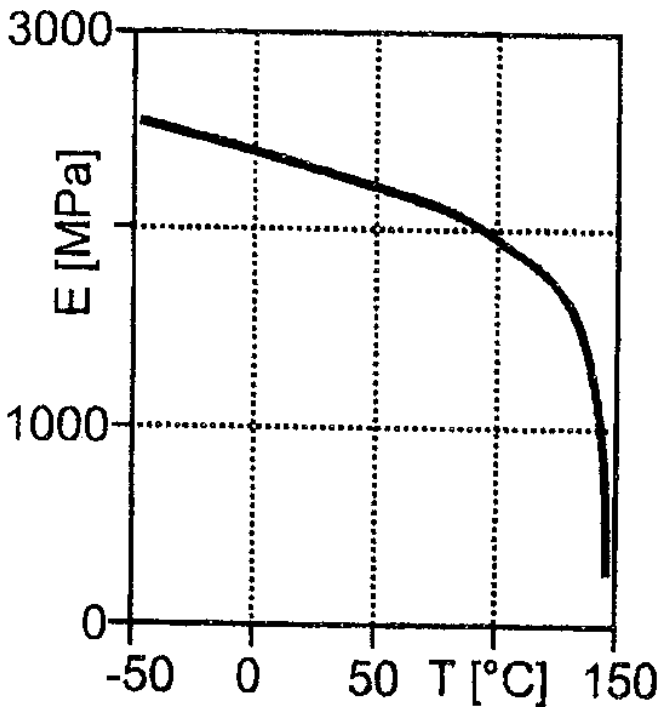

Fig. 5. 5. Elastic modulus of polycarbonate as a function of temperature. T_g = 145 C [5.6]

Table 5. 4. Fracture stress of two crystal orientations [5.7]

Fracture crystal orientation	Number of tests	Average fracture stress (GPa)	Standard deviation (Gpa)
{111}	103	1.3	0.3
{110}	80	2.3	0.4

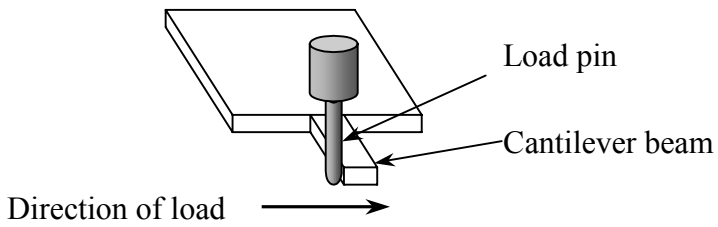

Fig. 5. 6. Schematic of a loading method conducted by Wilson et al. [5.7].

It is seen that the {111} orientation is weaker. The op amp used with hot embossing is bipolar type so that {111} orientation wafer is used. If excessive force is applied to the die, fracture occurs along the {111} plane.

ICDs were securely embossed and held in PCs when the working temperature was about 152 °C, which was an average temperature between the two plates in the HEM. As Fig. 5.5 shows, the elastic modulus of PC changes significantly between room temperature and 152 °C. Thus, the working temperature is beyond the region where Hooke's law governs. Hooke's law is defined as

$$= E \tag{5.4.1}$$

where is stress, E is elastic modulus (Young's modulus) and is strain. The elastic modulus which represents the stiffness of materials is highly non-linear in this temperature region. Poisson's ratio, , which represents the most fundamental behavior of elasticity of materials is defined as

$$\frac{transverse}{longitudinal} \tag{5.4.2}$$

where is strain. Poisson's ratio is the ratio of transverse contraction strain $\varepsilon_{transverse}$ to longitudinal extension strain $\varepsilon_{longitudinal}$. A positive value of Poisson's ratio means that a material becomes narrower when stretched. Most materials fall in this type. If Poisson's ratio is negative, a material becomes wider when stretched. Fukuhara et al. [5.8] studied Poisson's ratio of PC (DIALITE) as a function of temperature between 68 and 434 K and presented the experimental results. T_g of this PC is 423 K. The results show that Poisson's ratio decreased gradually from 0.40 to 0.34 as the temperature increased toward 409 K and increased suddenly as temperature further increased. The author pointed out that the reason of the abrupt increase from 409 K is due to viscoelastic softening associated with glass transition. Unlike elastic modulus, the change in Poisson's ratio is very small.

As a result of secure embossing stated above, the working temperature was determined around T_g. This fact inevitably turns the attention to a large difference in the coefficient of linear thermal expansion (CTE) between silicon and PC, which can be seen in Table 5.3. The mismatch of CTE induces stress and strain in the embossed sample if the temperature change is introduced. CTE expressed as below is no longer adequate as temperature approaches T_g [5.9].

$$_T \quad \frac{d}{dT} \tag{5.4.3}$$

where α_T is coefficient of linear thermal expansion, $d\varepsilon$ is change in strain and dT is change in temperature. Since CTE of silicon is much smaller than that of PC, a die can be forced to expand and contract with the PC during thermal cycling. Gradual cooling after embossing was found to be effective to avoid fractures in the die caused by a sudden temperature decrease.

5.5. Optimized process details

As a result of many experimental trials of hot embossing ICD into PC, the following procedures were found to give the most reliable results. The process flows as Fig. 5.4 shows.

(1) Preparation before embossing

Bonding wires were used to establish electrical connections from bonding pads on the ICD and copper tracks on PC. A method had to be developed to keep the bonding wires at appropriate positions as well as holding the ICD in position during the embossing process. The method realized was a dummy silicon substrate with evaporated aluminium. The ICD was placed on it and glued with alumina high temperature adhesive, 903HP from Contronics Corp. After the alumina was dried for one hour at 100 C, bonding was performed between the bonding pad and the appropriate position on the dummy substrate with gold wire. The location of copper tracks determines the positioning of the bonding wires. Aluminium was evaporated onto the dummy substrate making this bonding process reliable because the tail of the gold wire was kept steady during the embossing process. In the next process, the ICD was covered with polyimide for electrical insulation. The polyimide was dispensed over the die and cured for 30 min at 120 C. The polyimide served as an insulator to prevent the edge of the ICD from shorting electrically but it did not cover the entire length of the bonding wires. Fig. 5.7 shows the appearance of the ICD at this stage. All the materials used and five bonding wires can be identified from the figure.

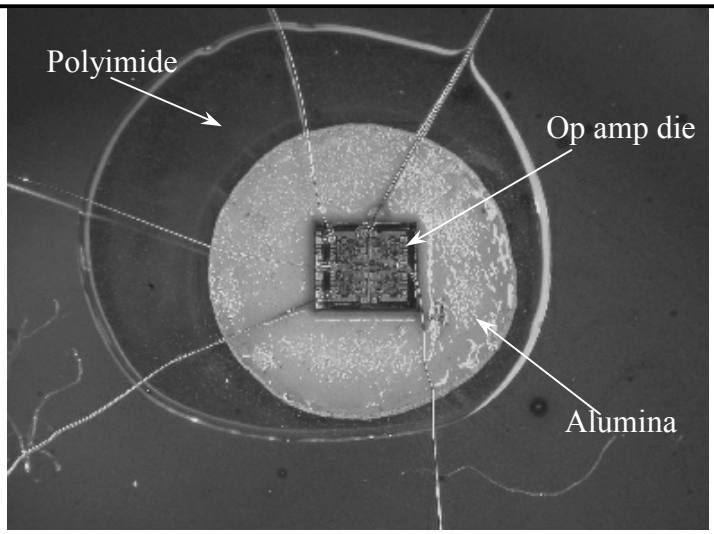

Fig. 5. 7. Top view of the op amp on the dummy silicon substrate with aluminium coating prior to hot embossing

(2) Hot embossing

The top and bottom plates of the HEM were preheated at 165 C and 140 C, respectively. These temperature settings are particularly important. At the minimum temperature of 140 C, the PC softens adequately. 165 C makes insertion of the bonding wires with the ICD secure. If the temperature is lower than 165 C, the bonding wires are trapped and dragged by the edge of the ICD, causing breakage at the neck of the bonding wires. The dummy substrate with the ICD was placed face down on PC. The dummy substrate and PC were then placed on the bottom plate of the HEM, and heated for 1 min. The hot embossing process was carried out in two stages. In stage one, the top and the bottom plates hold the ICD and PC for a further preheat time of 45s. In stage two, pressure was applied at 25 psi (approx. 172 kPa). After the embossing process was finished, the PC and the ICD were taken out from HEM and allowed to cool at room temperature. The dummy substrate was then removed from the PC at room temperature.

(3) Post embossing process

After embossing, the copper tracks and the bonding wires are not usually joined securely. There is also a requirement that some discreet electronic components

need to be mounted on the PC. The post embossing process requires forming electrical interconnections with the copper tracks, the ICD and the humidity sensor. This process was made with conductive silver epoxy. It was applied to the junctions between the copper tracks and each component interconnection. Three external access terminals; output, power supply, and ground, were also prepared. The completed sensor system on the plastic is shown in Fig. 5.8.

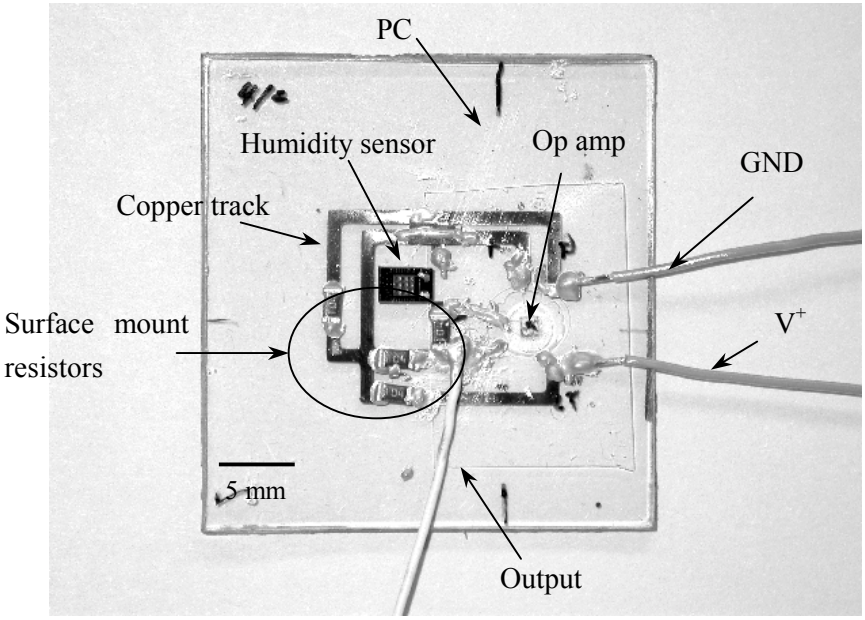

Fig. 5. 8. Complete sensor system on polycarbonate substrate with the embossed op amp, resistors and humidity sensor.

5.6. Results

(1) Surface profile

After insertion of the ICD with the bonding wires into the PC, the surface profile was investigated. Fig. 5.9 is an image of a bonding wire and a part of the embossed ICD. The image clearly shows that the wire is not entirely covered with the PC. This fact makes it possible to establish electrical contact with other parts of the circuit. The ICD is still intact revealing the smooth reverse side of the silicon substrate of the ICD. The object indicated by a circle in Fig. 5.9 is polyimide, which became brittle during the embossing process. Fig. 5.10 is the profile of a bonding wire embossed into the PC. The

trace was made across the surface of the PC to obtain this image using Tencor profiler, alpha-step 200. The bonding wire, 25 m in diameter, is located at 200 m in *x*-axis of Fig. 5.10. This image reveals that the bonding wire is actually embedded 670 nm lower than the surface of the PC. There are still large gaps at both sides of the wire.

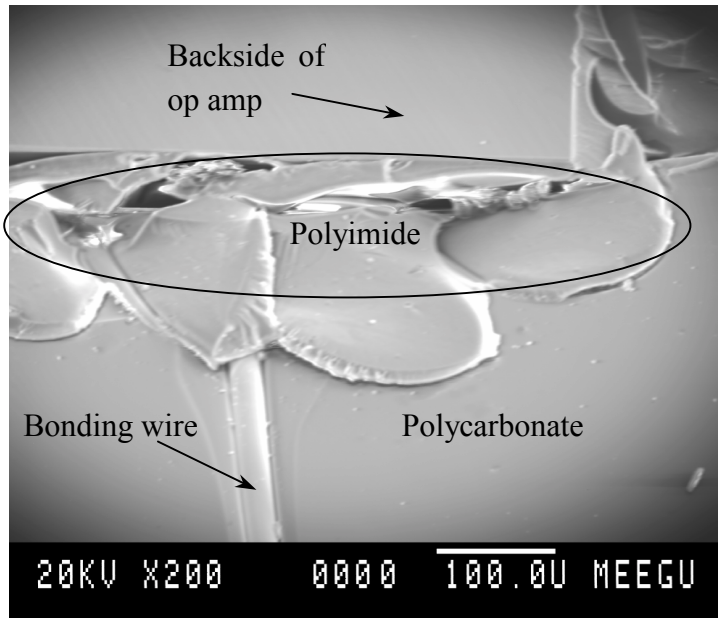

Fig. 5. 9. SEM image of a bonding wire after embossing the op amp into polycarbonate

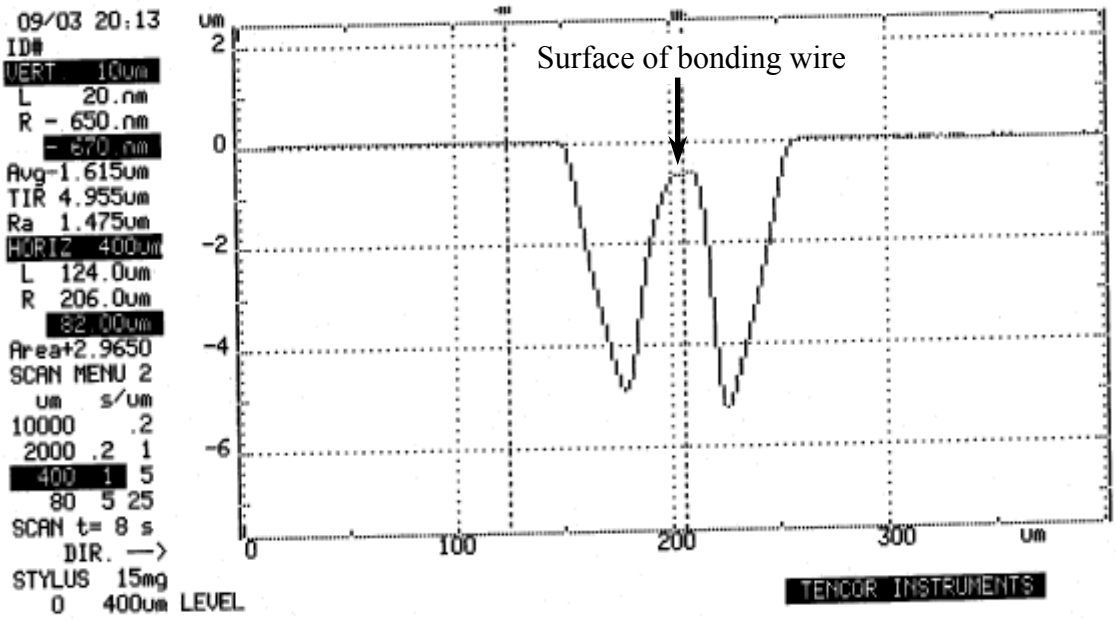

Fig. 5. 10. Surface profile of a bonding wire embossed into polycarbonate shown in Fig. 5. 9.

It is important to note how the embossing process influences the bonding wires along the sidewalls of the ICD. Fig. 5.11 is an image of the embossed bonding wires and the ICD taken from the underside of the PC. The critical points to investigate are the neck of bonding wires and the sidewalls of the ICD. The bonding wires along the sidewalls appear to have slopes partly due to the polyimide coverage. This is indicated with a circle in Fig. 5.11 (a). The image in Fig. 5.11 (a) was taken from the opposite side of which embossing was performed by looking through a PC sheet. Fig. 5.11 (b) may assist the understanding the conditions of the bonding wires around the embossed die.

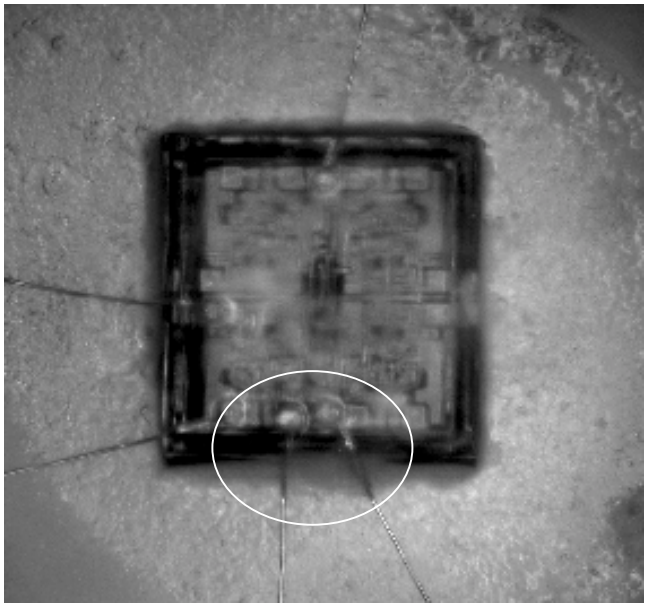

(a)

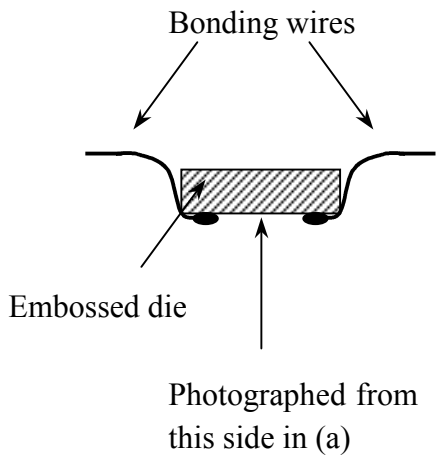

(b)

Fig. 5. 11. Bonding wires along op amp after hot embossing (a) Photograph from the backside see-through polycarbonate sheet (b) Cross section

Since the ICD is flipped over, there is no problem with dirt and dust on the active side of the ICD. However, water leakage could be a problem under the ICD. This test was performed with some drops of blue ink for ink jet printers. After waiting for one day, there was a small amount of migration of ink under the ICD. The leakage was mainly due to the scribe lines on the ICD made during the IC fabrication by the manufacturer. This indicates that a final sealing procedure may be required. No ink leakage was found under the wires because of firm contact to the PC.

(2) Testing with a humidity sensor

In order to test the validity of the concept, the complete sensor system shown in Fig. 5.8 was placed in a computer controlled environmental chamber, which is the same one used in Chapter 3. Measurements were conducted with the humidity sensor placed on the PC from 30% RH to 80% RH at 26 C, increasing the humidity at a rate of 1% RH/min. The frequency output was read by a frequency counter, GoldStar FC-7011. The result is plotted in Fig. 5.12. This indicates that the sensor system functions well

after embossing. The sensor response is almost linear. This test was conducted once.

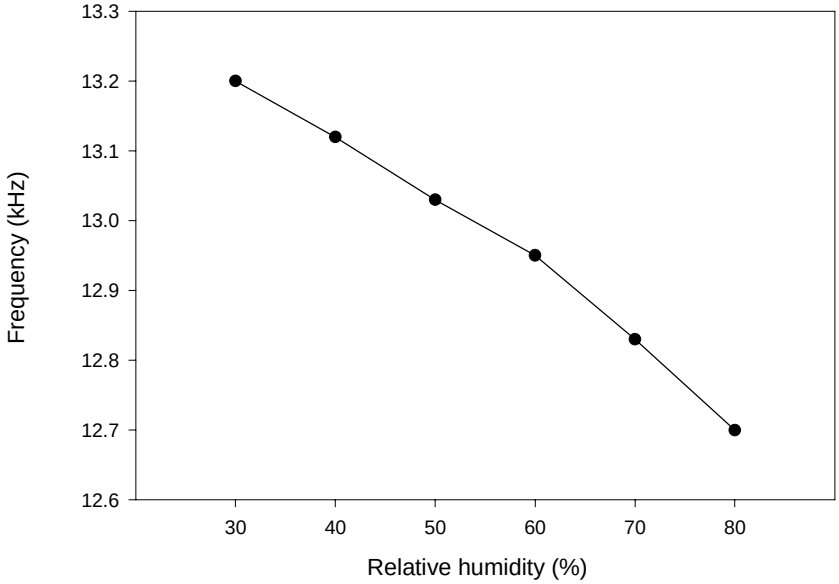

Fig. 5. 12. Measured frequency outputs of humidity sensor as a function of relative humidity.

5.7. Technical limitations and extension of technology

The processes presented in this chapter relied predominantly on manual operations based on many trials. These manual operations are a significant disadvantage in commercial use. The major process difficulties are the preparation of the dummy substrate, wire bonding, positioning of bonding wires, and photolithography of metallization on PC. This may be overcome by a number of alternative techniques that require further investigation.

Forming solder bumps, gold stud bumps, or electroless nickel bumps can eliminate the dummy substrate, wire bonding, and positioning of bonding wires. A chip with these bumps can be placed directly over electrical tracks and embossed.

Forming tracks by a screen-printing technique can eliminate

photolithography of metallization on PC.

Positioning the chip on PC with a camera system may allow automatic chip positioning and handling in embossing.

Interconnection between ICD and sensor can be formed during screen-printing process if the sensor is fabricated directly on PC. Alternatively, tracks on a polymer film rather than on PC can be attached on ICD and sensor.

5.8. Conclusions

In this chapter, the processes described above demonstrated the potential of embedding ICDs into plastic sheets for environmental sensors. This new technology is not necessarily limited to this application. Other potential applications include microfluidic monitoring and an activation system for biosensors (e.g. electric pumps, electric mixture, etc). Support electronics for detection and/or amplification of signals can be embossed in the same substrate as a microfluidic system. This represents significant progress to lab-on-chip technologies. If there is a potential to destroy the microfluidic structure in embossing ICDs, the embossing ICDs can be made in a plastic used as an intermediate layer or in the lid layer of microfluidic system. Other application areas would be products requiring small space/dimensions as well as a semi-rigid mechanical support. ICDs could be embossed into plastic cards, monthly train tickets, IC tags and so on.

These trials with the hot embossing technique have successfully demonstrated the validity of this technology. After ten trials during which many process parameters were adjusted, the conditions reported here yielded 50%. The environmental sensor system was successfully tested by monitoring frequency output generated with the embossed op amp into the PC and the mounted humidity sensor on the PC. The investigation of the profile of PC and the conditions of bonding wires indicates that the process is not destructive even though an op amp fabricated on a thin silicon substrate was used. Three important features which made this unique and innovative technique

possible are listed as follows:

Ensuring the embossed IC fabricated on silicon is functional.

The plastic is able to hold a brittle silicon die.

Interconnection between the embossed IC and an environmental sensor is feasible.

This section proved the new concept of packaging, however, the technique needs to be further improved and automated in order to adopt it for industrial use. Some results have been published [5.10] (See Appendix B).

References

[5.1] L.J. Kricka, P. Fortina, N.J. Panaro, P. Wilding, G. Alonso-Amigo, and H. Becker, "Fabrication of plastic microchips by hot embossing", *Lab on a chip*, 2, pp.1-4, 2002

[5.2] S. Qi, X. Liu, S. Ford, J. Barrows, G. Thomas, K. Kelly, A. McCandless, K. Lian, J. Goetteri and S.A. Soper, "Microfluidic devices fabricated in poly(methyl methacrylate) using hot-embossing with integrated sampling capillary and fiber optics for fluorescence detection", *Lab on a chip*, 2, pp.88-95, 2002

[5.3] G. Lee, S. Chen, G. Huang, W. Sung, and Y. Lin, "Microfabricated plastic chips by hot embossing methods and their applications for DNA separation and detection", *Sens. Actuators B*, vol. 75, pp. 142-148, 2001

[5.4] H. Becker and U. Heim, "Hot embossing as a method for the fabrication of polymer high aspect ratio structures", *Sens. Actuators A*, vol. 83, pp. 130-135, 2000

[5.5] C. David, P. Häberling, M. Schnieper, J. Söchtig, and C. Zschokke, "Nano-structured anti-reflective surface replicated by hot embossing ", *Microelectronic Engineering*, vol. 61-62, pp. 435-440, 2002

[5.6] G.W. Ehrenstein, *Polymeric materials*, Carl Hanser Verlag, Munich, 2001

[5.7] C.J. Wilson and P.A. Beck, "Fracture testing of bulk silicon microcantilever beam subjected to a side load", *J. Microelectromech. Syst.*, vol. 5, no. 3, pp. 142-150, Sept. 1996

[5.8] M. Fukuhara and A. Sampei, "Low-temperature elastic moduli and dilational and shear internal friction", *Jpn. J. Appl. Phys.*, vol. 35, pp. 3218-3221, 1996

[5.9] R.E. Schramm, A.F. Clark and R.P. Reed, *A compilation and evaluation of mechanical, thermal, and electrical properties of selected polymers*, Boulder, Colorado: U.S. Department of Commerce, 1973

[5.10] T.Suzuki, Neeli MadhusudanRao, D.V. Thiel, and P. Tanner, "Hot embossing integrated circuit dies in polycarbonate for environmental sensors", *CRC Annual Conference*, 7-8 Oct. 2003, Melbourne, Australia

Chapter 6. Conclusions

This thesis has focused on a number of novel manufacturing techniques designed to create environmental sensors with encapsulated electronics support. These major innovations were proposed, and tests revealed encouraging results.

Among the characteristics studied in humidity sensors based on the permittivity of polyimide, three factors enhanced the sensitivity. The three factors were a low curing temperature applied to polyimide, O_2 plasma treatment of polyimide and the partially perforated structure in polyimide. The behavior of humidity sensors with polyimide cured at a low temperature was higher sensitivity and more unstable response than those cured at higher temperature. This can be explained due to the effects of residual solvents and incomplete imidization. The sensor with O_2 plasma treated polyimide showed twice the sensitivity when compared with the non-plasma treated one. An investigation with XPS, FTIR and AFM techniques support this conclusion regarding the increase in sensitivity. The improvement is due to the increase both in carbonyl groups on the polyimide surface and in surface area of roughened polyimide. One of the other effects on the sensor constructed with plasma treated polyimide is a very small hysteresis. The possible reason is that water molecules may be bonded to carbonyl groups weakly. The sensor with the partially perforated structure in the polyimide also showed an increase in sensitivity. The fabrication method of this structure requires few additional steps without extra equipment. The partially perforated structure is created photo-lithographically rather than by a plasma etch process using the top electrode as a mask, thus causing chemical modification of the polyimide. The reason for the sensitivity increase can be explained by both the increase in surface area of polyimide and the effective bonding of water molecules with the polyimide chain even under the top electrode with an introduction of side walls of polyimide created at the holes in the top electrode.

In preparation for the design and fabrication of the multiple sensors, the effectiveness of thermal isolation was studied. Experimental results revealed that

thermal isolation is an important aspect of the process to eliminate thermal short circuiting between a heating element and a substrate. A very good thermal isolation was observed with a silicon nitride diaphragm supported by a silicon rim in comparison to a structure of polyimide plateau on a silicon nitride layer coated on the silicon substrate. Although dedicated equipment and tooling are necessary to produce a diaphragm using the silicon back etching technique, the fabrication strategies for the multiple sensor have demonstrated the feasibility of producing this structure with a single-sided mask aligner. The multiple sensor requiring 8-masking steps faced a number of process compatibility issues. The main hurdles to overcome were the method to align the front and back sides of structures with a single-sided mask aligner, the removal of photoresist without damaging polyimide after nickel etching and to perform silicon back etching while protecting the sensor surface from anisotropic silicon etching solution. Front-to-back alignment was feasible with the aid of alignment through-holes parallel to the {110} plane, which are opened initially. A nickel film was used to minimize the damage to a silicon nitride film coated on the silicon substrate through an anisotropic etching process twice over 10 hours. The usefulness of PAN etchant was demonstrated using a hard-bake-free photoresist method while etching nickel. This was performed in a carefully controlled thermal bath, and resulted in no damage to the polyimide layer. Another benefit of PAN is that a lift-off process can be avoided and heating the substrate is allowed during the deposition of metals. This results in an increase of process flexibility. Application of the resin as a protection layer of the multiple sensor during anisotropic silicon etching was found to be a suitable method. This method protected the sensor from the etchant as well as providing the diaphragm under the sensor with mechanical support. With the techniques developed, the multiple sensor yielded above 80 %.

The trend to integrate sensors and their signal conditioning electronics circuitry (SICONEC) on the same substrate was addressed. The packaging method of embedding a silicon die into a polycarbonate (PC) sheet using hot embossing is an alternative

approach to the conventional encapsulation method used in a majority of sensors and sensor support electronics circuitry such as ICs. The novel parts of this technique are the elimination of bulky encapsulation and a reduction in the amount and types of disposable materials while maintaining mechanical support and protection against damage from its local environment. The bulky encapsulation structures can be categorized in a mold type of encapsulation used for SICONEC and a sensor, and a casing around a PCB board containing parts which support SICONEC. The reduction of amount and types of disposable materials can be achieved by the demonstrated hot embossing packaging techniques because it does not use mold packaging, leadframes and PCB boards, and a casing for the PCB boards. Thus, fewer and less types of materials remain at the end of useful lifetime of sensor systems. The currently demonstrated PC sheet contains discreet components, resulting in a large size. If all discreet components were integrated at the die level, a very small piece of PC sheet would be required. In the proof of concept prototype, although the proposed process seems destructive, the embossed die and the bonding wires serving as interconnections remained intact after hot embossing was performed. The validity of embedding a silicon die into a PC sheet using hot embossing was reinforced by successful testing of a humidity sensor.

Future development

It is always important to produce as many sensors as possible per wafer in order to minimize the unit cost. To achieve this, the size of multiple sensor has to be reduced. If scaled proportionately, the capacitance of the humidity sensor decreases significantly. This may require a different approach to condition the sensor output electronically. One approach to this is a ratiometric measurement. This requires a reference capacitor and a humidity sensor in the same substrate. A smaller area can also be expected to enhance the mechanical strength of the entire multiple sensor. In order to reinforce the usefulness of the multiple sensor, integration of SICONEC with the sensor on the same substrate is

important. The fabrication process of the multiple sensor was carefully determined to fit the CMOS or bipolar processes from material point of view. Nickel is the only material, which does not fit the CMOS or bipolar process currently. However, nickel is not unique in a MEMS foundry. This still allows the sensor to be fabricated after SICONEC is integrated with the CMOS or bipolar process.

Packaging the multiple sensor requires a new approach in order to improve structural robustness while maintaining a good laminar flow. In addition, a mechanism is necessary to protect the sensor from damage during handling or monitoring in practical use. It is a significant technical challenge to meet all of these requirements at once. With regards to packaging, mounting the sensor inside the recess created in a PCB is an alternative method to a chip carrier. This may provide bonding methods across the sensor and the PCB other than wire bonding. Example interconnection methods for this packaging can be flexible tapes, metal hinges or through-holes in a silicon substrate. These interconnections have a potential of minimizing the disturbance of airflow.

In packaging ICs with the hot embossing technique, development of new methods must be made in two major parts, namely interconnection and protection of embedded IC from water and contamination. The interconnection has to be implemented in a cost effective way with high yield in an automated production line. A cost effective technique currently available is screen-printing. Conductive ink can be directly applied onto a PC sheet or an intermediate material to form interconnections. This still needs improvement in terms of junction quality on the boundary between PC and an embedded IC die, where the conductive ink may be disrupted. Another interconnection method is using Copper Clad Laminate Film (CCLF), which includes electrical tracks by patterning a copper layer. With this film, SICONEC is embossed without flipping over. The CCLF is placed over the SICONEC with appropriate a conductive adhesive on tracks. The CCLF also serves as a protective cover. An image of CCLF applied to a hot embossed chip is shown in Fig. 6.1. The protection over an embedded IC demonstrated in Chapter 5 can be implemented with materials, that

feature minimal water permeation, a good temperature stability, a good adhesion on PC, a high resistance against chemical and a long lifetime. One possible material for this purpose is a polyimide film designed for MCM packaging and flip-chip packaging. This material adheres well to PC sheets with an application of heat and pressure in a similar setting range used in embossing ICs.

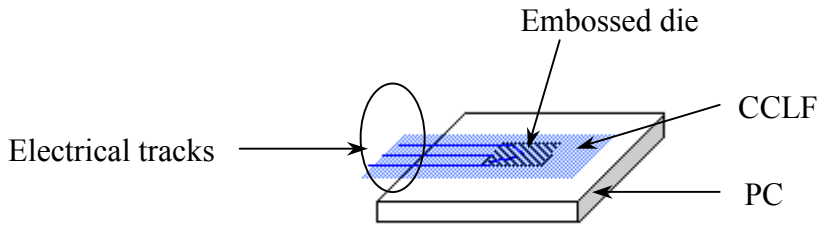

Fig. 6. 1. Schematic of hot embossed chip with CCLF

The goal continues to be to provide the world with tiny, low cost, intelligent and networked sensors. This thesis has explored a number of pathways towards this goal.

NOTE

Appendices A and B to this thesis consist of reproduced articles and have not been included in the electronic version of the thesis.

Appendix A:

Suzuki, Takeharu, Philip Tanner and David V. Thiel. **O_2 plasma treated polyimide-based humidity sensors.** *Analyst*, 2002, 127, 1342-1346.

Appendix B:

Suzuki, Takeharu, *et al.* **Hot embossing integrated circuit dies in polycarbonate for environmental sensors.** (Citation not given.)